

UC Santa Barbara

UC Santa Barbara Electronic Theses and Dissertations

Title

Molecular Ordering in Functional Blends of Organic Semiconductors

Permalink

<https://escholarship.org/uc/item/1466s86z>

Author

Sherman, Jessica

Publication Date

2014

Peer reviewed|Thesis/dissertation

UNIVERSITY OF CALIFORNIA

Santa Barbara

Molecular Ordering in Functional Blends of Organic Semiconductors

A dissertation submitted in partial satisfaction of the
requirements for the degree Doctor of Philosophy
in Chemistry

by

Jessica Brittany Sherman

Committee in charge:

Professor Michael Chabinyc, Co-Chair

Professor Thuc-Quyen Nguyen, Co-Chair

Professor Fred Wudl

Professor Javier Read de Alaniz

Professor Michael Doherty

December 2014

The dissertation of Jessica Sherman is approved.

Michael Doherty

Javier Read de Alaniz

Fred Wudl

Thuc-Quyen Nguyen, Committee Co-Chair

Michael Chabinyc, Committee Co-Chair

December 2014

Molecular Ordering in Functional Blends of Organic Semiconductors

Copyright © 2014

by

Jessica Sherman

ACKNOWLEDGMENTS

Those who set me on this path – Sandy Sherman, Mary Lynne Lovingood, and John Anthony. When I was little I swore I would never go into science, but I’m good at being wrong, and the three of you dragged me into it.

Those lost along the way – Geraldine Moyers, Mananya Tantiwiwat and Roger Kelley.

Those who kept me in research – Gary Sherman, who taught me how to ask questions and enjoy a challenge; Michael Chabinyc, for giving me a place to work when I was a lab refugee and offering a really unreasonable amount of support; Ben Sherman, whose writing and music reminds me that what I do for a living is fascinating and brutal, and whose formatting help was a great kindness.

Those who kept me alive – Marshall Ligare, Don Wenz and Sam Fulton-Koerbling, with whom I found a home when I needed one most; Nick Conn, for emergency deadlifts; Cathy Rives, Mary Miller and Janis Kling, for keeping me alive in a strictly literal sense; and Zak Kling—without whom I might not have graduated or even survived 2014.

And, of course, those who helped with the science. You know who you are.

VITA OF JESSICA SHERMAN

December 2014

EDUCATION

Bachelor of Science in Chemistry, University of Kentucky, December 2007 (cum laude)
Doctor of Philosophy in Chemistry, University of California, Santa Barbara, December 2014 (expected)

PROFESSIONAL EMPLOYMENT

2014: Teaching Assistant, Department of Chemistry, University of California, Santa Barbara
2011: Reader, Department of Chemistry, University of California, Santa Barbara
2009-2010: Teaching Assistant, Department of Chemistry, University of California, Santa Barbara
2009: Research Assistant, Outrider Technologies
2007-2009: Chemist I, Kentucky Department for Environmental Protection

PUBLICATIONS

Amorphous thin films of binary isomer mixtures. Sherman, J.B.; Chiu, C.-Y.; Fagenson, R.; Hawker, C.J.; Chabinyk, M.L. in preparation.

Crystalline alloys of organic donors and acceptors based on TIPS-pentacene. Sherman, J.B.; Moncino, K.; Parkin, S.R.; Wu, G.; Anthony, J.E.; Chabinyk, M.L. in preparation.

Role of crystallinity of non-fullerene acceptors in bulk heterojunctions. Sherman, J.B.; Purushothaman, B.P.; Kim, C.; Parkin, S.R.; Collins, S.; Anthony, J.E.; Nguyen, T.-Q.; Chabinyk, M.L. Submitted.

Fabrication and electrochemical photovoltaic response of CdSe nanorod arrays. Schierhorn, M.; Boettcher, S.W.; Ivanovskaya, A.; Norvell, E.; Sherman, J.B.; Stucky, G.D.; Moskovits, M. *J. Phys. Chem. C*, **2008**, *112*, 8516.

A new functionalization strategy for pentacene. Anthony, J.E.; Gierschner, J.; Landis, C.A.; Parkin, S.R.; Sherman, J.B.; Bakus II, R.C. *Chem. Commun.*, **2007**, 4746.

PATENTS

Photosensitized explosives. Sherman, J.B. U.S. provisional 61/867053 (filed 08/17/2013)

PRESENTATIONS

Suppression of crystallization in thin films of mixed isomers. (Poster) Sherman, J.B.; Chiu, C.-Y.; Fagenson, R.; Hawker, C.J.; Chabynyc, M.L. (CGOM11, Nara, Japan, 2014)

Functionalized Pentacene Alloys: Implications of Substitutional Disorder in Molecular Crystals and Thin Films. (Oral) Sherman, J.B.; Moncino, K.; Parkin, S.R.; Wu, G.; Anthony, J.E.; Chabynyc, M.L. (MRS meeting, San Francisco, 2014)

Organic semiconductor alloys. (Oral) Sherman, J.B. (Chemical Sciences Student Seminar Series, UCSB, 2013)

Pentacene alloys: structure and characterization. (Poster) Sherman, J.B.; Wu, G.; Parkin, S.R.; Anthony, J.E.; Chabynyc, M.L. (Center for Energy Efficient Materials review, Santa Barbara, CA, 2013)

Mixed crystals of functionalized pentacene derivatives. (Poster) Sherman, J.B.; Wu, G.; Parkin, S.R.; Anthony, J.E.; Nguyen, T.-Q.; Chabynyc, M.L. (CGOM10, Limerick, Ireland, 2012)

Beyond polymers and fullerenes: small molecule bulk heterojunction organic photovoltaics. (Oral) Sherman, J.B.; Purushothaman, B.P.; Kim, C.; Anthony, J.E.; Nguyen, T.-Q. (5th IWAMSN, Hanoi, Vietnam, 2010)

AWARDS

National School on Neutron and X-ray Scattering (2012)

Department of Energy Office of Science Graduate Fellowship (2010 - 2013)

National Science Foundation Graduate Research Fellowship (2010)

FIELDS OF STUDY

Major Field: Materials Chemistry

Studies in Thin Film Ordering of Organic Semiconductors with Professor Michael Chabynyc

Studies in Organic Photovoltaics with Professor Thuc-Quyen Nguyen

ABSTRACT

Molecular Ordering in Functional Blends of Organic Semiconductors

by

Jessica Sherman

Organic semiconductors offer a convenient reason to study how blending materials affects molecular packing. For example, organic solar cells rely on phase separation between dissimilar compounds to produce the “bulk heterojunction” morphology requisite for efficient devices. X-ray scattering and atomic force microscopy reveal that functionalized pentacene acceptors, which are highly ordered in neat films, lose long-range correlation when blended with a donor. These same acceptors can form substitutionally disordered single crystals (molecular alloys) when blended with other functionalized pentacenes, which share a high degree of structural similarity. Single crystal diffraction, UV/vis spectroscopy and thin film x-ray scattering show that substitutional disorder does not lead to loss of long-range order, even with the presence of multiple polymorphs. Finally we show that blends of organic materials can also lead to stable molecular glasses. We show that these stable molecular glasses can be formed from solution casting rather than from the more commonly used vapor deposition.

TABLE OF CONTENTS

1. Introduction: Organic Semiconductors and Blends	1
2. Role of Crystallinity of Non-Fullerene Acceptors in Bulk Heterojunctions	10
3. Crystalline Alloys of Organic Donors and Acceptors Based on TIPS-Pentacene...	68
4. Amorphous Thin Films of Binary Isomer Mixtures	100
5. Interfacial Doping of Organic Semiconductors	118
6. Ambipolar Transistors from Glassy Polymer	129
Acknowledgments	135
References.....	136

LIST OF TABLES

Table 2.1. Ionization energies (IE) and estimated electron affinity (EA)	15
Table 2.2. Characteristics of BHJ solar cells	20
Table 2.3. Crystallographic data from single crystal structures.	42
Table 2.4. HOMO and LUMO energy levels of acceptor F8TCHS.....	62
Table 2.5. Device properties for blends of donor C6PT2C6 with F8TCHS.....	63
Table 3.1. Unit cell parameters show thermal expansion	79
Table 3.2 Peak fittings	86
Table 3.3. HOMO and LUMO levels vs. optical gap.....	91
Table 3.4. Summary of crystallographic data	95

LIST OF FIGURES

Figure 1.1. Extending conjugation reduces HOMO-LUMO gap.	2
Figure 1.2. Schematic illustrating disorder in single crystals and thin films.....	5
Figure 1.3. Simulated diffraction data illustrates the effect of texture.	7
Figure 2.1. Chemical structures and diagrams of crystal packing.	14
Figure 2.2. Thin film absorption spectra on of the BHJs.....	19
Figure 2.3. Current-voltage characteristics of the BHJs.....	21
Figure 2.4. GIWAXS of neat donor and acceptor films	24
Figure 2.5. Morphological data for films of F8TIPS:C6PT2C6.....	28
Figure 2.6. Morphological data for thin films of F8TIBS:C6PT2C6	31
Figure 2.7. Morphological data for thin films of F8TCPS:C6PT2C6	34
Figure 2.8. Synthesis of trialkylsilylethynylated octafluoropentacene.....	38
Figure 2.9. J-V curves illustrating optimization of annealing temperature	45
Figure 2.10. EQE curves illustrating optimization of annealing temperature.	46
Figure 2.11. UV/vis of thin films of the neat donor and acceptors.	47
Figure 2.12. Overlap of emission of donor with absorption of acceptors.	48
Figure 2.13. PL quenching for C6PT2C6:F8TCPS and C6PT2C6:F8TIBS blends..	49
Figure 2.14. AFM of neat donor and acceptor films on PEDOT/ITO.....	50
Figure 2.15. AFM and C-AFM of blends.	51
Figure 2.16. GIWAXS of F8TIPS/C6PT2C6 blend, annealed.....	52
Figure 2.17. GIWAXS of F8TIBS/C6PT2C6 blend, as cast.	53
Figure 2.18. GIWAXS of F8TIBS/C6PT2C6 blend, annealed	54
Figure 2.19. GIWAXS of F8TCPS/C6PT2C6 blend, annealed.....	55

Figure 2.20. F8TCPS GIWAXS data plotted against SimDiffraction data	56
Figure 2.21. Chemical structure and crystal packing of F8TCHS.....	59
Figure 2.22 Thin film absorption spectrum for F8TCHS blended with C6PT2C6 ...	60
Figure 2.23. Bulk heterojunction solar cell performance of F8TCHS blend.....	61
Figure 2.24. F8TCHS:C6PT2C6 blend, cast as previously noted.	64
Figure 2.25. F8TCHS GIWAXS data plotted against SimDiffraction data	65
Figure 2.26. GIWAXS of F8TCHS/C6PT2C6 blend, annealed.....	66
Figure 2.27. GIWAXS of neat F8TCHS film.....	67
Figure 3.1. DFT calculations on a dimer of TIPS Pn: F8TIPS Pn.....	71
Figure 3.2. Distance between terminal acene rings vs. F8TIPS loading	76
Figure 3.3. Peak FWHM in the out-of-plane (00l) scattering direction.	83
Figure 3.4. Illustration of peaks fit to produce Table 3.2	85
Figure 3.5. Coherence lengths for mixed films	87
Figure 3.6. UV/vis spectra of thin films of TIPS Pn, F8TIPS Pn and alloy	92
Figure 3.7. Specular x-ray scattering measurements.....	94
Figure 3.8. HPLC data showing retention times and UV-vis spectra.....	96
Figure 3.9. ¹ H NMR spectra of a single mixed crystal.....	97
Figure 3.10. High resolution in-plane x-ray scattering.....	98
Figure 3.11 Example of packing schematics shown for one crystal structure	99
Figure 4.1. Chemical structures of (E)-MeBTP, (Z)-MeBTP, and DMDBS.	102
Figure 4.2. Crystal structure of (E)-MeBTP.....	104
Figure 4.3. DSC shows melting upon first heating a sample of (E)-MeBTP	106
Figure 4.4. AFM images of (E)-MeBTP film.....	110
Figure 4.5. Optical microscope images of (E)- and mixed (E)- and (Z)-MeBTP ...	111

Figure 4.6. Spherulite formation is not observed in films with 40% (Z)-MeBTP...	112
Figure 4.7. GIWAXS shows lack of order in films with 40% (Z)-MeBTP.....	114
Figure 4.8. (E)-MeBTP films with less (Z)-additive crystallize faster.....	116
Figure 4.9. UV/vis spectra of thin films of MeBTP isomers.....	117
Figure 5.1. Chemical structures of F TES ADT and F4TCNQ.	119
Figure 5.2. Schematic showing apparatus for sublimation of F4TCNQ.	121
Figure 5.3. Optical micrographs of F TES ADT films and sublimed F4TCNQ.	122
Figure 5.4. AFM images of F TES ADT and F4TCNQ films.....	123
Figure 5.5. GIWAXS of thin films.	126
Figure 5.6. Conductivity of F TES ADT films with and without F4TCNQ.....	128
Figure 6.1. Chemical structure of pBTPDPP polymer.	130
Figure 6.2. GIWAXS of pBTPDPP shows no strongly preferred orientation.	131
Figure 6.3. Hole transport in a pBTPDPP transistor.	133
Figure 6.4. Electron transport in a pBTPDPP transistor.....	134

1. Introduction: Organic Semiconductors and Blends

A. Molecular structure and properties of organic semiconductors

The delocalization of electrons is what makes hole and electron transport possible for carbon-based molecules and polymers. This delocalization is effected by conjugation—adjacent, coplanar p orbitals within a framework of σ -bonds are considered to be conjugated. Commonly, these p orbitals contain electrons involved in double or triple carbon-carbon or carbon-heteroatom bonds. However, empty p orbitals (in the case of cations), p orbitals containing one electron (in the case of radicals), or p orbitals containing lone pairs may also be conjugated.¹ In a conjugated system of π -bonds, the overlap between adjacent p orbitals, which describes the bonding and antibonding interactions in the structure, depends on the phase of each orbital in the system.² Conjugated p orbitals within a σ -bonded framework interact strongly, and these through-bond interactions perturb the energy levels of their bonding and antibonding orbitals as described by Huckel molecular orbital theory.³ In materials with conjugated p orbitals, a band gap exists between the highest occupied molecular orbital (HOMO) and the lowest unoccupied molecular orbital (LUMO); materials with extended conjugation exhibit smaller band gaps. For a simple example, we can consider the molecular orbitals of ethylene and butadiene (**Figure 1.1**). Ethylene has a HOMO-LUMO gap of 7.6 eV, whereas the HOMO-LUMO gap in butadiene is 5.7 eV; the next molecule in the series, hexatriene, has a HOMO-LUMO gap of 4.9 eV.⁴ Further extending conjugation in linear polyenes will continue to decrease the HOMO-LUMO gap, but even polyacetylene has a finite bandgap of ~ 1.5 -2.5 eV.⁵ This has been attributed to a Peierls distortion.⁶

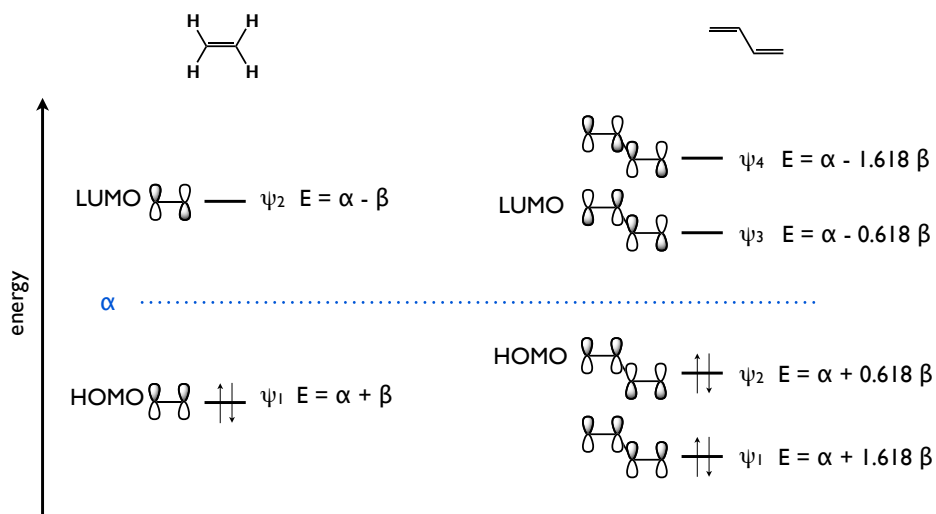


Figure 1.1. Molecular orbital energy levels in ethylene (left) and butadiene (right) show that extending conjugation reduces HOMO-LUMO gap.

Both molecular and polymeric semiconductors may feature these delocalized π -electrons, and many examples of both have been reported. Among molecular organic semiconductors, common structures with many derivatives reported include (but are not limited to) linear acenes, oligothiophenes and fullerenes.^{7, 8, 9, 10} A few semiconducting polymers include poly(phenylenevinylene) derivatives, polythiophenes, and polyfluorenes.^{7, 11, 12} The batch-to-batch variability among polymer semiconductors can be significant, and electronic properties and performance can vary with molecular weight and polydispersity.¹³ Small molecules, on the other hand, can often be purified using scale-friendly methods such as recrystallization, reducing (though not necessarily eliminating) batch-to-batch variability.¹⁴

The most crucial properties for a given organic semiconductor depend on its intended application, and synthetic functionalization allows for tuning of many of these important parameters. Processing is an important factor, since most relevant devices employ a thin film geometry. Adding alkyl substituents is a frequently employed strategy to improve solubility for solution processing.¹⁵ Common device applications for organic semiconductors include organic photovoltaics, organic light-emitting diodes (OLEDs), thermoelectrics and transistors. For organic photovoltaic applications, absorption of visible light is crucial, as this leads to higher current generation in devices.^{16, 17} The furthest-red absorption edge is set by the HOMO-LUMO gap; these energy levels can be tuned by adding donor or acceptor substituents.^{18, 19} For materials used in the active layer of an OLED, it is important to control the color and luminance of light emission.^{20, 21} Materials for thermoelectric applications do best with low thermal conductivity (common among many organic materials) and high electrical conductivity, which can be achieved by doping.^{22, 23} High-performance transistors require high charge carrier mobility, which can

depend heavily on the solid-state arrangement of semiconductor molecules, but the HOMO and LUMO levels are also important considerations in determining compatibility with contact metals and device stability under ambient conditions.^{24, 25}

B. Structural ordering

Organic compounds form weak crystals, mostly held together by van der Waals interactions; most organic semiconductors do not exhibit hydrogen bonding. Molecular crystals can be grown using a variety of methods, from solvent evaporation to solvent layering to sublimation.²⁶ Once a crystal of appropriate size is obtained (0.1 to 0.4 μm per side works well), single crystal structural determination can be carried out. A unit cell can be indexed after taking a few frames of diffraction, and its size and symmetry can be used to determine how to proceed with collecting a full set of diffraction data. Once the reflections are integrated and scaled, structure solution can take place—usually by direct methods, though other means such as simulated annealing can be employed. The initial structure solution yields a model that is further refined until the experimentally determined electron density agrees well with what is calculated from the model.

When compared to single crystals, thin films of molecular solids are generally less highly oriented. Single molecular crystals do exhibit some imperfections, including point defects, dislocations and twinning, as well as small angle grain boundaries between domains, which contribute toward mosaicity (**Figure 1.2**).²⁷ Thin films are prone to all these issues, in addition to out-of-plane orientation spread (due to tilting of crystallites relative to substrate normal) and large-angle grain boundaries in plane.²⁸

In addition to these issues, most thin films are less ordered than their counterpart molecular crystals. Thin films often exhibit cumulative lattice disorder of the second kind

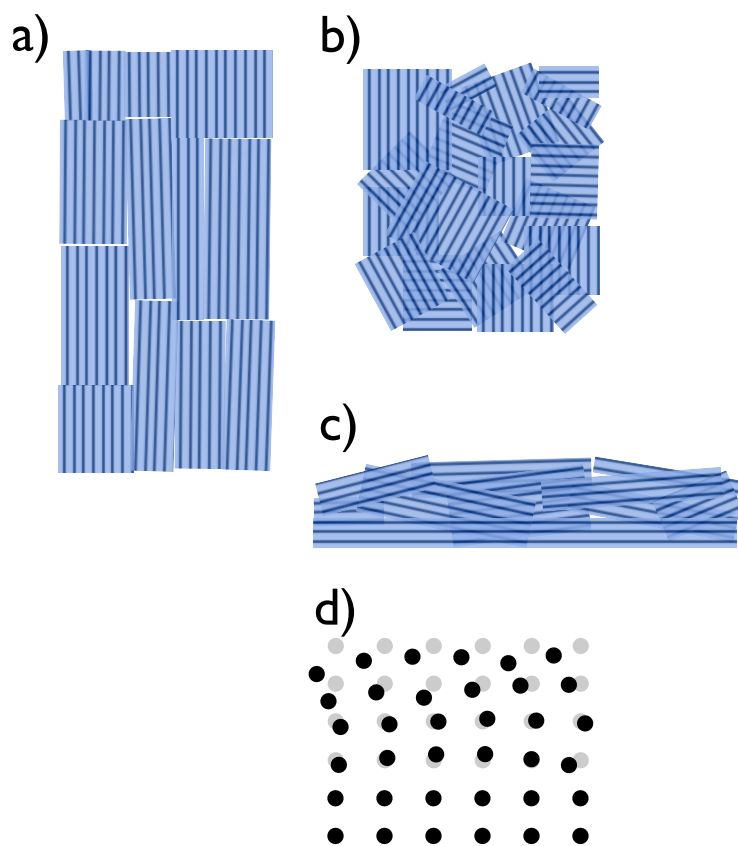


Figure 1.2. Schematic illustrating disorder in single crystals and thin films. In single crystals (a), mosaicity is caused by small-angle grain boundaries between domains. In thin films (b), large angle grain boundaries are often present in-plane unless careful measures have been taken to cast a film that is anisotropic in-plane. In addition to the in-plane orientation distribution, crystallites in thin films also exhibit an out-of-plane tilt angle distribution, (c). Paracrystalline disorder is illustrated in (d), which shows that cumulative lattice plane distortion can cause molecules (black) to deviate from their equilibrium lattice positions (grey) in such a manner that coherence of the lattice is lost over some length scale.

(paracrystalline disorder, illustrated in **Figure 1.2**), which leads to shifts in molecular positions, which distorts lattice planes until all coherence is lost, causing higher-order reflections to wash out..^{29,30} It is important to note that ordering within a thin film is strongly dependent on processing conditions, and that methods such as FLUENCE have been developed that produce highly ordered films of organic semiconductors.³¹

Obtaining a crystal structure can be useful in analyzing the solid-state ordering and texture within a thin film of the neat material in question. Like single crystal diffraction, thin film synchrotron x-ray scattering can provide a great amount of detail about the ordering and texture within a film. Wide-angle x-ray scattering performed at grazing incidence (GIWAXS) is a commonly used technique, and can be performed using an area detector, which rapidly collects data from a wide range of reciprocal space.³² **Figure 1.3**, illustrating the effect of different textures on a thin film diffraction pattern, was generated using SimDiffraction code, which simulates a diffraction pattern based on a bulk crystal structure.³³ Using this simulation data, it is possible to overlay experimental GIWAXS data with what is expected from a given bulk structure; this helps determine if the molecular packing is the same in the film as it is in single crystals. Several problems may arise. The first issue that can cause discrepancies between simulated and experimental data is that single crystal diffraction data tend to be collected at cryogenic temperatures (90 K to 150 K is common for many structures; the collection temperature is noted in the CIF file). GIWAXS data, on the other hand, are usually collected at ambient temperature. Because there is no way to predict how thermal expansion will affect the unit cell axes, it is useful to index the unit cell of a single crystal at ambient temperature for comparison. The second problem is that many organic compounds crystallize in several polymorphs, and some

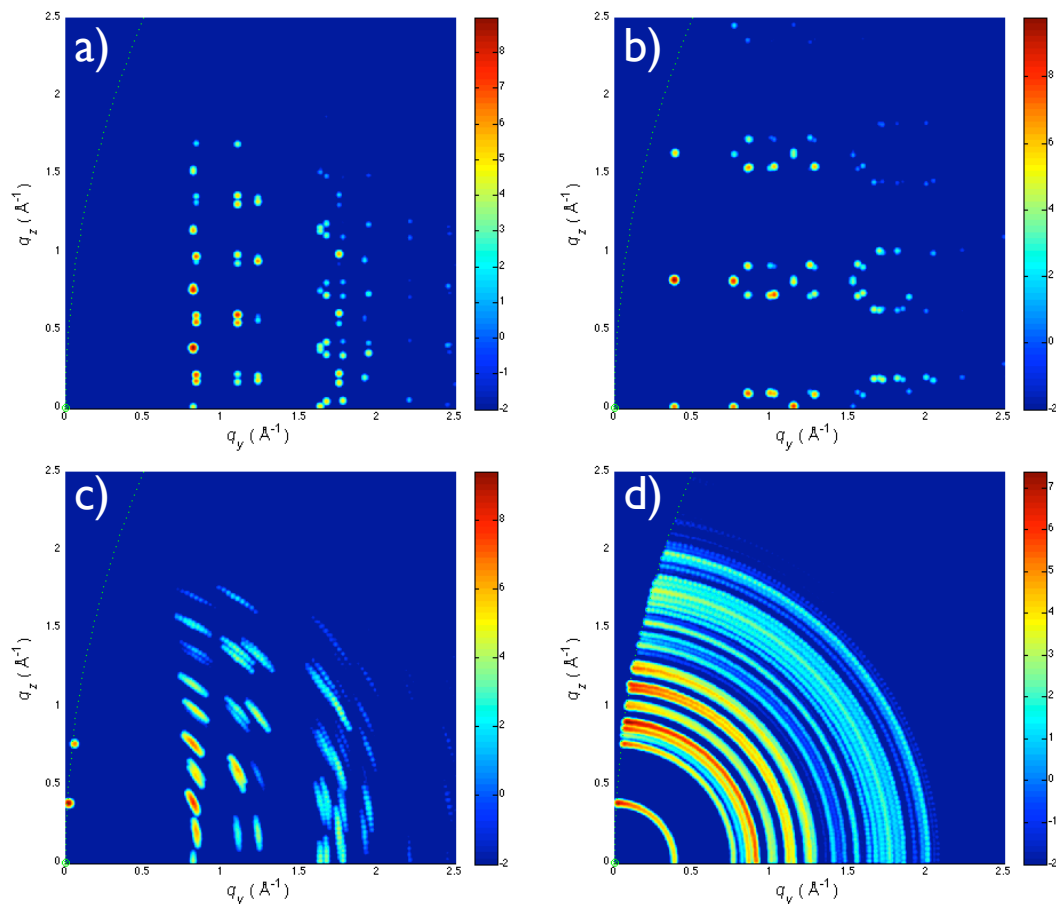


Figure 1.3. Simulated diffraction data using the bulk unit cell of TIPS pentacene illustrates the effect of texture.¹⁵ (a) shows a film oriented with (001) planes parallel to the substrate, and (b) shows a film with (010) planes parallel to a substrate. If a small out-of-plane orientation spread is present, as seen in (c) (4° for the (001)-oriented film), the reflections appear as small arcs. If a thin film has no preferred orientation, as seen in (d), the reflections appear as rings, like what would be observed for a powder sample.

polymorphs are only observed in thin films.³⁴ While it is possible to solve the crystal structure of a thin film polymorph using methods such as simulated annealing, commercial software has not been developed for this task, and high-quality data are required.^{35, 36}

C. Blends of organic compounds and organic semiconductors

Blends of organic compounds are useful for a variety of purposes. The earliest studies include the use of dye inclusion crystals to elucidate growth mechanisms.³⁷ In the pharmaceutical community, blending additives and excipients with active pharmaceutical ingredients can influence crystal habit, polymorph selection and crystallite size distribution—all crucial parameters to control in producing effective drugs.^{38, 39, 40} Polymorph selection, in particular, is very sensitive to the presence of trace amounts of additives; in some cases, such as that of ritonavir, a polymorph may “disappear” in the presence of impurities.^{41, 14, 42} Beyond the pharmaceutical industry, energetic materials are sometimes cocrystallized to produce more shock-sensitive explosives.^{43, 44, 45} Alternatively, blending small amounts of the explosive HNS with TNT can prevent the undesirable growth of friable needles, and can thus improve the shelf stability of TNT.⁴⁶

In the field of organic electronics, additives can be blended with organic semiconductors to influence thin film growth and morphology. The most ubiquitous example is that of electron donors and acceptors blended to produce the “bulk heterojunction” morphology that leads to efficient solar cells.⁴⁷ Thin film morphology and molecular packing can also be influenced by an underlying layer of another compound.^{48, 49} The addition of a nucleating agent can improve film uniformity.^{50, 51} Even the presence of an unintentional additive can affect film morphology by inducing lattice defects.^{52, 53}

Beyond lattice defects, the presence of additives also influences the electronic properties of a molecular solid.⁵⁴ Impurities with the right transport levels act as charge carrier traps, decreasing mobility in transistors.⁵⁵ Photoexcited charge carrier dynamics can be influenced by the presence of an additive.⁵⁶ Donor/acceptor complexes have been widely studied; these materials show a charge transfer excitation in which the neutral D/A complex becomes an ionized D⁺/A⁻ complex.^{57, 58} Many donor/acceptor complexes, such as TTF:TCNQ, exhibit high electrical conductivity.⁵⁹ Depending on the energetics of the frontier molecular orbitals, adding an acceptor to a donor can lead to doping—small amounts of the electron acceptor F4TCNQ can be used to dope polymers and make them more electrically conductive.⁶⁰ This doping can even take place at the interface of the two materials without significant mixing.²²

A few structural possibilities exist for blends of molecular solids. In the simplest case, the blend is a bilayer and all interaction is confined to the interface. Some blends (most notably those in bulk heterojunction solar cells) exhibit phase separation, though more than two phases may be present.⁶¹ In some cases, blending two or more components can be used to achieve an amorphous film.^{62, 63} Some compounds are isostructural and can form solid solutions that may be well-ordered.^{64, 65} This dissertation explores these cases.

2. Role of Crystallinity of Non-Fullerene Acceptors in Bulk

Heterojunctions

Jes B. Sherman[†], Balaji Purushothaman[‡], Sean R. Parkin[‡], Chunki Kim[†], Sam Collins[†],
John Anthony[‡], Thuc-Quyen Nguyen[†], Michael L. Chabinyc^{*§}

A. Abstract

Understanding the solid-state structure of the bulk heterojunction provides insight into how to improve the performance of nonfullerene acceptors in organic solar cells. We have characterized the self-assembly of three functionalized pentacene acceptors in single crystals, neat films and bulk heterojunctions formed by blending with a diketopyrrolopyrrole-based molecular donor. Atomic force microscopy, grazing incidence wide-angle x-ray scattering and optical spectroscopy indicate that the presence of the donor perturbs the packing and texture of acceptors with smaller substituents. The structural characterization explains the differences in performance among the three acceptors studied and suggests that, unlike fullerenes, disordered domains of molecular acceptors with planar molecular structure have inefficient electron transport in BHJ thin films.

B. Introduction

Organic photovoltaics (OPVs) are a class of thin film solar cells that can be fabricated by deposition from solvents using simple printing methods. The highest performance OPVs are bulk heterojunctions (BHJs), where an electron donating material and an electron accepting material are dissolved together in solution and then cast into a blended thin film.^{66, 67} BHJ solar cells with both small molecule and polymer donors with fullerene-based acceptors have been demonstrated with power conversion efficiencies approaching 10%.^{68, 69, 70} Due to

the relatively short exciton diffusion lengths in organic semiconductors (~ 10 nm), the length scale of phase separation of the donor and acceptor domains in efficient BHJs is ideally on the order of 20 nm. Because of this complex morphology, BHJs present an opportunity to exploit molecular self-assembly and to investigate the role of molecular packing within biphasic blends.

The formation of efficient BHJs relies on the nanoscale phase separation of the donor and acceptor upon casting. If the donor and acceptor crystallize readily, the phase separation process is additionally complicated by the kinetics of the growth of crystalline domains. Here, we study the role of crystallization of non-fullerene acceptors in BHJs using a series of silylethyne-substituted pentacenes as acceptors with a well-performing diketopyrrolopyrrole-based donor. Systematic investigation of alternative acceptors with a fixed donor is a necessary step in the development of design rules for molecular BHJ OPVs.^{71, 72} Our results demonstrate the critical role of molecular packing in thin films on the properties of small molecule BHJs.

Using molecular semiconductors instead of polymers in BHJ solar cells affords an opportunity to explore structure-property relationships with materials that are inherently monodisperse and can be purified by simple methods such as recrystallization.^{73, 74} Molecular materials can be deposited by solution casting or by vapor deposition allowing both the donor and acceptor to be cast from solution or by a combination of solution and vapor deposition.^{75, 76, 77} Many small molecules exhibit high optical extinction coefficients in thin films, up to 10^5 cm^{-1} , and have broad overlap with the solar spectrum.⁷⁸ Additionally, their electronic levels can be tuned easily by attaching substituents that donate or withdraw electrons from the aromatic core allowing materials to behave as either donors or acceptors in BHJs.⁷⁶

The acceptor in a BHJ has an important role in charge generation and also in setting the open circuit voltage (V_{oc}).^{79, 80} Because the molar ratio of donor to acceptor is generally near one in BHJs, it is desirable that the optical absorption of each are both strong and have complementary overlap with the solar spectrum. Fullerenes are the most widely used acceptors due to the ability to promote efficient charge generation and charge extraction despite their relatively poor optical absorption coefficient (relative to the donor). Non-fullerene acceptors have been demonstrated to form BHJs with reasonable power conversion efficiencies, but they are still below the performance of fullerene-based BHJs with the same donor.^{79, 81, 82, 83, 71, 72, 84, 85, 86}

It is not well understood why non-fullerene acceptors underperform relative to their fullerenes using a common donor.⁸⁷ It is possible that the answer lies within the observed morphology of highly efficient fullerene-based BHJs. Fullerenes are disordered in BHJs showing only broad x-ray scattering peaks even in the presence of a highly ordered donor.⁸⁸ The overlap of the molecular orbitals between two adjacent nearly spherical fullerenes does not depend on orientation and charge transport is likely tolerant of molecular disorder. In contrast, most non-fullerene acceptors have a relatively planar structure dictating that the strongest electronic coupling (and thus efficient electron transport) between molecules occurs when they are oriented co-facially.⁸⁹ As a consequence, these π - π interactions will promote the assembly of crystalline domains within a blend film. For example, a recent study using electron-deficient pentacene acceptors with P3HT as the donor showed large-scale crystal growth through the film for acceptors that pack with strong cofacial π - π interactions, whereas acceptors with sandwich herringbone crystal packing (containing fewer cofacial interactions) formed blend films without obvious large-scale phase separation, and exhibited higher power conversion efficiency.^{90, 91} With this in mind, we

expect that the molecular packing of small acceptors (that is, the interactions between molecules in the solid state) has significant influence on their thin film morphology and their resulting optoelectronic behavior.^{91, 30}

We present here a study of the molecular ordering of silylethyne-substituted pentacenes with a common molecular donor in BHJs. These materials are particularly useful for the examination of structure-property relationships in small molecule BHJs because their crystal packing can be tuned relatively independently of their electronic transport levels simply by altering the peripheral trialkylsilyl substituent.¹⁵ We focus on the octafluoropentacene derivatives shown in **Figure 2.1** because fluorination has been shown to yield highly stable materials with good electron transport properties.^{92, 25} The ionization energy and electron affinity (HOMO and LUMO energy levels) of these compounds (**Table 2.1**) are suitable for use as acceptors with diketopyrrolopyrrole-based donors, and we expect high open circuit potentials (~ 1.0 V) to result from the pairing. Diketopyrrolopyrroles have high optical extinction coefficients, on the order of $10^4 \text{ M}^{-1} \text{ cm}^{-1}$ in solution, and BHJs with modest power conversion efficiencies have been made with them with fullerene acceptors.^{93, 94} Using a combination of x-ray scattering, conducting probe atomic force microscopy, optical characterization, and device measurements, we examine how this series of non-fullerene acceptors and molecular donor crystallize and phase separate in BHJ films.⁹⁵ Although the resulting power conversion efficiencies of the cells are low, our results reveal how crystallization affects the morphology and performance of these small molecule BHJs.

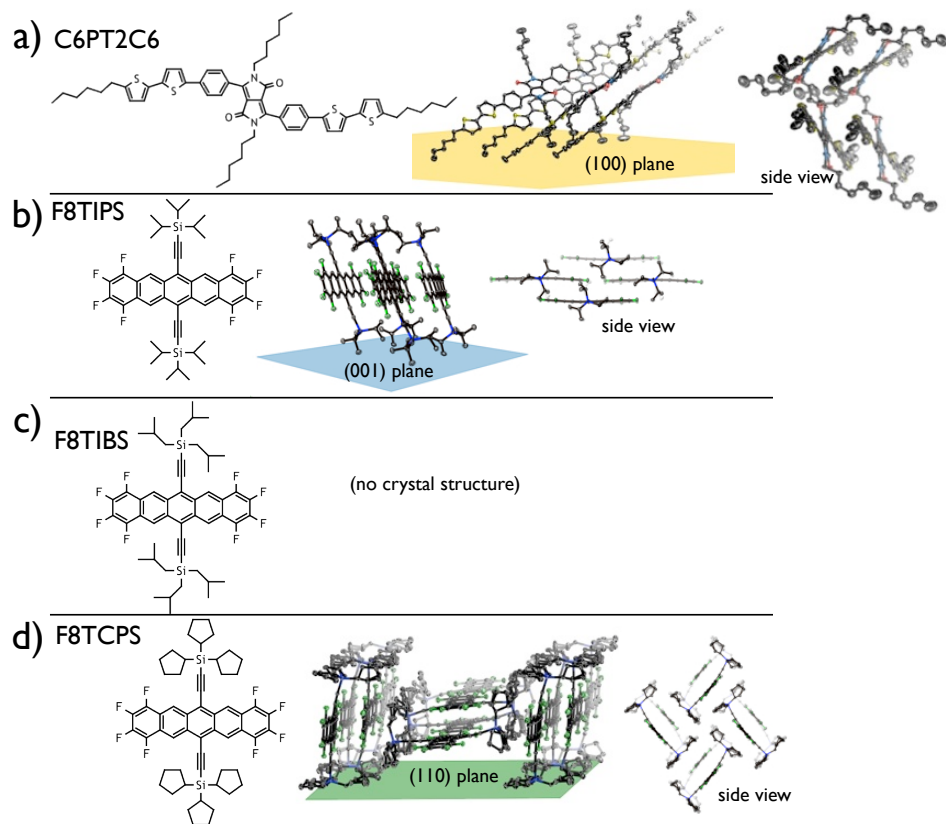


Figure 2.1. Chemical structures and diagrams of crystal packing of the donor (C6PT2C6) and the acceptors (F8TIPS, F8TIBS, and F8TCPS).

	C6PT2C6	F8TIPS	F8TIBS	F8TCPS
IE (eV)	5.16	5.51	5.59	5.71
EA(eV)	3.32	3.56	3.61	3.71

Table 2.1. Ionization energies (IE) and estimated electron affinity (EA) of the donor (C6PT2C6) and the acceptors (F8TIPS, F8TIBS, F8TCPS). The ionization energies (HOMO) were determined by UPS (on thin film); the electron affinity (LUMO) are estimated using the optical bandgap from the absorption edge of thin film UV/Vis spectra. Data for C6PT2C6 taken from [26].

C. Results and Discussion

i. Single Crystal Structures of Pentacene-based Acceptors and Diketopyrrolopyrrole-based Donor.

In thin films of small molecule BHJ blends, both the donor and the acceptor may crystallize, leading to a complex evolution of the phase separated morphology during deposition or during post treatments.¹³ Because many organic semiconductors exhibit thin film polymorphs or form co-crystals, it is also of interest to develop a better understanding of how the solid-state organization is perturbed by the addition of a second component a blended thin film.^{26, 35, 96, 97} In many cases, single crystal structures are not available, complicating quantitative analysis of x-ray scattering data from thin films.⁹⁸

The single crystal structure of the donor and acceptors provide a means to determine if ordered domains in thin films have the same packing structure as the bulk crystals. The single crystal structures of the donor, C6PT2C6, and one of the acceptors F8TIPS were previously determined. The structure of F8TCPS was solved here (CCDC 1034523). The crystal structure of F8TIBS could not be determined due to the inability to grow high quality single crystals. As shown in **Figure 2.1**, the donor material in this study, C6PT2C6, packs in a gamma-motif with close contacts between adjacent molecules within a stack.^{93, 91} As reported previously, F8-TIPS packs in a similar fashion to TIPS pentacene; that is, close cofacial stacking between aromatic cores.^{99, 100} F8-TCPS packs in a “sandwich herringbone” motif.⁹¹ This packing motif in pentacene acceptors has consistently produced the highest photocurrents in OPV devices using polymer donors.^{101, 90} Using these single crystal structures, we quantified the molecular orientation in thin films by examining the texture of the crystallites (*vide infra*).

ii. Characteristics of Bulk Heterojunction Solar Cells.

In order to relate the thin film structure to the current-voltage characteristics of solar cells, we fabricated BHJ solar cells and optimized the annealing temperatures and blend ratios through empirical testing (Details in Supplementary Information). We have used a common donor molecule, C6PT2C6, for all the BHJs. This donor material exhibits a moderate hole mobility ($\sim 2 \cdot 10^{-3} \text{ cm}^2/\text{Vs}$) in organic thin film transistors and has been successfully used as a donor in OPV devices with fullerene acceptors.¹⁰² BHJ films were spun-cast and processed according to procedures listed in the Supporting Information. UV/Vis spectra of the BHJ films (**Figure 2.2**) show that they absorb light from about 275 nm up to about 700 nm. The long wavelength absorption edge is set by the acceptor rather than the donor in contrast to many fullerene-based BHJs where the donor has the lowest optical edge.¹⁷ The current-voltage (J-V) response of the solar cells in the dark and under AM1.5 simulated solar illumination are shown in **Figure 2.3**, and their characteristics including the short circuit current, J_{sc} , open circuit voltage, V_{oc} , fill factor, FF, and power conversion efficiency are summarized in **Table 2.2**. While the open circuit voltage was near 1.0 V for all the devices, the absolute power conversion efficiencies were low ($<1\%$) due to the J_{sc} . These results with TIPS-pentacene acceptors can be compared to C6PT2C6:PC₇₁BM solar cells that have V_{oc} of 0.90, J_{sc} 7.9 mA/cm² and FF 0.49.¹⁰³ Clearly the largest difference is the short circuit current suggesting inefficient charge generation or extraction in the non-fullerene cells here. Photoluminescence (PL) quenching data suggests that charge extraction before recombination is a major cause of the low PCE. PL data was obtained by excitation at 520 nm dominantly excites the donor, C6PT2C6. TIPS-pentacene derivatives are known to have a very low PL yield and we did not pursue PL studies by excitation of the acceptor.¹⁰⁴ The PL data shows emission from C6PT2C6 as expected and the quenching

efficiency was relatively high ($>50\%$) for the BHJ blends over a range of annealing temperatures. Because of the overlap of the emission of C6PT2C6 and the absorption of TIPS-pentacene acceptors, we expect that energy transfer from the donor to the acceptor will occur and aid in bringing excitons to the donor-acceptor interface over a longer range than just exciton diffusion.¹⁷ The very low PL yield of the acceptors makes it difficult to study this process in detail. The PL data from excitation of the donor suggests clearly that the excitons are quenched, but any charges that are generated are not extracted efficiently, i.e. they recombine. We therefore sought to understand the origin of the low PCE despite relatively good PL quenching by studying the morphology of these BHJs.

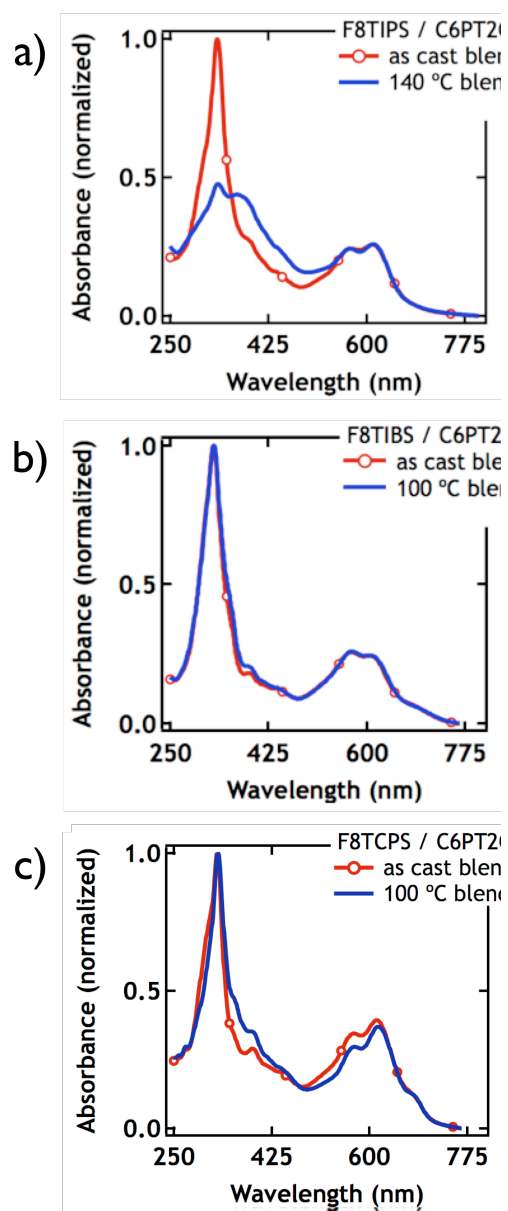


Figure 2.2. Thin film absorption spectra on of the BHJs before and after annealing on quartz. The BHJ films were spun-cast at 2000 RPM/60s from 1.5% (w/v) chloroform solutions.

	F8TIPS		F8TIBS		F8TCPS	
Condition	As cast	140 °C	As cast	100 °C	As cast	100 °C
V_{oc} (V)	1.03	1.03	0.60	0.80	0.93	1.00
J_{sc} (mA/cm²)	0.07	0.15	0.06	0.07	0.38	0.56
FF	0.40	0.44	0.31	0.34	0.48	0.58
PCE (%)	0.03	0.07	0.01	0.02	0.17	0.21
μ_h (cm²/Vs)	2.0•10 ⁻⁵	1.2•10 ⁻⁵	1.1•10 ⁻⁵	1.5•10 ⁻⁵	5.5•10 ⁻⁶	1.5•10 ⁻⁵
μ_e (cm²/Vs)	3.9•10 ⁻⁵	1.4•10 ⁻⁵	1.4•10 ⁻⁵	1.6•10 ⁻⁵	1.5•10 ⁻⁵	1.5•10 ⁻⁴

Table 2.2. Characteristics of BHJ solar cells of C6PT2C6 with the acceptors, listed at top, under various processing conditions (as cast, thermally annealed). Hole and electron mobilities were determined from space charge limited current measurements of single-carrier diodes (as described in SI).

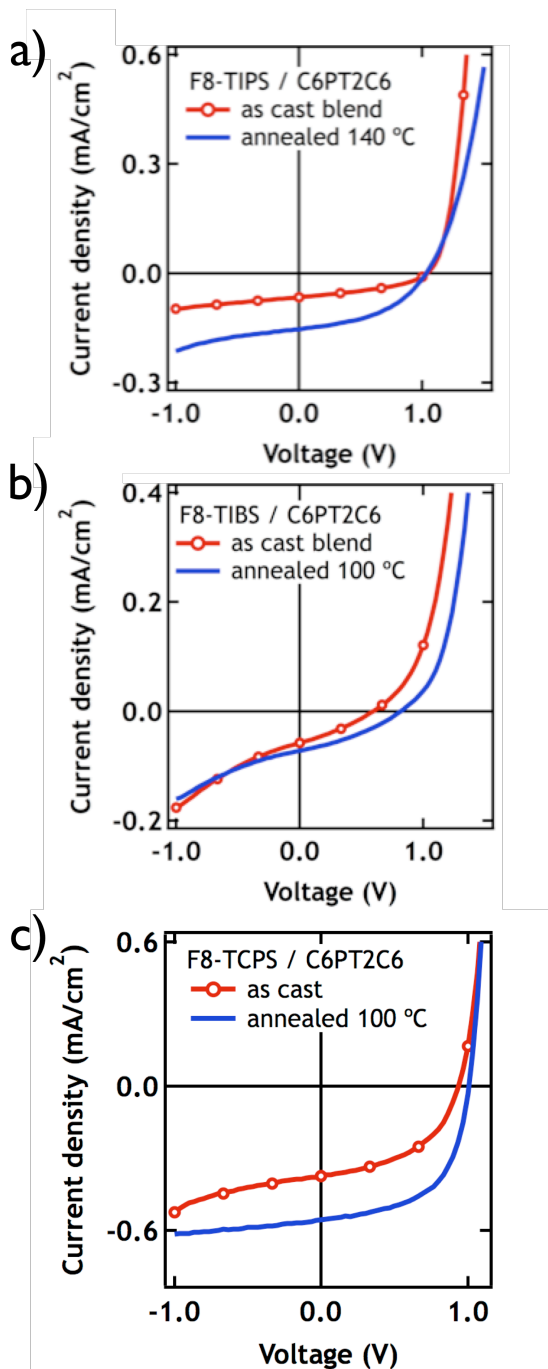


Figure 2.3. Current-voltage characteristics of the BHJs using (a) F8-TIPS, (b) F8-TIBS, and (c) F8-TCPS. All films cast at 2000 RPM for 60 s from 1.5% w/v solutions in chloroform; blend ratio 1:1 by weight. Information about the device structure can be found in the SI and the solar cell characteristics are summarized in Table 2.

iii. Molecular Ordering in Thin Films

In order to probe molecular packing and film morphology within the BHJ, grazing incidence wide angle x-ray scattering (GIWAXS) was used to determine if the donors and acceptors crystallized upon spin casting or after thermal treatment in both neat and blend films. A synchrotron source was used because high flux is necessary in structural investigations of thin films of materials with structural disorder. Additionally, the use of 2D detection allowed a large area of reciprocal space to be measured simultaneously minimizing damage done to the sample by x-ray exposure. First we outline how the donor orders in neat films, then we describe the structural changes in the donor and the acceptors when blended into BHJs.

iv. Thin Films of Donor C6PT2C6

GIWAXS from as-cast thin films (roughly 100 nm thick) of C6PT2C6 reveals that the molecules crystallize with essentially the same unit cell as the bulk crystal structure (**Figure 2.4**). The scattering peaks of the bulk structure were compared to the 2D GIWAXS data using SimDiffraction, a code developed to simulate the thin film diffraction pattern for a given crystal structure and film texture.³³ The overlay of the predicted and experimental data does not show peaks along q_z because this data is not accessible using the experimental geometry, and the simulated data shown have been calculated assuming all crystallites are perfectly oriented with respect to the substrate. Small differences in the unit cell parameters of C6PT2C6 are observed in thin films and we attributed these to the different data collection temperatures (150 K for the single crystal, 298 K for GIWAXS). Single crystal X-ray scattering of C6PT2C6 at 298 K confirmed that the volume increase of roughly 5% (2593 \AA^3 to 2722 \AA^3) is consistent with thermal expansion. It should be noted that all single crystal data were collected at cryogenic temperatures, so we expect thermal expansion to

produce small shifts in unit cell parameters relative to the single crystal structures for all the compounds in this study.

Crystallites of C6PT2C6 exhibit preferential (100) orientation in thin films (this lattice plane is rendered in **Figure 2.1**). The conjugated portion of C6PT2C6 is oriented at roughly a 20° angle to the substrate and both sets of alkyl substituents on C6PT2C6 are oriented toward the interfaces of the film with PEDOT and air. The orientational spread (or tilt angle distribution) of the crystallites in the film, as measured by the FWHM of the polar angle for the observed reflections, is ~14°. The FWHM of the (100) peak at χ 86° (near $q_{xy}=0$) gives crystallite correlation length of ~24 nm.³⁰ We note that this does not represent the FWHM of highly oriented crystallites, which are in the “missing wedge” of the grazing incidence scattering data. The atomic force micrographs (AFMs) show elongated domains (**Figure 2.14**) where the long direction of the crystallites is the direction of fastest growth, likely the *c* axis of the crystal, along which close π - π interactions are observed. Although the domains are larger than 50 nm in the AFM, the FWHM of the (020) reflection at $q_{xy} = 0.035 \text{ \AA}^{-1}$ gives a correlation length ~30 nm. This difference suggests that the domains in the AFM images are not single crystallites or that cumulative disorder destroys long-range order within them. The observation of such disorder is consequential for organic semiconductors where the orbital overlap between molecules is crucial to charge carrier transport.¹⁰⁵

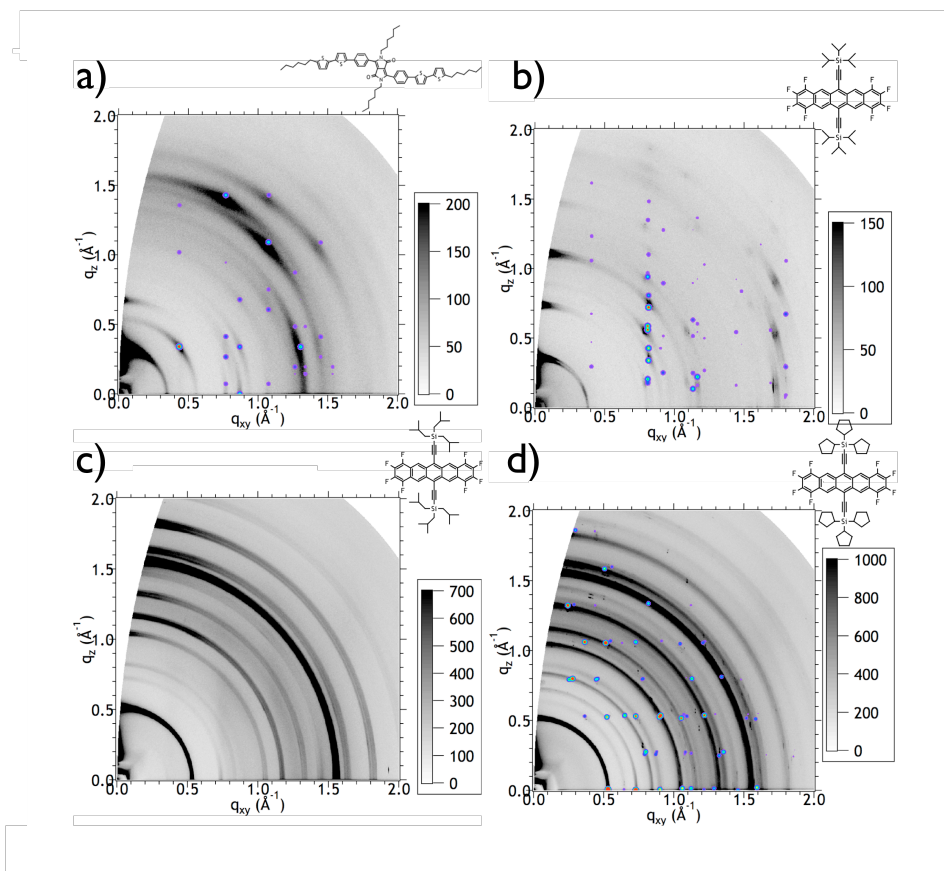


Figure 2.4. GIWAXS of neat donor and acceptor films overlaid with peaks from the bulk single crystal structure. (a) C6PT2C6; room temperature unit cell, (b) F8TIPS; bulk single crystal unit cell; (c) F8TIBS; no unit cell determined (d) F8TCPS bulk crystal unit cell adjusted for thermal expansion. Fits for adjusted unit cells can be seen as 1D plots in Supporting Information.

v. Ordering of F8TIPS in neat films and BHJs.

The acceptor F8TIPS appears to adopt a thin film structure similar to that of the bulk single crystal. We observe that all reflections along q_z appear to be split into two peaks with very similar d -spacings, and speculate that this results from the presence of a thin film polymorph, although it could also be due to scattering from the film roughness (AFM of a neat film of the F8TIPS acceptor is included in the SI). It should be noted that a similar compound, TIPS pentacene, exhibits a thin film polymorph.³⁵ While this complicates analysis, the packing in the thin film phases is similar enough to what is observed in the single crystal structure to enable us to draw some conclusions. The simulated diffraction pattern obtained from the bulk crystal structure of F8TIPS, with (001) planes oriented parallel to the substrate, is overlaid on the GIWAXS pattern in **Figure 2.4**. It is clear that the (01 l) family of reflections, which should appear as a series of peaks along $q_{xy} \sim 0.4$, is absent in the experimental data likely from a change in symmetry (i.e. the space group). The bulk unit cell of F8TIPS is similar to that of TIPS pentacene, with two salient structural differences: F8TIPS, with $Z = 2$, has b axis length almost exactly double that of TIPS pentacene, which has $Z = 1$. It is conceivable that F8TIPS could adopt a TIPS pentacene-like thin film structure in which both molecules in its unit cell are symmetrically equivalent. This would account for the missing family of reflections in a diffraction pattern that is otherwise close to what we would expect of the F8TIPS bulk unit cell. We do observe small shifts in unit cell lengths and angles as a result of thermal expansion, and it is possible that subtle shifts in molecular geometry (e.g. distortions of the acene core from planarity) could result in small changes in scattering intensity for the diffraction peaks. As expected from the crystallographic planes containing close co-facial π - π stacking, the film adopts an orientation with [001] along the surface. The tilt angle distribution of this film is about 3°,

the lowest of all the films investigated in this work, and many higher-order reflections are apparent. The crystallite correlation length, estimated by the Scherrer analysis on the (001) reflection, is around 80 nm at a polar angle of 86°.

The packing of as-cast blends of F8TIPS with C6PT2C6 shows significant differences from the neat film of either component, although thermal annealing restores the packing found in the single crystal structures of both the donor and acceptor. Our investigations for all donor-acceptor blends in this study focus on a 1:1 blend ratio, which yielded the best solar cell performance (See Supporting Information). The GIWAXS of as-cast F8TIPS/C6PT2C6 blend films shows weaker scattering than neat films, although a large number of peaks are still observable (**Figure 5**). However, these reflections do not appear to correspond to any peaks from the bulk cell of the donor or the acceptor. The ordered material in this blend has a crystallite correlation length around 25 nm based on the FWHM of the peak appearing at 0.85 \AA^{-1} . One notable feature in the GIWAXS is a very prominent peak along q_{xy} corresponding to a d -spacing of 3.51 \AA , likely indicating in-plane π - π stacking interactions. It is surprising that the as-cast BHJ adopts a structure so different from the crystal structure of either donor or acceptor; GIWAXS of the thermally annealed blend clearly shows (100) oriented C6PT2C6 and (001) oriented F8TIPS, each with crystallite orientation distribution of 7° (**Figure 2.5**; overlay of bulk structure shown in **Figure 2.16**). The donor crystallites have a correlation length around 35 nm, and the acceptor around 27 nm based on the FWHM of the (100) donor peak and the (002) acceptor peak at a polar angle of 86°. These structural changes are reflected in the UV/Vis of the blend (**Figure 2.2**). In the as-cast film, the acene has a single absorbance band around 335 nm, but after annealing the blend, the intensity of this absorbance decreases significantly and a second band appears around 370 nm. This band is also present in the neat F8TIPS film

(**Figure 2.11**) and likely arises from intermolecular interactions between acceptor molecules. AFM images (**Figure 2.5**) show what appear to be small crystallites in as-cast films, and significantly larger aggregates that appear somewhat faceted in annealed films. We note that the AFM of these films probes only the top surface and does not necessarily reflect the structural changes we see in the scattering data from the bulk. Conducting AFM data on these films mainly showed correlation with topography without significant intradomain variation (see Supporting Information).

The F8TIPS:C6PT2C6 BHJs are relatively inefficient ($< 0.1\%$ PCE) due to their very low J_{sc} (data summarized in **Figure 2.3** and **Table 2.2**). Based on AFM data alone, we might predict a decrease in J_{sc} upon annealing the blend because domains larger than the a typical exciton diffusion length (~ 5 to 10 nm for the donor C6PT2C6) should result in more recombination and less effective charge transfer.¹⁰⁶ However, the GIWAXS data correlates to the solar cell characteristics: we observe that J_{sc} doubles upon annealing, suggesting that the structural change improves charge generation with only a small increase in the FF. The electron and hole mobilities from space charge current limited diodes shows an apparent decrease upon annealing leading to both having a similar low value.

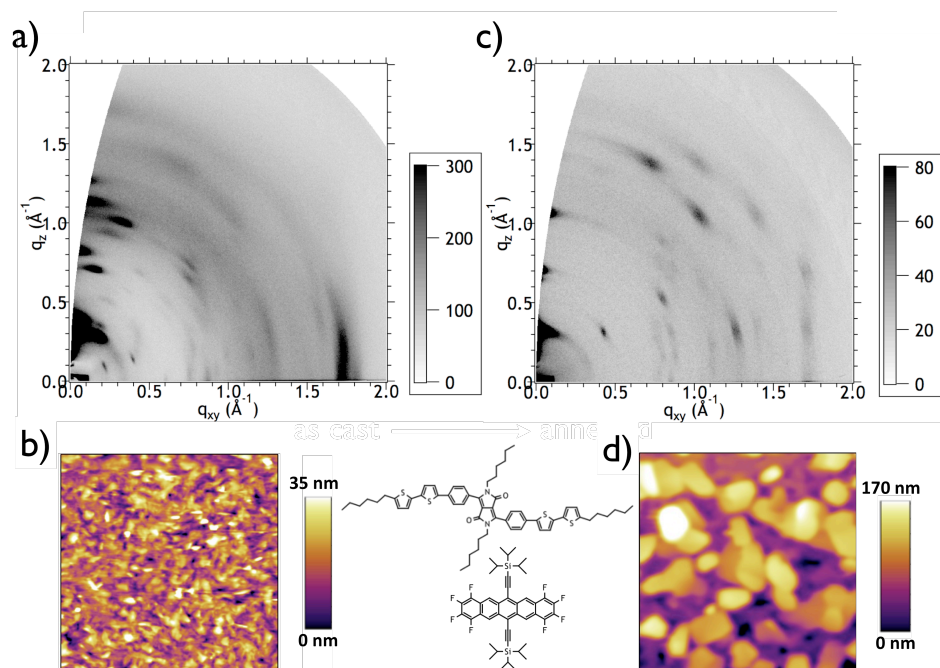


Figure 2.5. Morphological data for as-cast and annealed films of F8TIPS:C6PT2C6 (1:1 by weight). GIWAXS and AFM topography for as-cast film shown in (a) and (b); GIWAXS and AFM topography for annealed film shown in (c) and (d) (AFM images are 5x5 μm .)

vi. Ordering of F8TIBS in neat films and BHJs.

F8TIBS differs chemically from F8TIPS by only a methylene unit between the silicon atoms and each isopropyl substituent; it is the only compound for which we could not obtain a refinable crystal structure. Unlike the other acceptors in the series, the AFM for F8TIBS (**Figure 2.14**) indicates that it forms smooth, continuous films, such as those we might expect from an amorphous material. The neat F8TIBS films show a sharp absorbance around 330 nm, unlike the other acceptor films, in which this band is significantly broadened with a “shoulder” around 360-370 nm (**Figure 2.11**). We do not observe discrete spots from this compound in the GIWAXS, but we do see scattering in arcs, which indicate aggregation between molecules in a film with orientation distribution around 15° (**Figure 2.4**). (The appearance of rings results from arcs that overlap.) Among the rings, two progressions of *d*-spacings are observed, corresponding to 12.0 Å and 7.6 Å, with apparent correlation lengths of 65 and 42 nm, respectively, based on the FWHM with a polar angle of 86°. F8TIBS crystallizes with highly oriented crystallites in BHJs despite being poorly textured in thin films. Upon blending F8TIBS with the donor C6PT2C6, we observe peaks due to crystalline C6PT2C6, but no longer see scattering rings corresponding to the acceptor. Instead we observe discrete reflections, mostly near the q_z axis, with a preferred texture that we attribute to the acceptor (**Figure 2.6**). The orientation distribution of the F8TIBS crystallites is around 12°, with average thickness only about 24 nm. It is notable that the intense overlapping arcs observed off-axis in the neat acceptor film are not discernible in the blend film. It seems that the acceptor crystallizes in the blend with long-range order along q_z . Additionally, an intense peak has appeared along q_{xy} , corresponding to a *d*-spacing of 3.46 Å. This peak can be attributed to π - π stacking interactions, although it is unclear whether F8TIBS is associating with a donor molecule or with another F8TIBS molecule.

C6PT2C6 crystallites (thickness of at least 50 nm by the FWHM of the (100) reflection at a polar angle of 86° may nucleate the growth of F8TIBS, templating a particular texture of F8TIBS crystallites. This hypothesis would explain the more highly oriented F8TIBS film in the blend relative to the F8TIBS neat film because C6PT2C6 exhibits a strongly preferred orientation in nearly all films, an 11° orientation distribution comparable to its neat film. Upon annealing the film, we observe the appearance of even higher-order reflections corresponding to acceptor F8TIBS along q_z (**Figure 2.6**). No clear indication of crystallinity is observable by the topography in AFM images that indicates a relatively smooth film with no immediately apparent crystalline features (**Figure 2.6**).

While the morphology of the F8TIBS films is the smoothest of the series we investigated, and is most similar in appearance to the topography of high-performance BHJs, the short-circuit current density is the lowest of the series (**Figure 2.3** and **Table 2.2**). The PL quenching is highest for this blend in the series in agreement with the small domain sizes (See ESI Figure SX). The electron mobility of the blend is also relatively low in comparison to the rest of the series. Even with clearly evident π - π stacking interactions in the blend, and even with domain sizes approximately on the order of what is considered optimal for a bulk heterojunction, it appears that the lack of 3-D crystalline ordering within F8TIBS (we only observe higher order reflections along q_z in the blend) leads to low mobility, impeding charge extraction.

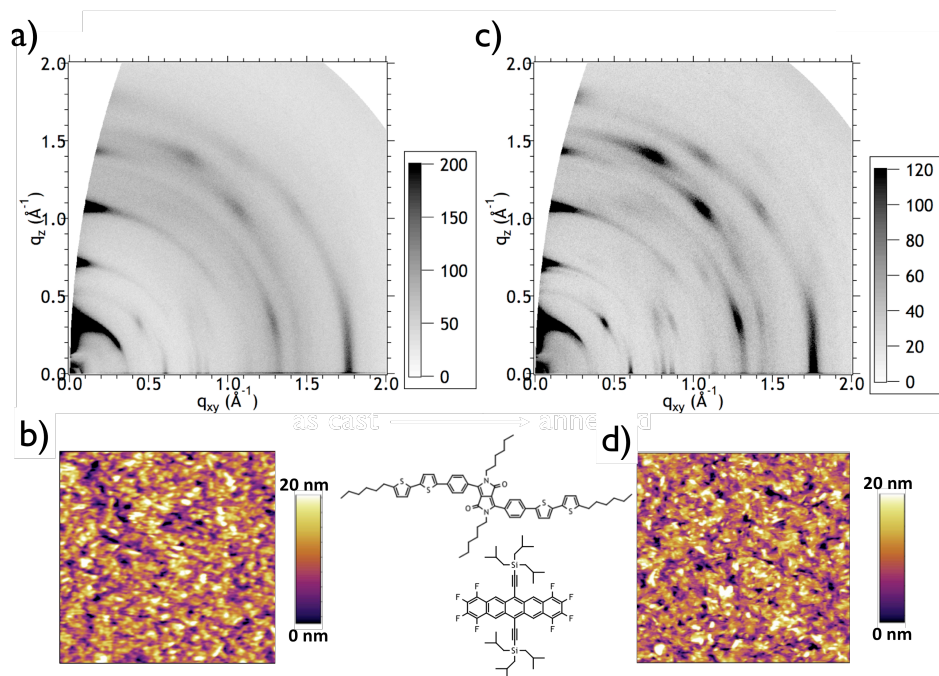


Figure 2.6. Morphological data for thin films of F8TIBS:C6PT2C6 (1:1 by weight).

GIWAXS and AFM topography for as-cast film shown in (a) and (b); GIWAXS and AFM topography for annealed film shown in (c) and (d) (AFM images are 5x5 μm .)

vi. Ordering of F8TCPS in neat films and BHJs

F8TCPS leads to highest performance in solar cells with C6PT2C6. GIWAXS of as-cast films indicates a weak preference for (110) orientation, with 22° orientational spread, and many scattering rings that overlap significantly (**Figure 2.4**). The GIWAXS data is fit well by the bulk structure with small adjustments for thermal expansion, as shown by the simulated diffraction pattern overlay and the powder figure (**Figure 2.19** and **Figure 2.20**). The relatively wide distribution of orientations for this compound is expected because several crystal faces (110 and -110, for example) should have similar surface energies because they comprise a mixture of alkyl groups and acene cores. AFM topography of the neat acceptor film (**Figure 2.14**) appears similar to that for F8TIBS, exhibiting a fairly continuous film, but some aggregates that are faceted are also present in the film.

Blending F8TCPS with donor results in a BHJ film in which the acceptor is disordered initially, but crystallize after thermal processing. In the as-cast F8TCPS blend, though, the donor is also disordered, and no clear donor peaks are present in the GIWAXS data (**Figure 2.7**). (Although a peak appears where we expect the donor (331) reflection, we do not observe other reflections for which we predict higher scattering intensity.) Thermal annealing for this blend leads to ordering of both components, producing discrete reflections with the typical (100) texture, 10° tilt angle distribution and an apparent crystallite thickness of 52 nm for C6PT2C6, based on the (100) reflection at a polar angle of 86°. (**Figure 2.7**). For F8TCPS, we observe (110) orientation with 8° spread and 38 nm crystallite thickness.

The F8TCPS:C6PT2C6 BHJs have low efficiency (PCE < 1% PCE) due to their very low J_{sc} (data summarized in Figure 3 and Table 2), but do improve upon thermal annealing. Interestingly the % PL quenching decreases with annealing from ~60% to 40% indicating

that the improved structural order of the acceptor improves the PCE mainly through more efficient charge extraction (higher FF).

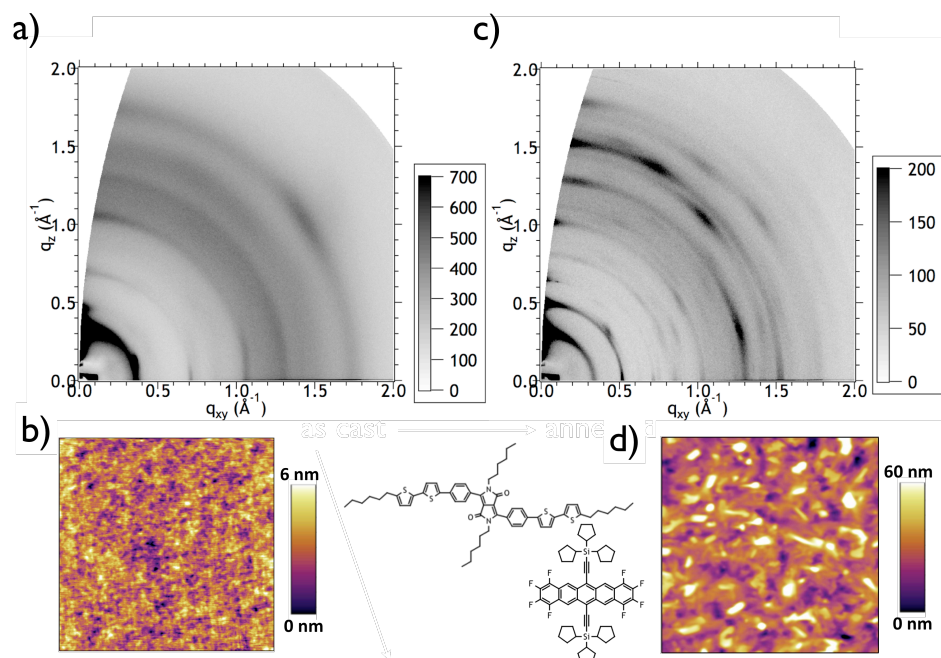


Figure 2.7. Morphological data for thin films of F8TCPS:C6PT2C6 (1:1 by weight). GIWAXS and AFM topography for as-cast film shown in (a) and (b); GIWAXS and AFM topography for annealed film shown in (c) and (d) (AFM images are 5x5 μm .)

vii. Comparison of Acceptors

Our results demonstrate that the internal molecular packing of the F8TCPS crystallites is the key to its optoelectronic performance. Of all blends studied in this series, those containing F8TCPS have the highest J_{sc} , including the as-cast blend in which the acceptor is less ordered relative to the annealed film (**Figure 2.3**; **Table 2.2**). This observation contrasts with the results for the F8TIBS blend, in which poorly ordered acceptor phases lead to low J_{sc} . An important difference in this case is that the donor domains are also disordered. Of the F8TCPS blends, the fill factor is highest for the thermally annealed films, in which the donor and acceptor are both crystalline. Thermally annealed F8TCPS blend films also have hole mobilities twice as high and electron mobilities four times as high as untreated blends. Thus we find that, as in the case of P3HT as a donor, the “sandwich herringbone” packing shown by F8TCPS produces the best performance with molecular donors.⁹⁰ The fact that this observation occurs for both a semicrystalline polymer and a crystalline molecular donor support the conclusion that the molecular packing in the acceptor is the origin.

The short circuit current is low for all of the blends studied here, but the % PL quenching is high. Therefore photophysical properties of acceptors are also as important as molecular packing. For example, TIPS-pentacene is known to undergo singlet fission and the resulting triplet state may have too low of an energy to drive the electron transfer in the BHJs studied here with high open circuit voltage.¹⁰⁷ Our results here suggest do, however, indicate that the sandwich herringbone packing allows the charges that are generated to be extracted at the contacts.

D. Conclusions

We have studied the morphology and crystallization of pentacene-based acceptors in BHJs with a diketopyrrolopyrrole-based small molecule donor. In these BHJs, both the

donor and acceptor form crystalline domains. In contrast, PCBM and other fullerene acceptors, which perform well in BHJ solar cells, are disordered. Because fullerenes have a relatively spherical shape their electronic coupling is less sensitive to molecular orientation. Our observations in this study indicate that for nearly planar small molecule non-fullerene acceptors, amorphous domains may not be advantageous for BHJs. We observe consistently low J_{sc} for blends in which a pentacene-based acceptor is disordered. Additionally, the fill factor appears to be sensitive to ordering within both components, and is highest for cases in which donor and acceptor are both ordered.

We find significant changes in molecular ordering in BHJs relatively to neat films. In as-cast BHJ films, F8TIPS exhibits a completely unforeseen structure because it is sterically unencumbered relative to the other acceptors and can associate very closely with the donor. However, after thermal annealing both the donor and acceptor revert to their bulk crystal structures demonstrating the important role of processing in establishing molecular order. F8TIBS, the second smallest, loses long-range order except in the out-of-plane direction when blended with donor, and we do not see a return of the out-of-plane reflections upon annealing. This observation, along with our lack of success in growing single crystals, indicate that it is difficult to nucleate domains of F8TIBS making it an unsuitable small molecule acceptor. F8TCPS, which is sterically encumbered, is disordered upon initial casting of a blend film, but becomes ordered upon thermal annealing. This property may allow formation of nanoscale domains subsequently providing a means to improve the crystalline ordering critical for the power conversion efficiency.

Structural characterization of organic semiconductor molecules within a biphasic BHJ is complicated due to the disorder present in thin films, but GIWAXS provides valuable insight into molecular packing and ordering within the film. Single crystal structures are

helpful in data analysis, but polymorphism in thin films can lead to unit cells that are not equivalent to those observed for bulk crystals complicating the analysis. In cases such as as-cast BHJs of F8TIPS, where a new structure is present that may contain one or both compounds present in the blend, it is very difficult to extract the molecular arrangement due to the relatively low number of diffraction peaks and question of composition. In such cases molecular spectroscopies, e.g. spectroscopic ellipsometry or polarized infrared spectroscopy, can provide insight into the molecular order.^{108, 109}

E. Materials Synthesis

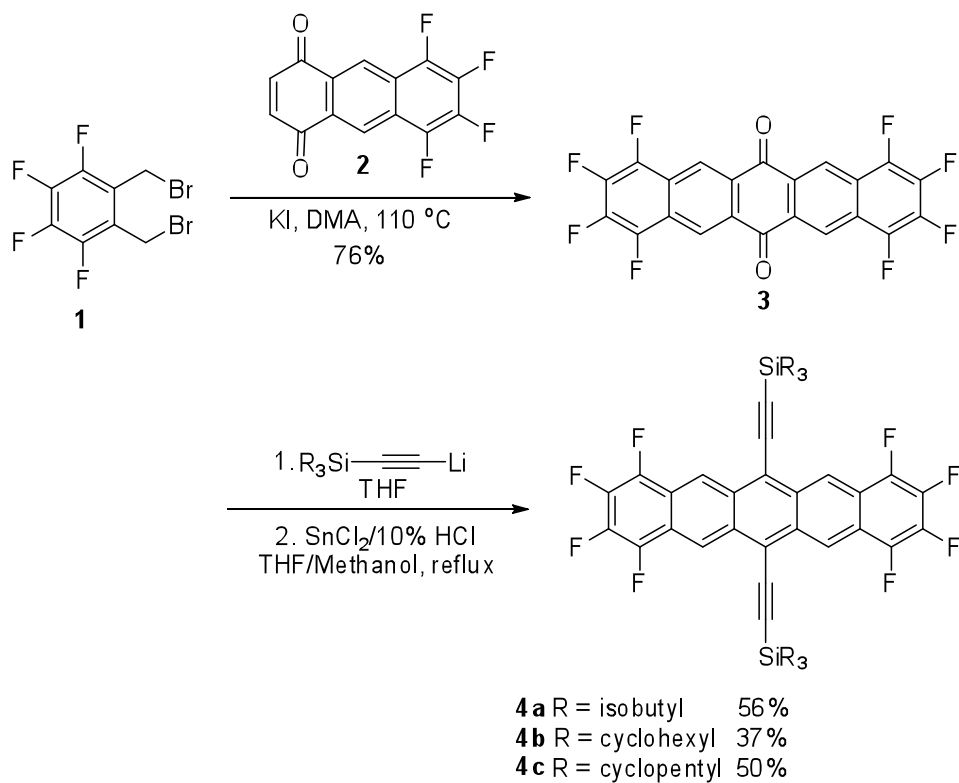


Figure 2.8. Scheme showing the synthesis of trialkylsilyl ethynylated octafluoropentacene.

Synthetic Methods.

All solvents were purchased from Pharmco Aaper except anhydrous tetrahydrofuran which was purchased from Aldrich. Chromatography was performed on silica gel (60 Å, 40-63 µm) purchased from Silicycle Inc. Thin layer chromatography was performed using Silica Gel HL TLC plates (w/UV254) purchased from Sorbent Technologies. UV-Vis absorbance spectra were recorded using Shimadzu UV-Vis Spectrophotometer model UV-2501PC. NMR spectra were recorded on Varian Inova 400MHz instrument. High resolution mass spectra were recorded in EI mode on JOEL JMS-700T MStation or in MALDI mode on Bruker Daltonics Autoflex MALDI-TOFMS. Electrochemical analysis was performed using BAS CV-50W voltammetric analyzer performed on 0.1M Bu₄NPF₆ solution in dichloromethane with ferrocene as internal standard. 1,2-bis(bromomethyl)-3,4,5,6-tetrafluorobenzene¹ and 5,6,7,8-tetrafluoroanthracene-1,4-dione² were synthesized using previously reported literature methods. Tricyclopentylsilylacetylene³, tricyclohexylsilylacetylene⁴ and triisobutylsilylacetylene⁴ were prepared by previously reported literature methods.

1,2,3,4,8,9,10,11-octafluoropentacene-6,13-dione (3)

To a 100ml RB flask equipped with a reflux condenser were added 5g of 1,2-bis(bromomethyl)-3,4,5,6-tetrafluorobenzene (**1**), 5.22g (18.6mmol) of 5,6,7,8-tetrafluoroanthracene-1,4-dione (**2**). 50 ml of degassed DMA was added and the reaction mixture was heated to 70°C. 16.56g of KI was added to the reaction mixture and the temperature was raised to 110°C. The reaction mixture was allowed to stir for 24h. During the course of the reaction yellow precipitate crashes out from solution. The hot reaction mixture was poured into 800 ml of water and allowed to stir for 30 min. The precipitate was filtered and washed with plenty of water, followed by acetone and finally with 200 ml THF.

5.16 g (77%) of the quinone was obtained as a light brown solid. MS (EI 70 eV) m/z 452 (M^+ , 100%)

**General procedure for synthesis of 6,13-bis(trialkylsilylethynylated)
octafluoropentacene (4a-c)**

To a flame dried 100 ml flask cooled under nitrogen was added 4.4 mmol of acetylene, followed by 5 ml of anhydrous THF. The reaction mixture was then placed in an ice bath. 3.98 mmol of *n*-BuLi (2.5 M solution in hexanes) was added dropwise and the reaction mixture stirred at 0 °C for an hour. 15 ml of anhydrous THF was added followed by 500 mg (1.1 mmol) of octafluoropentacenequinone (**3**). The reaction mixture was allowed to stir overnight at room temperature and was quenched with 2ml of saturated NH_4Cl solution the next day. The pentacene diol was extracted into ether, washed with water and dried over anhydrous $MgSO_4$. Removal of solvent under reduced pressure gave the crude diol which was dissolved in 10ml of THF and 40 ml of methanol. 2ml of 10% HCl was added followed by 5g of $SnCl_2 \cdot 2H_2O$ and the reaction mixture was heated to reflux. The reaction was monitored using thin layer chromatography (TLC) by following the disappearance of intermediate diol. The reaction mixture was then poured into methanol and the precipitated solids were filtered and washed with methanol. The crude pentacenes were then purified by silica gel chromatography using 100% hexanes.

6,13-bis(triisobutylsilylethynyl)-1,2,3,4,8,9,10,11-octafluoropentacene (4a)-

Recrystallized using acetone-537 mg (56%)

1H NMR (400 MHz, $CDCl_3$) δ 9.49 (s, 4H), 2.23 – 2.10 (m, 6H), 1.17 (d, J = 6.6 Hz, 36H), 0.97, (d, J = 6.8 Hz, 12H). ^{13}C NMR (100 MHz, $CDCl_3$) δ 141.93 (dm, J = 257.6 Hz), 137.69 (dm, J = 256.2 Hz), 130.81, 120.93, 120.22, 120.11 (m), 113.37, 102.99, 26.61, 25.70, 25.44. MS (LDI) m/z 866 (M^+ , 100%). Decomposition temperature-264°C

6,13-bis(tricyclohexylsilylethynyl)-1,2,3,4,8,9,10,11-octafluoropentacene (4b)-

Recrystallized using hexanes/DCM-418 mg (37%)

^1H NMR (400 MHz, CDCl_3) δ 9.55 (s, 4H), 2.06 (d, $J = 12.8$ Hz, 12H), 1.97 – 1.70 (m, 18H), 1.68 – 1.48 (m, 12H), 1.45 – 1.26 (m, 18H), 1.26 – 1.13 (m, 6H). ^{13}C NMR (100 MHz, CDCl_3) δ 141.93 (dm, $J_F = 257.6$ Hz), 137.67 (dm, $J_F = 255.8$ Hz), 130.81, 120.93, 120.19, 120.14 (m), 111.12, 103.38, 29.13, 28.60, 27.20, 23.53. MS (EI 70 eV) m/z 1022 (M^+ , 100%). Decomposition temperature - 310°C

6,13-bis(tricyclopentylsilylethynyl)-1,2,3,4,8,9,10,11-octafluoropentacene (4c)-

Recrystallized using hexanes/DCM-520 mg (50%)

^1H NMR (400 MHz, CDCl_3) δ 9.50 (s, 4H), 2.15 – 1.95 (m, 12H), 1.86 – 1.69 (m, 24H), 1.69 – 1.56 (m, 12H), 1.42 – 1.24 (m, 6H). ^{13}C NMR (100 MHz, CDCl_3) δ 141.91 (dm, $J = 257.6$ Hz), 137.66 (dm, $J = 256.2$ Hz), 130.77, 120.87, 120.19, 120.11(m), 111.20, 102.15, 29.61, 27.23, 24.00. MS (LDI) m/z 938 (M^+ , 100%). Decomposition temperature - 310°C

References for Synthesis:

Swartz, C. R.; Parkin, S. R.; Bullock, J. E.; Anthony, J. E.; Mayer, A. C.; Malliaras, G. *G. Org. Lett.* **2005**, 7, 3163.

Chen, Z.; Swager, T. M. *Org. Lett.* **2007**, 9, 997.

Purushothaman, B.; Parkin, S. R.; Anthony, J. E. *Org. Lett.* **2010**, 12, 2060.

Kamakura, J. M.; Machida, M. O. U.S. Patent 4 714 481, 1987.

F. Single Crystal Data

Material	C6PT2C6	F8TIPS	F8TCPS	F8TCHS
Crystal system and space group	Monoclinic, P2 ₁ /c	Triclinic, P-1	Orthorhombic, P2 ₁ 2 ₁ 2 ₁	Triclinic, P-1
<i>a</i> (Å)	18.157	7.718	16.454	17.150
<i>b</i> (Å)	14.465	15.545	16.516	18.719
<i>c</i> (Å)	9.938	16.875	17.259	18.826
<i>alpha</i> (°)	90.00	102.247	90.00	83.174
<i>beta</i> (°)	96.507	92.666	90.00	72.176
<i>gamma</i> (°)	90.00	91.545	90.00	67.666
Volume (Å³)	2593	1975.06	4690.18	5322.1
Z	4	2	4	4

Table 2.3. Crystallographic data from single crystal structures.

G. Fabrication of Solar Cells and Diodes

Solar cells: Pre-patterned ITO substrates (Thin Film Devices) were sonicated in soapy water for 15 minutes, then DI water for 5 minutes, then acetone for 15 minutes. The substrates were then sonicated in isopropanol for 15 minutes, dried with a stream of nitrogen, and exposed to UV-ozone treatment for 1 hour. A layer of PEDOT:PSS (Clevios P VP Al 4083, H.C. Stark) was filtered with an 0.45 μm PVDF syringe filter, applied by spincoating at 2500 RPM for one minute, then annealed at 140 °C under ambient atmosphere for 30 minutes. Substrates were then transferred into a glovebox, where the active layer blend (1.5% w/v in chloroform unless otherwise specified) was heated at 60 °C for at least one hour, cooled to room temperature, filtered through an 0.45 μm PTFE syringe filter and directly spincoated at 2000 RPM for 1 minute. Solvent annealing for select devices was performed in the glovebox thereafter, and films were placed under vacuum immediately after solvent annealing treatment. This was followed by thermal evaporation of an aluminum cathode (~ 115 nm) under vacuum ($\sim 10^{-6}$ torr), during which a shadow mask was used to produce discrete 19 mm² devices.

Processing: For thermal annealing, films were annealed on a hotplate under nitrogen atmosphere at the indicated temperature for 10 minutes, then rapidly cooled when placed on a metal surface at room temperature. During solvent annealing, films were placed in a chamber with a reservoir of solvent for a given period of time. This treatment took place in a glovebox (while continually purging with nitrogen). Samples were removed from the solvent chamber and immediately placed under vacuum to remove any traces of solvent.

Hole-only diodes: PEDOT:PSS was applied to pre-patterned ITO substrates prepared exactly as in the above section. Following the deposition of the active layer as listed above, a layer of gold (~ 90 nm) was applied under vacuum ($\sim 10^{-7}$ torr) using a shadow mask to produce 4.5 mm^2 devices.

Electron-only diodes: ITO substrates were cleaned by sonicating as above, then placed in an oven for 10 minutes. Following this, the substrates were exposed to UV-ozone treatment for an hour. Then, after sonicating again in iPrOH for 15 minutes, the devices were sonicated in a 1:5:1 mixture of $\text{NH}_4\text{OH}:\text{H}_2\text{O}:\text{H}_2\text{O}_2$ for 15 minutes. Following this treatment, the devices were rinsed individually with methanol and placed into a 1% solution of APTMS in MeOH, and left alone for one hour. The substrates were then rinsed with MeOH, gently dried under a stream of nitrogen, and transferred into the glovebox. The organic blend was applied by spincoating as above. Finally, 5 nm Ba immediately followed by 100 nm Al was evaporated onto the substrates under vacuum ($\sim 10^{-7}$ torr).

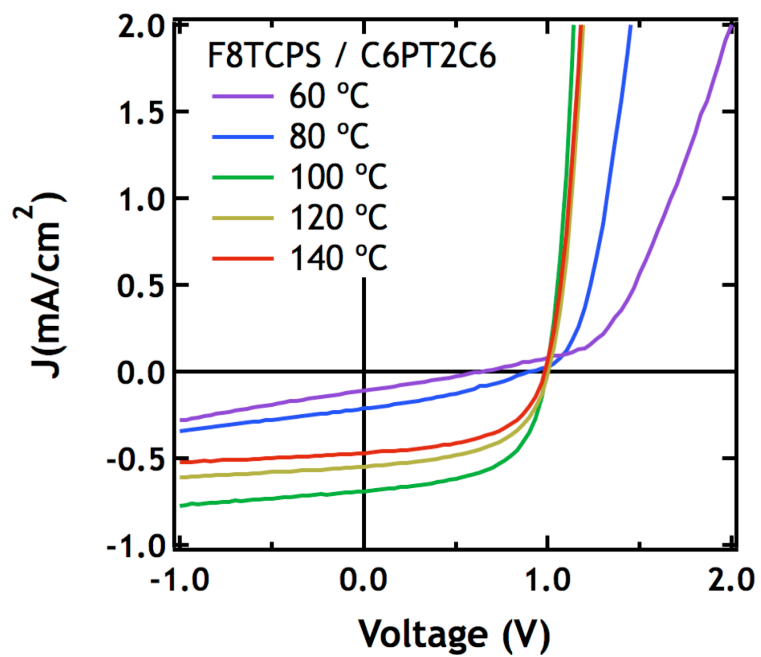


Figure 2.9. J-V curves as example data illustrating optimization of annealing temperature, using F8TCPS blend.

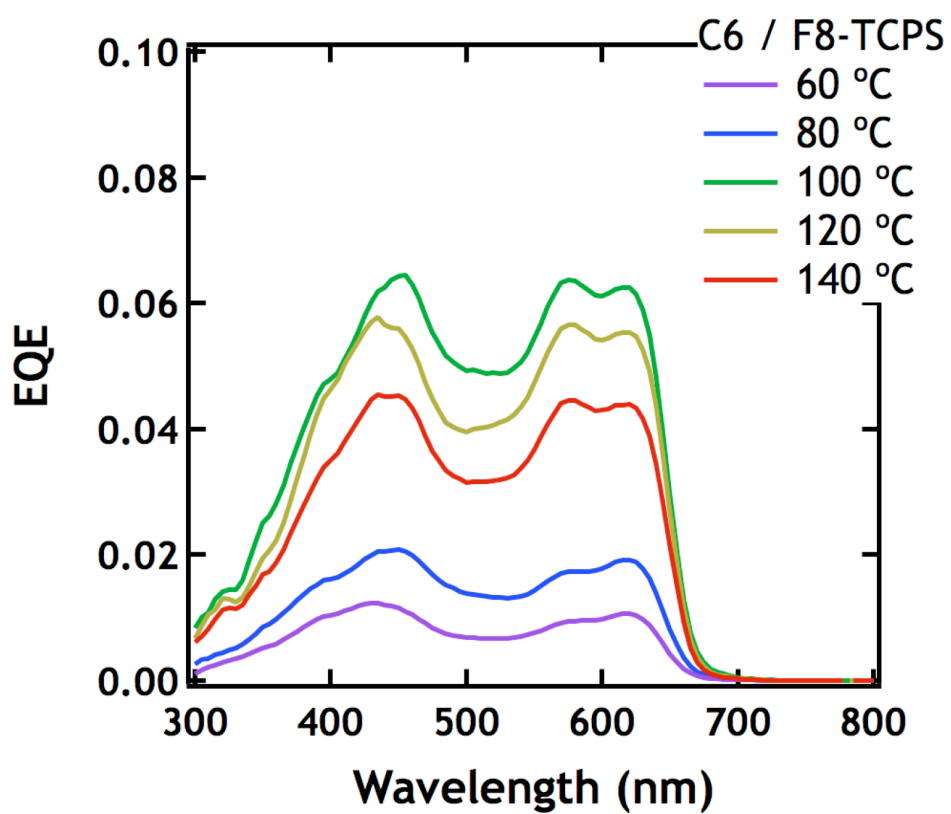


Figure 2.10. EQE curves as example data illustrating optimization of annealing temperature, using F8TCPS blend.

H. Spectroscopy

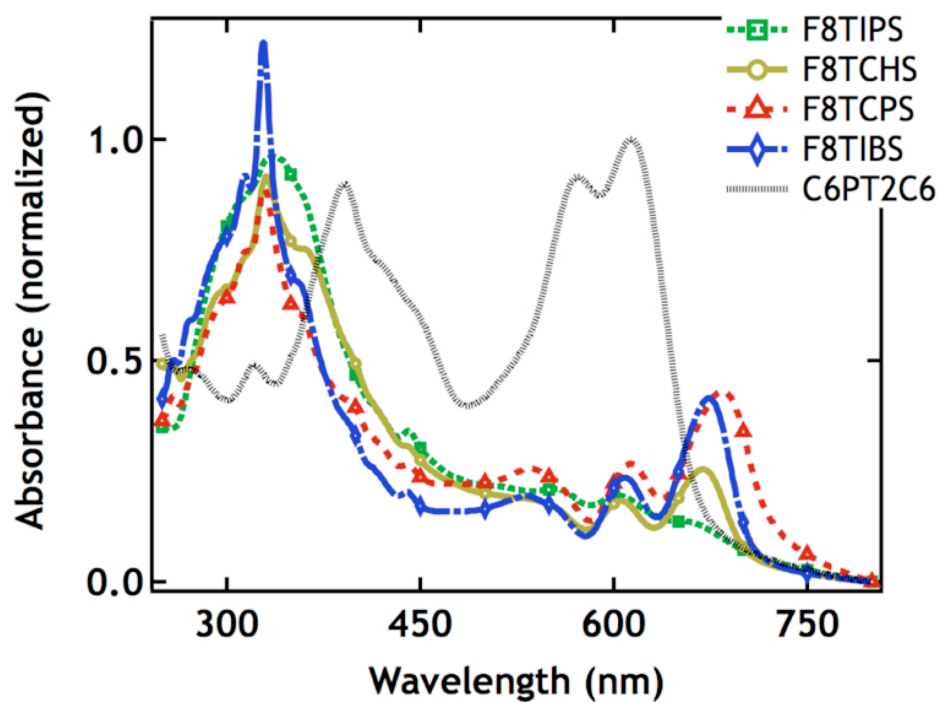


Figure 2.11. UV/vis of thin films of the neat donor and acceptors.

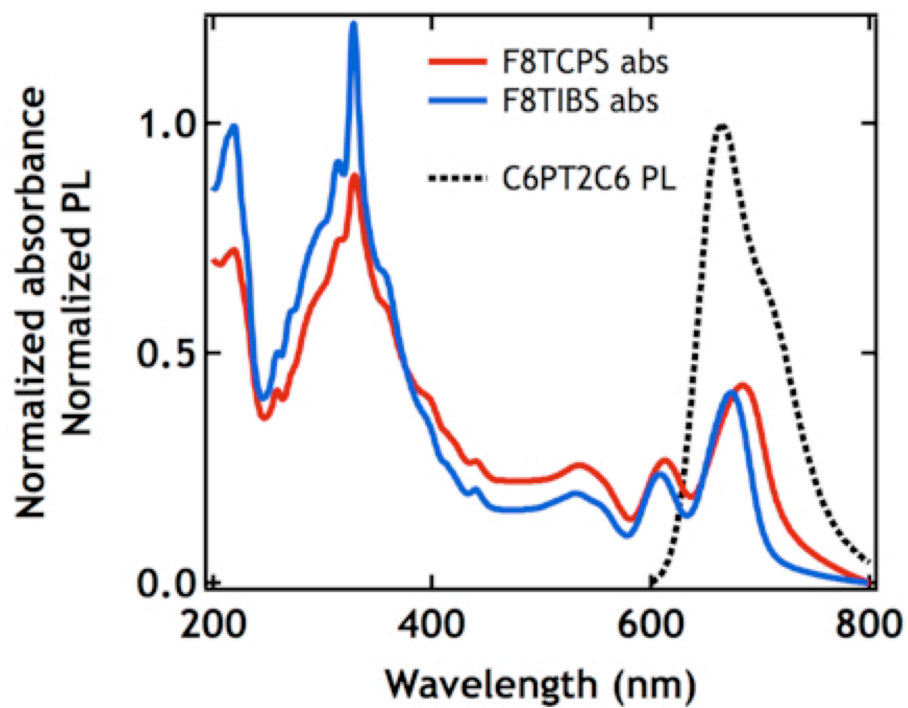


Figure 2.12. Overlap of emission of C6PT2C6 (donor) with absorption of F8TCPS and F8TIBS (acceptors).

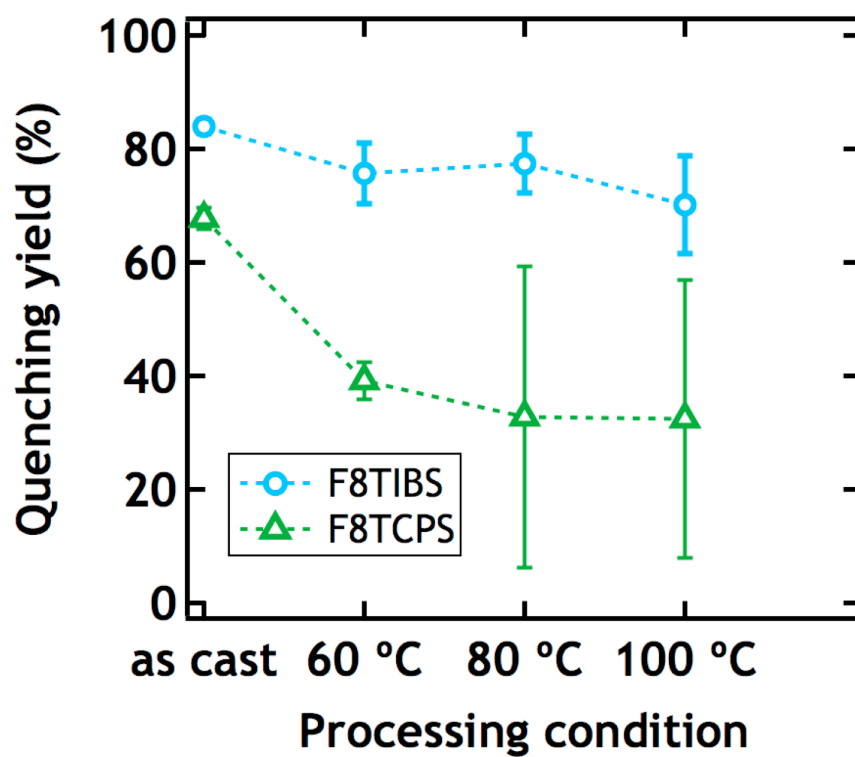


Figure 2.13. PL quenching for C6PT2C6:F8TCPS and C6PT2C6:F8TIBS blends under various processing conditions.

I. Atomic Force Microscopy

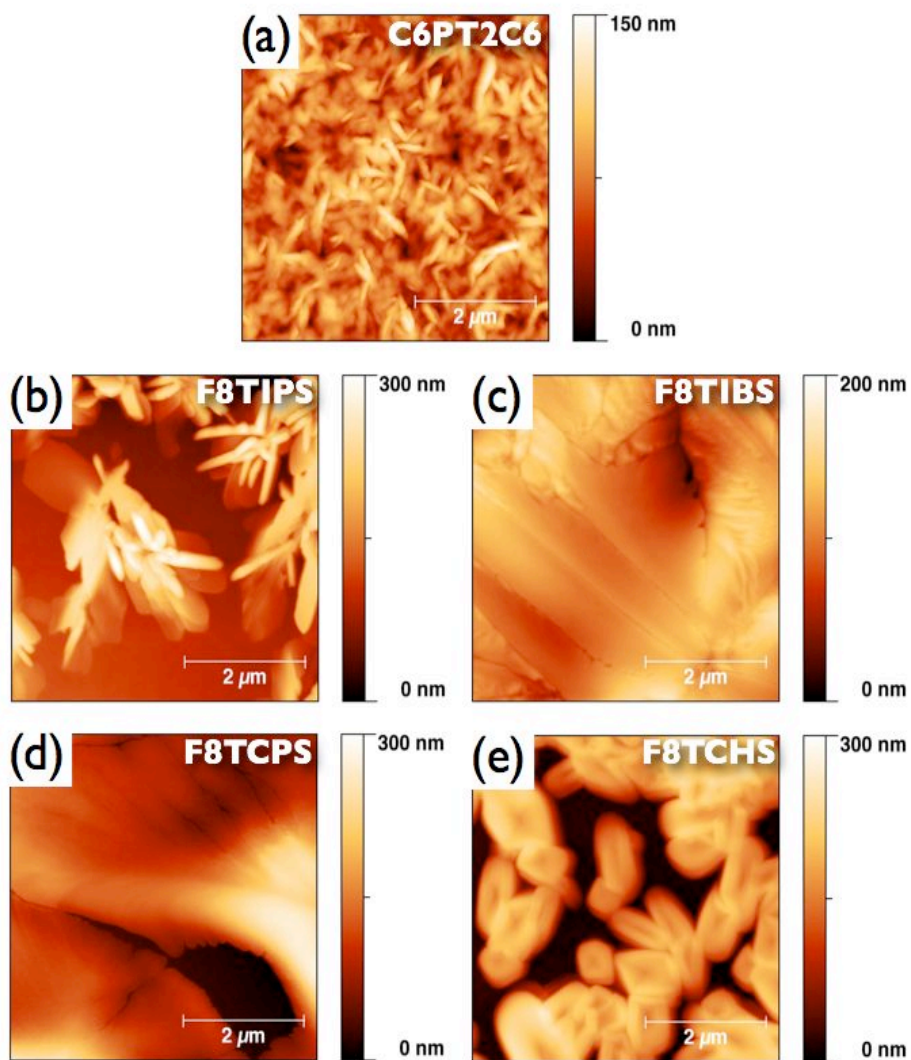


Figure 2.14. AFM of neat donor and acceptor films on PEDOT/ITO. Cast at 2000 RPM/60s from 1.5% (w/v) chloroform solutions.

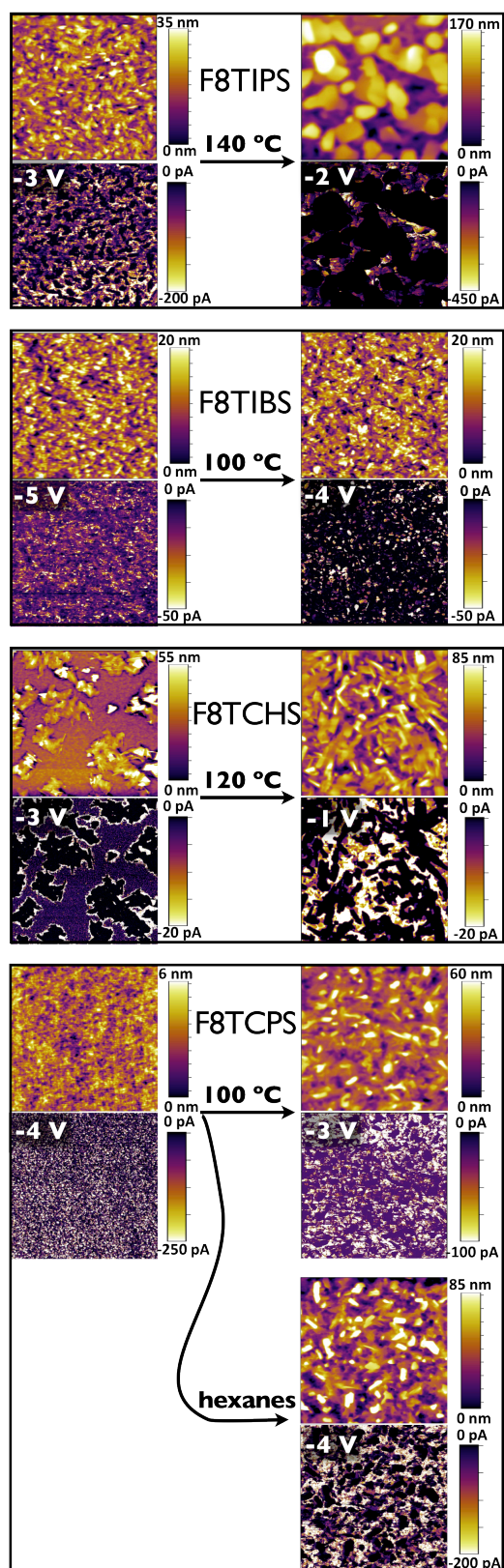


Figure 2.15. AFM and C-AFM of blends.

J. Grazing Incidence X-ray Scattering Data

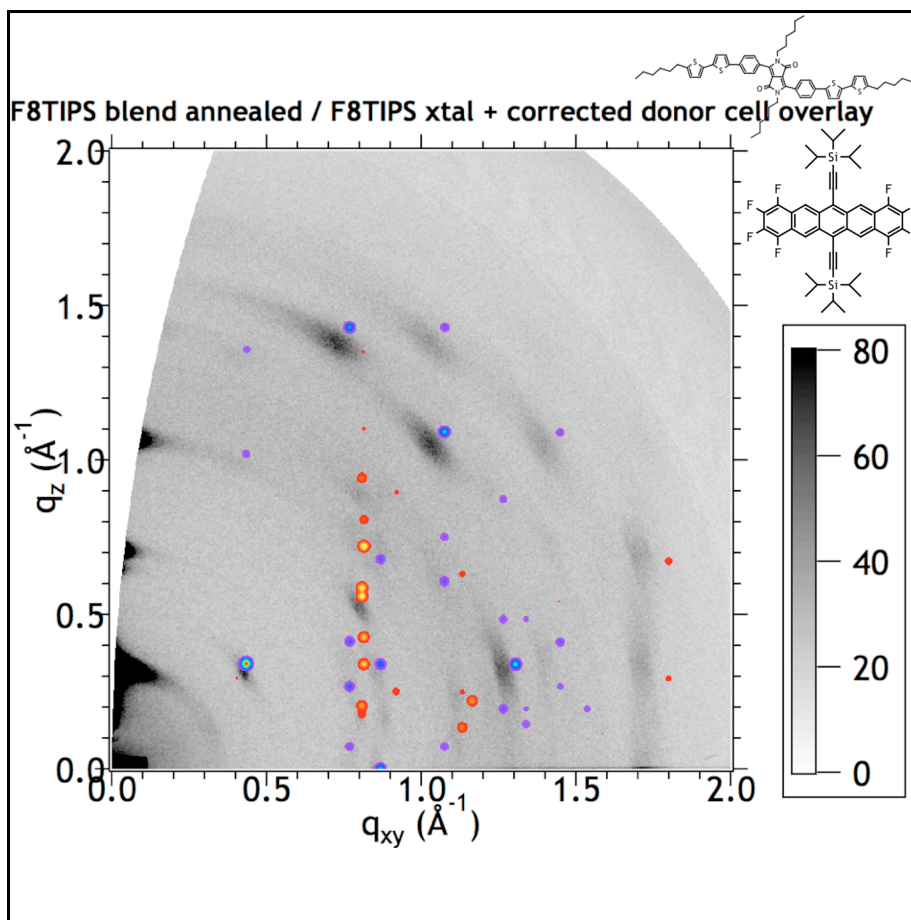


Figure 2-16. GIWAXS of F8TIPS/C6PT2C6 blend, annealed. SimDiffraction overlay shows data calculated using F8TIPS crystal structure (red to yellow spots, depending on intensity) and room temperature C6PT2C6 unit cell (purple to red spots, depending on intensity).

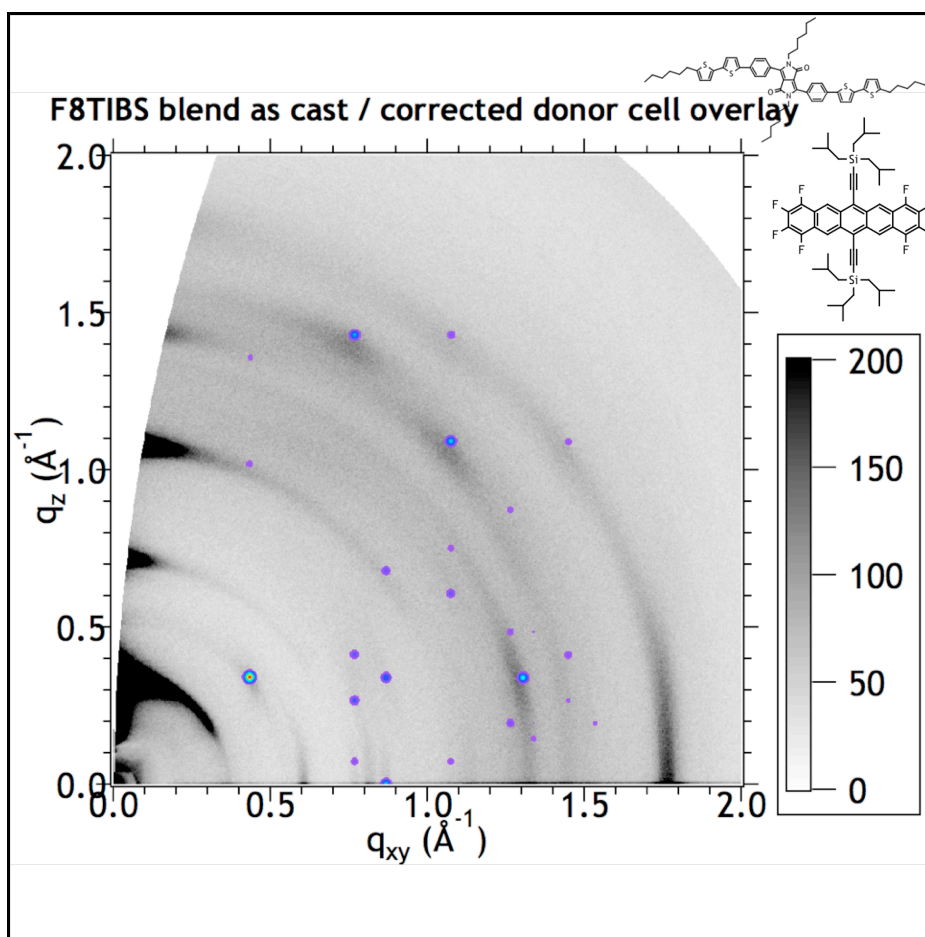


Figure 2.17. GIWAXS of F8TIBS/C6PT2C6 blend, as cast. SimDiffraction overlay shows room temperature C6PT2C6 unit cell.

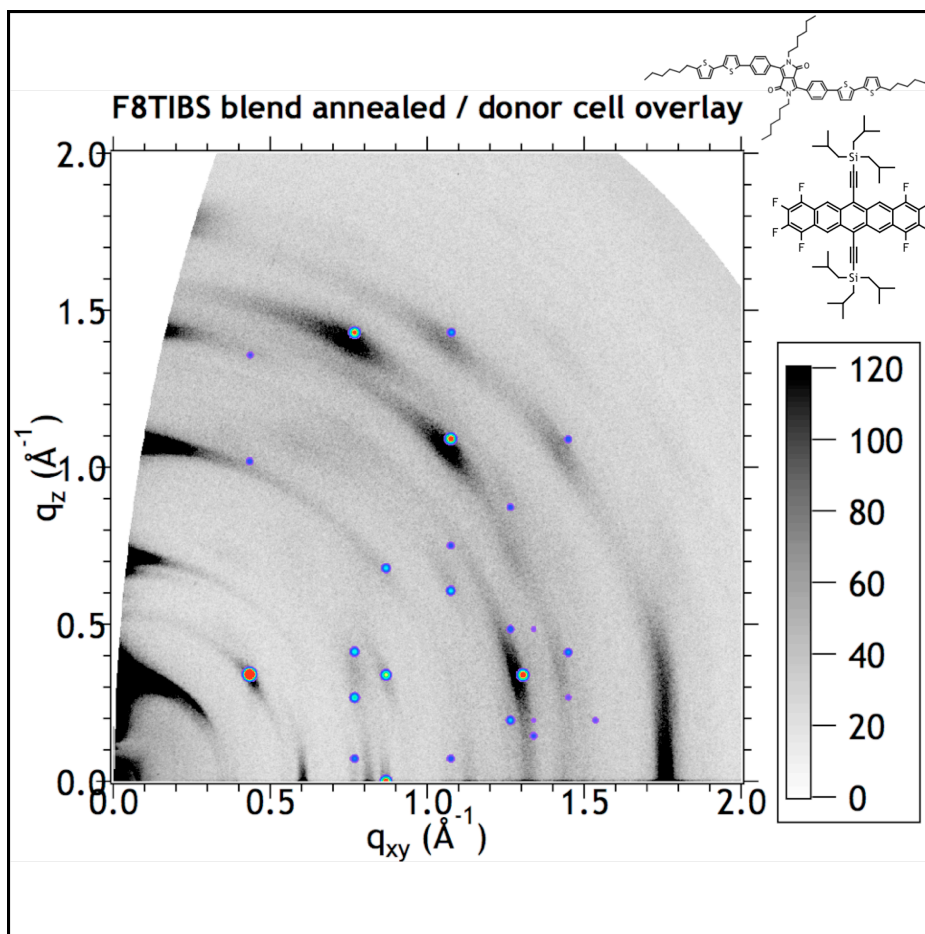


Figure 2.18. GIWAXS of F8TIBS/C6PT2C6 blend, annealed. SimDiffraction overlay shows room temperature C6PT2C6 unit cell.

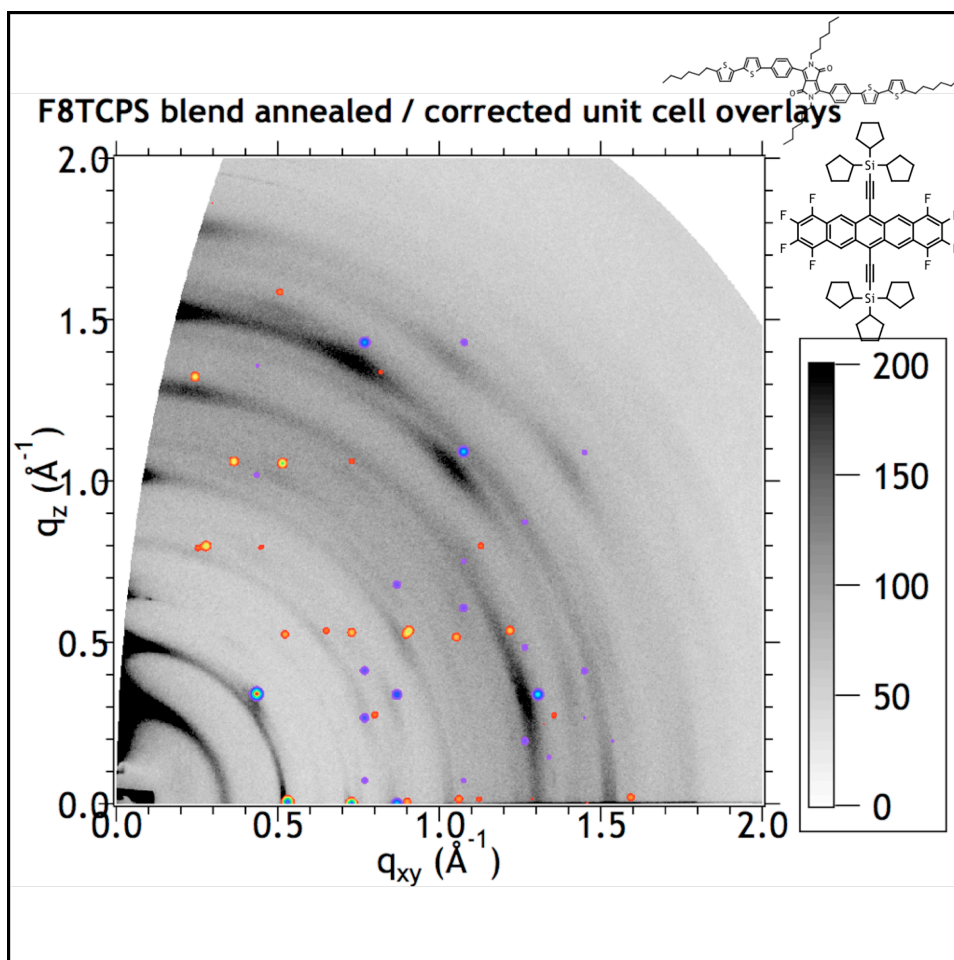


Figure 2.19. GIWAXS of F8TCPS/C6PT2C6 blend, annealed. SimDiffraction overlay shows room temperature C6PT2C6 unit cell (purple to red) and the corrected F8TCPS unit cell (red to yellow).

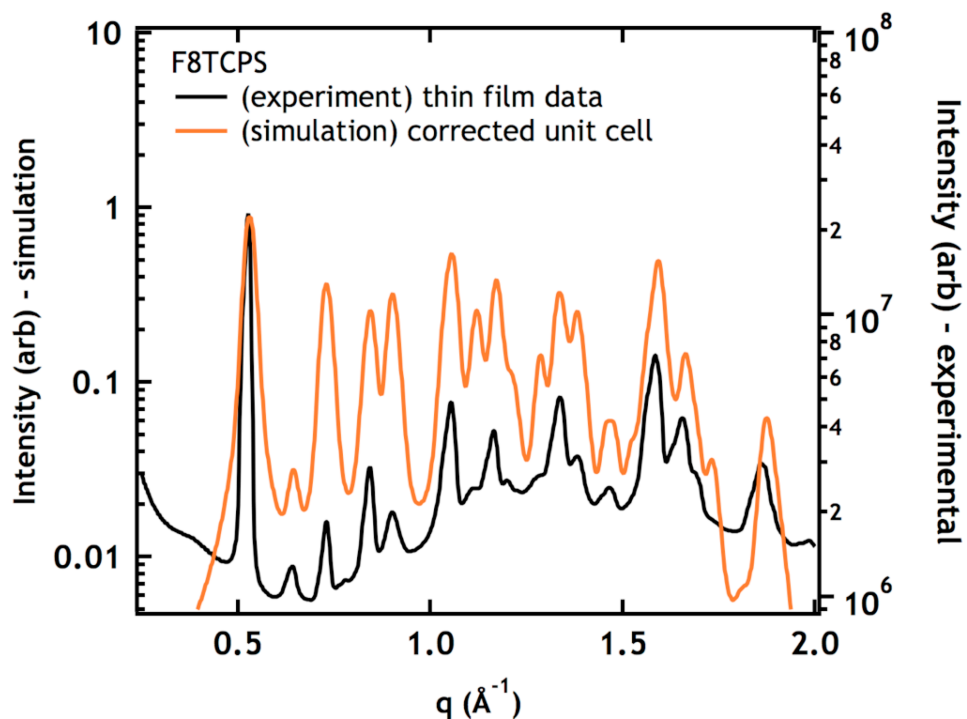


Figure 2.20. F8TCPS GIWAXS data (black) plotted against SimDiffraction data (orange) shows how well the adjusted F8TCPS unit cell fits with the experimental data. Note that SimDiffraction fails to account for paracrystalline disorder, so cannot simulate the broadening of higher order diffraction peaks.

K. Characterization of F8TCHS

Ordering of F8TCHS in neat films and BHJs.

F8TCHS contains the largest solubilizing substituent of the series of acceptors. Again, the molecules in the neat film crystallize in a similar unit cell to that of the bulk; the powder figure (**Figure 2.25**) shows the experimental data alongside the simulated diffraction pattern (in which the unit cell parameters have been adjusted to account for thermal expansion). The GIWAXS (**Figure 2.27**) features no preferred texture (orientation distribution approximately 15° at FWHM) and overlapping mixed-index arcs. Examination of the crystal packing of the compound (**Figure 2.21**) show several crystal faces with a mixture of alkyl substituents and arene ring faces, which suggests that these faces will have similar interfacial interactions. It is therefore not surprising that there should be only a weakly preferred orientation. The AFM images (**Figure 2.14**) show what appear to be randomly oriented crystallites with clear facets but inconsistent habits, consistent with the x-ray scattering.

Blending this compound with C6PT2C6 appears to disorder both components relative to their packing in neat films, as evidenced by the scattering data, which indicates broad, diffuse rings with low intensity relative to the background (**Figure 2.24**). The orientation distribution of the donor in this blend is around 50°, with average crystallite size around 31 nm. We could not determine orientation distribution for F8TCHS in the blend; there were no clearly discernible acceptor features in the GIWAXS. This presents a sharp contrast to the behaviour of the F8TIPS blend, in which ordered domains of the donor and another ordered phase appear in the as-cast film. After annealing, discrete reflections corresponding to donor and acceptor are apparent in the GIWAXS, indicating some ordered material with preferred orientation (**Figure 2.24**). The donor C6PT2C6 exhibits its typical (100) texture

with tilt angle distribution around 9° , whereas we think F8TCHS is (011) textured and exhibits 11° orientation spread. Average crystallite sizes (by Scherrer) for both components are both around 50 nm. This data nicely corroborates the AFM (**Figure 2.14**), which indicates a fairly smooth as-cast film with surface aggregates; the film appears to become more crystalline upon annealing.

The BHJs of as-cast films are very inefficient, but the PCE increases by an order of magnitude upon annealing (**Figure 2.23; Table 2.5**). As with the F8TIBS blends, we see with the as-cast F8TCHS blend that a disordered acceptor leads to very low electron mobility and low J_{sc} . The J_{sc} doubles as the film becomes more ordered, and the forward current of the diode increases dramatically. Annealing the films also leads to a doubling of the fill factor. This is likely due to improved charge extraction upon better film ordering. The J_{sc} is the limiting factor in the performance of F8TCHS blends. The domain sizes we observe (50 nm), even limited by cumulative disorder, are larger than what is thought to be the exciton diffusion length in these materials; we note that the films are also quite rough. Curiously, the UV/Vis of the as-cast F8TCHS blend (**Figure 2.22**) shows a hypsochromic shift of the acene absorbance (330 nm in the neat acceptor film vs. 310 nm in the blend). Upon annealing the blend, the peak at 310 nm is still present, along with absorption at 330 nm. It should be noted that absorption around 310 nm is observed for these acceptors in solution, so this could indicate a lack of electronic interaction for the acene chromophore of F8TCHS. This observation explains why the electron and hole mobilities of the as-cast F8TCHS blend are the lowest observed. The fact that the blends still absorb significantly at 310 nm after annealing likely indicates that the films are still significantly disordered; this disorder appears to limit the performance of the solar cells.

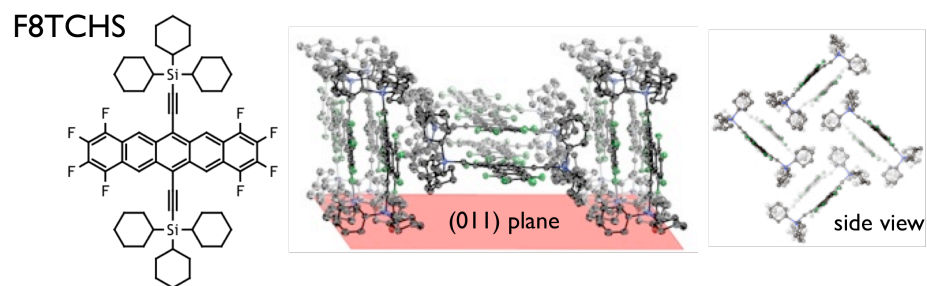


Figure 2.21. Chemical structure and crystal packing of F8TCHS. Although the poor crystal quality led to weak high-angle scattering, and the data were thus insufficient for acceptable refinement of the alkyl group disorder in the structure, F8-TCHS packs in a sandwich herringbone arrangement.

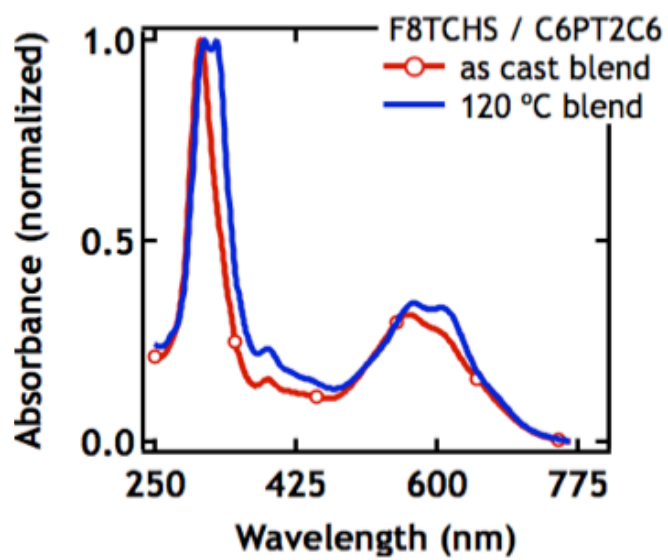


Figure 2.22. Thin film absorption spectrum for F8TCHS blended with C6PT2C6.

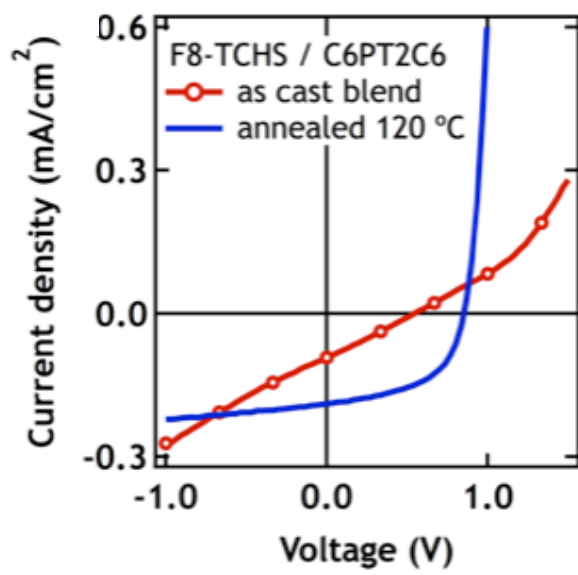


Figure 2.23. Bulk heterojunction solar cell performance of F8TCHS blend.

	F8TCHS
HOMO (eV)	5.70
LUMO (eV)	3.75

Table 2.4. HOMO and LUMO energy levels of acceptor F8TCHS. HOMO levels are determined by UPS (on thin film); LUMO levels are back-calculated using optical bandgap from thin film UV/Vis absorption edge.

	F8TCHS blend	
Condition	As cast	120 °C
V _{oc} (V)	0.53	0.83
J _{sc} (mA/cm ²)	0.09	0.19
FF	0.27	0.54
PCE (%)	0.01	0.09
μ _h (cm ² /Vs)	1.7•10 ⁻⁶	4.3•10 ⁻⁶
μ _e (cm ² /Vs)	9.0•10 ⁻⁶	4.1•10 ⁻⁵

Table 2.5. Device properties for blends of donor C6PT2C6 with F8TCHS, under various processing conditions (as cast, thermally annealed). Hole and electron mobilities were determined by making single-carrier diodes and fitting data to SCLC equation.

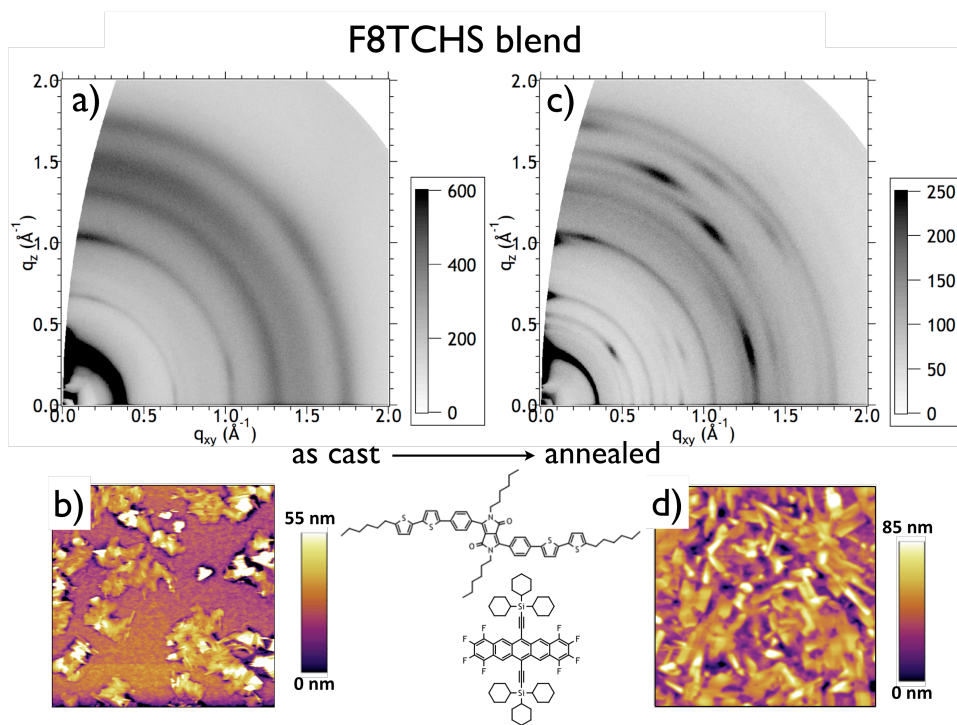


Figure 2.24. F8TCHS:C6PT2C6 blend, cast as previously noted. Blend is 1:1 by weight. As-cast GIWAXS (a) and AFM (b) on the left; annealed GIWAXS (c) and AFM (d) on the right. (AFM images are $5 \times 5 \mu\text{m}$.)

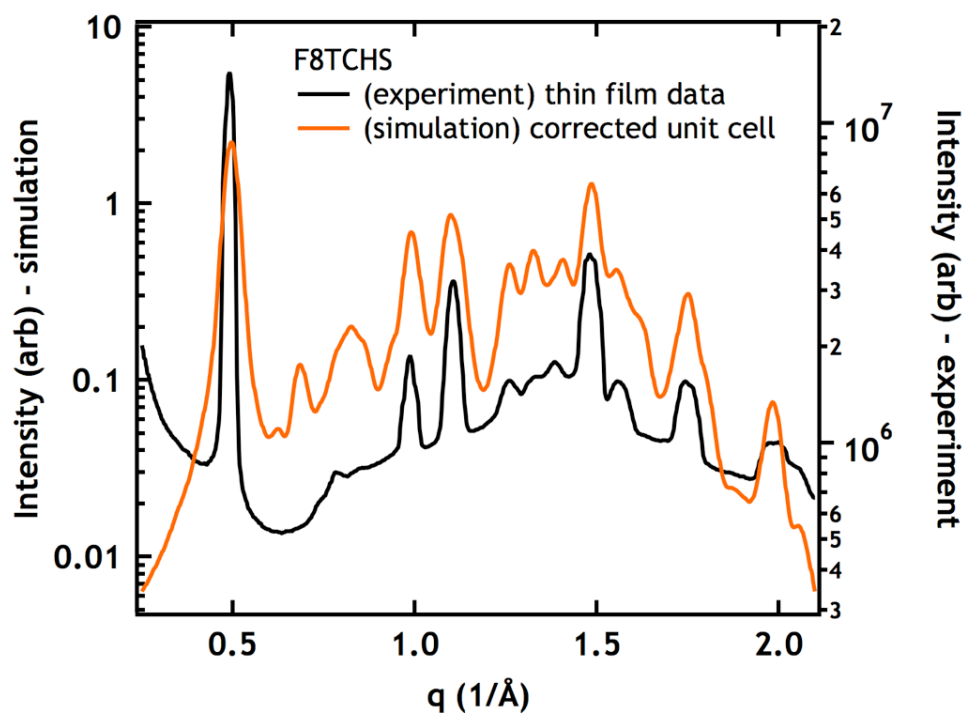


Figure 2.25. F8TCHS GIWAXS data (black) plotted against SimDiffraction data (orange) shows how well the adjusted F8TCHS unit cell fits with the experimental data. Note that SimDiffraction fails to account for paracrystalline disorder, so cannot simulate the broadening of higher order diffraction peaks.

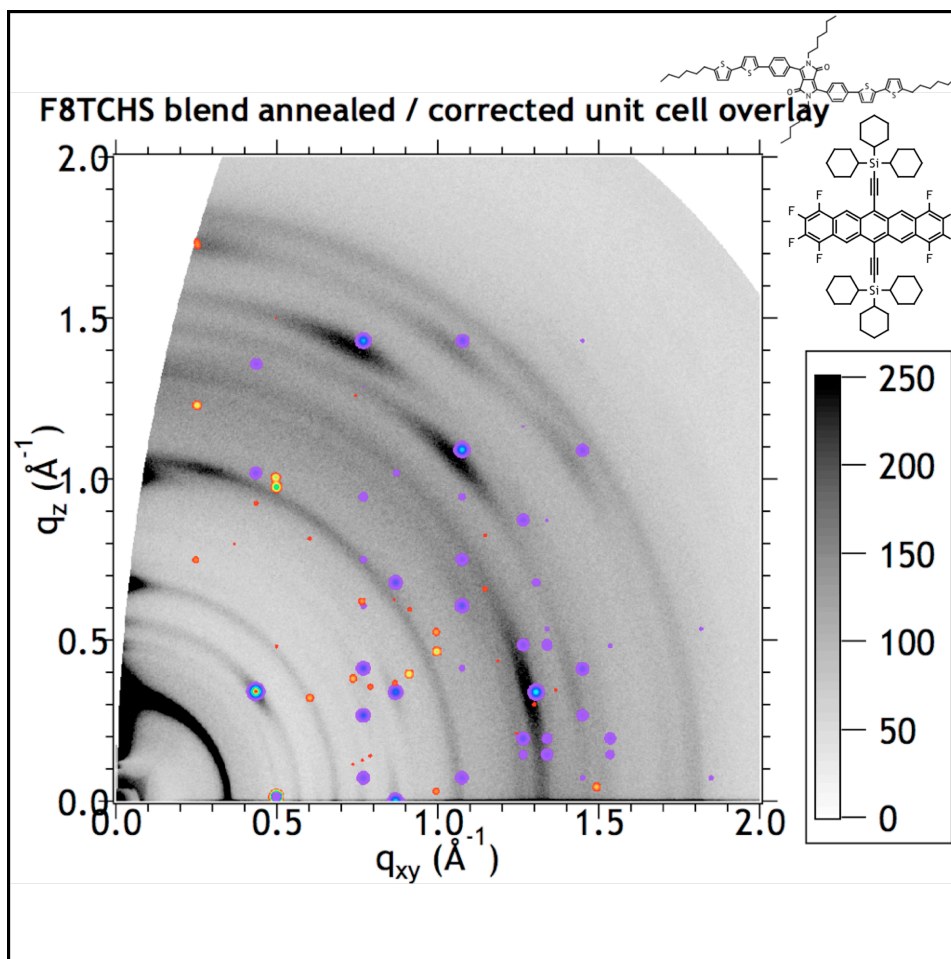


Figure 2.26. GIWAXS of F8TCHS/C6PT2C6 blend, annealed. SimDiffraction overlay shows room temperature C6PT2C6 unit cell (purple to red) and the corrected F8TCHS unit cell (red to green).

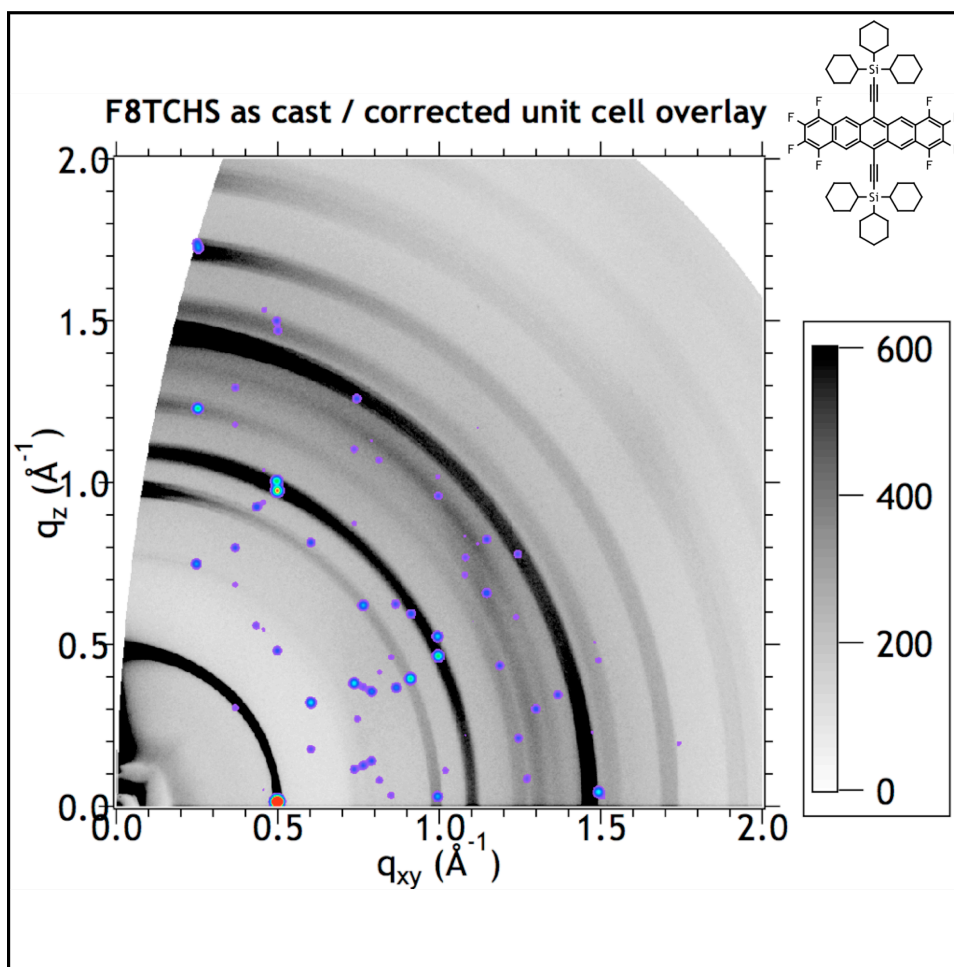


Figure 2.27. GIWAXS of neat F8TCHS film. SimDiffraction overlay shows the corrected F8TCHS unit cell (purple to red).

3. Crystalline Alloys of Organic Donors and Acceptors Based on TIPS-Pentacene

Jes B. Sherman, Kai Moncino, Tunna Baruah, Guang Wu, Sean R. Parkin, John Anthony, Michael Chabinyc

A. Abstract

The widely studied organic semiconductor TIPS Pn can be blended with its fluorinated analogue (F8TIPS Pn) to produce a crystalline substitutional alloy. Solving the structure of a series of mixed crystals containing different amounts of TIPS Pn and F8TIPS Pn provides structural information useful in analyzing thin film scattering data. The mixed films exhibit many higher-order reflections, and the peak breadths are similar to those observed for TIPS Pn films and F8TIPS Pn films. The materials appear to have sufficient geometric similarity to be miscible in all proportions without inducing long-range disorder in the solid state. Because the energy level offsets between TIPS Pn and F8TIPS Pn are similar to those found in a bulk heterojunction donor/acceptor pair, UV/vis spectroscopy and theory can be informative as to whether photoinduced charge transfer takes place in the mixed films.

B. Introduction

Organic semiconductors are frequently blended with other organic materials to form solids with functional properties. For example, blends of electron donors and acceptors lead to bulk heterojunctions used as efficient solar cells. Donor-acceptor complexes of organic compounds have been widely studied.¹¹⁰ In a donor-acceptor complex, an electronic transition from neutral D/A to charged D⁺/A⁻ leads to the characteristic “charge transfer” absorption.¹¹¹ Electronic donor-acceptor interactions are known to occur in a variety of

systems—for example, between iodine and solvent molecules, or in the widely characterized TTF-TCNQ complex.^{112, 59}

Donor-acceptor complexes, as well as mixed crystals that do not exhibit donor-acceptor interactions, have been studied intently in the organic crystal growth community. In general, two organic compounds with sufficient geometric similarity are potentially miscible in the solid state and are capable of forming solid solutions and even mixed crystals with variable composition (“alloys”).¹¹³ The addition of a second component may lead to changes in crystal habit or polymorph selection, which are important considerations in pharmaceutical research.^{38, 114} Historically, dye inclusion crystals were useful in studying crystal growth mechanisms and solid solutions.³⁷ Mixed crystals may also exhibit physical properties that differ from the parent compounds; in energetic materials, the addition of a small amount of HNS to TNT changes the crystal habit such that friable needles do not form.⁴⁶

In organic electronics, the addition of a second component to form a solid solution provides a means to introduce guests that can act as dopants, traps or emissive guests. Currently, the most technologically relevant solid solutions of organic semiconductors are in OLEDs, where a small concentration of an emissive guest is dissolved in a conductive host matrix.²¹ Historically, such model systems as Bridgman-grown crystals of anthracene doped with tetracene or acridine were used to determine trap levels and provide experimental backing to charge transport models.^{115, 52} Pentacene and perfluoropentacene have been coevaporated to produce thin films for structural studies.⁴⁸ Solution-processed thin films of F TES ADT with various additives have been used to study photoexcited charge carrier dynamics.¹⁰⁴ Many of these studies include characterization on either thin films or single crystals, but seldom both. While single crystals enable structure

determination, thin films are more relevant to device applications and may feature different polymorphs or long-range disorder not observed in single crystals.^{116, 117}

We sought to form a mixed crystal comprising materials with energy level offsets similar to those observed in high-performance solar cell materials can give insight into fundamental photophysical processes in the devices. To this end, we have selected the organic semiconductors TIPS Pn and F8TIPS Pn, shown in **Figure 3.1**. TIPS Pn has been widely researched as a thin film transistor material because it can be easily processed from solution leading to thin films with high charge carrier mobility in thin film transistors.¹¹⁸ F8TIPS, an isostructural derivative, is also highly soluble and can be processed from solution, and has been investigated as an electron acceptor in solar cells.⁹⁹ We find that these materials co-crystallize efficiently, allowing for large single crystal suitable for full determination of the molecular packing structure, and that they also co-crystallize in thin films relevant for applications in organic electronics.

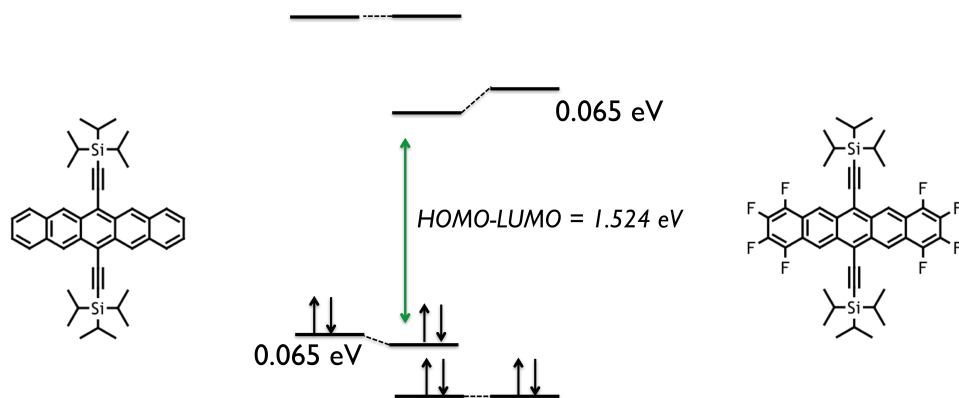


Figure 3.1. DFT calculations on a dimer of TIPS Pn: F8TIPS Pn show that frontier molecular orbitals should be slightly perturbed as the compounds are brought into close proximity.

C. Results and Discussion

i. Alloying of TIPS-Pn and F8TIPS-Pn in Single Crystals

The bulk structures of both TIPS Pn and F8TIPS Pn have been reported.^{15, 99} The two compounds are chemically similar, and both pack in a β -motif, in which only cofacial interactions are present between neighboring acene cores (**Figure 3.2**).⁹¹ The largest difference between the two structures is that there are two molecules in the unit cell of F8TIPS and one in the unit cell of TIPS Pn (**Table 3.4**). An inversion center is present in the center of the single molecule in the TIPS Pn unit cell, but the F8TIPS Pn acene core appears to deviate slightly from planarity. Thus, two molecules comprise the F8TIPS Pn unit cell, and the requisite inversion center for space group P-1 lies between them. The carbon atom density per unit cell volume is very similar for the two compounds—TIPS Pn contains 0.046 carbon atoms per \AA^3 , and F8TIPS Pn contains 0.045 carbon atoms per \AA^3 . We sought to determine if TIPS Pn and F8TIPS Pn would co-crystallize from solution, as is expected from their structural similarity.

Slow evaporation of a chloroform solution containing TIPS Pn and F8TIPS Pn produced mixed crystals of sufficient size (generally, several hundred microns on a side) for structure determination using lab-based single crystal x-ray diffraction. Pure crystals containing *solely* TIPS Pn or F8TIPS Pn were never observed after growth from a mixed solution. Changing the relative proportions of TIPS Pn to F8TIPS Pn allows reasonable control over the composition of the mixed crystals, but crystals grown from the same solution exhibit some variation in composition. We verified the composition of the mixed crystals by dissolution and analysis by HPLC using 10 mixed crystals from a particular growth run (**Figure 3.8**). We found 10% deviation from crystal to crystal; the mixed crystals contained

an average of 60% F8TIPS Pn although the growth solution contained 50% F8TIPS Pn.

This can be attributed to the lower solubility of F8TIPS Pn.

The single mixed crystals provided scattering data of sufficient quality to determine that the materials are random alloys. Splitting of individual reflections, which would indicate phase separation of TIPS and F8TIPS Pn into separate domains, was not observed. Fluorine and hydrogen atoms in the terminal rings of the acene (as well as the carbon atoms to which fluorine and hydrogen are bonded) were assigned partial occupancy. After refinement, the free variable indicating the partial site occupancy factor for the fluorine atoms was taken to indicate the fractional composition of F8TIPS Pn in the crystal. At very high fractional composition of F8TIPS, the molecular packing of the alloys closely resembles that observed in F8TIPS Pn. As the proportion of TIPS Pn in the crystals increases, the packing of the molecules in the alloy crystals becomes like TIPS Pn, with one molecule in the unit cell. Some rotational disorder is observed in the isopropyl groups—refinement of the disorder reveals that a minority of the isopropyl groups occupy sites 60° from the positions in which the majority lie. At compositions with less than 50% F8TIPS content, this freedom is no longer present, as the molecules pack more tightly with increased TIPS Pn loading—that is, the unit cell volume decreases. The carbon atom density per unit cell volume of the mixed crystals is almost identical to that of the parent compounds (0.045 – 0.046 carbon atoms per Å³). We note that the structure of pentacene/perfluoropentacene alloys has not been described in this level of detail, because no single crystals were produced.

The intermolecular packing is of interest for understanding the electronic structure of donor-acceptor interactions in solids. Benzene and perfluorobenzene are known to form complexes in the solid state.¹¹⁹ Despite the fact that single crystals of benzene and single crystals of perfluorobenzene feature herringbone packing (edge-to-face interactions), mixed

crystals of the two molecules exhibit only cofacial interactions, and the molecules alternate within a columnar stack.¹²⁰ This is attributed to the quadrupole moments of the two molecules, which are similar in magnitude but opposite in phase.¹²¹ The highly electronegative fluorine substituents in perfluorobenzene withdraw electron density to the periphery of the ring; this leaves a positive electrostatic potential in the center of the ring, which interacts with the negative electrostatic potential above and below the plane of the benzene ring adjacent in the stack.¹²² This alternant columnar stack motif is not limited to benzene and perfluorobenzene, but has also been observed in other mixtures of arenes and perfluoroarenes.^{65, 123} For example, pentacene and perfluoropentacene both crystallize with herringbone packing motifs.¹²⁴ The molecular packing of the pentacene:perfluoropentacene blend, which produces crystalline thin films, has not been characterized.

Unlike pentacene and perfluoropentacene, TIPS Pn and F8TIPS Pn both crystallize in a β -motif, with only cofacial π - π interactions, and mixed crystals containing both TIPS Pn and F8TIPS Pn also exhibit this β -motif packing.^{15, 99, 91} Relevant packing parameters for each structure are illustrated in **Figure 3.11**, and plotted against F8TIPS Pn composition in **Figure 3.2**. If molecules are represented as a centroid surrounded by four carbon atoms from the acene core, the distance between the plane of one molecule and the centroid of its neighbor does not appear to change significantly as the fractional composition of F8TIPS Pn increases. Additionally, there is no trend in the distance between centroids of neighboring molecules. The only significant difference across the series is the trend observed in the distances between carbon atoms in adjacent, coplanar terminal acene rings (illustration in **Figure 3.11**). This distance increases by approximately 1 Å across the series of structures as F8TIPS Pn loading increases. This is not surprising, because the Van der Waals radius of fluorine is larger than that of hydrogen, and carbon-fluorine bonds are longer than carbon-

hydrogen bonds.¹²⁵ A crystal structure of a tetrafluorinated TIPS pentacene derivative (F4TIPS Pn), which shares some similarities with the alloy, has been reported.⁹⁹ In F4TIPS, one terminal ring of the acene core is functionalized with four fluorine atoms. Disorder around the inversion center in the reported F4TIPS structure makes it resemble an alloy with strict 1:1 stoichiometry. The F4TIPS Pn structure exhibits packing very similar to the alloy series, with centroid-centroid distance of 7.549 Å and a centroid-plane distance of 3.377 Å. The terminal ring spacing for the tetrafluorinated TIPS pentacene structure is 4.471 Å, slightly lower than observed in the alloy structure containing closest to 50% F8TIPS Pn.

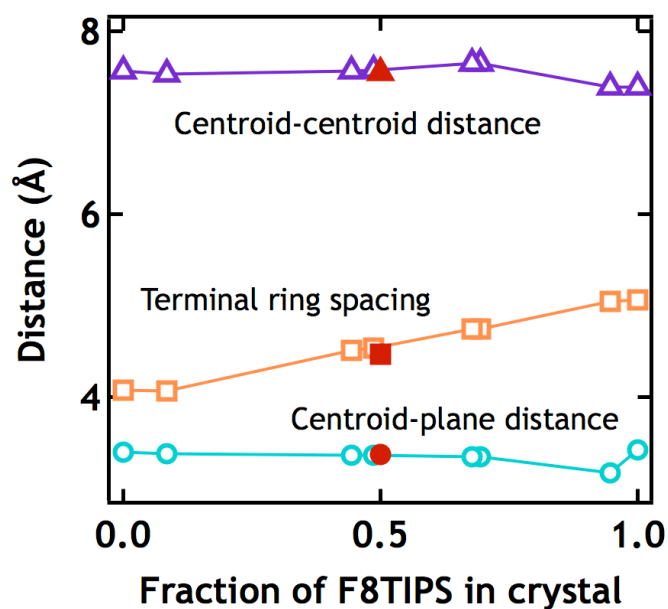


Figure 3.2. The distance between adjacent, coplanar terminal acene rings increases steadily as F8TIPS loading increases. By contrast, centroid-centroid and centroid-plane distances show little change with F8TIPS loading. The filled red symbols correspond to terminal ring spacing, centroid-centroid, and centroid-plane distances for the tetrafluorinated TIPS Pn structure.

ii. Solution Processed Films

Due to the interest in solution processing of thin films for organic electronics, we also explored the thin film structure of the donor acceptor pair. We chose to deposit the films using blade-coating from solutions similar to those used to form the single crystals. In order to examine how substitutional disorder might impact charge transport in a thin film, we cast thin films of both materials as well as mixtures of the two. We then used synchrotron source grazing incidence wide angle scattering (GIWAXS) on SSRL beamline 11-3 to examine the resulting films. Using an area detector provided 2D imaging of the scattering, and the low angular dispersion of the beam provided high resolution detection of diffraction peaks. We note that different exposure times were used for the different samples in order to avoid saturating the detector; the short exposure times used for the TIPS Pn film explain the high background. Exposure time is not indicative of film crystallinity, but is influenced by a number of factors—among them, the penetration depth of the beam, the area of film exposed to the beam, and differing structure factors and peak overlap for different materials. Because blade coating can induce directional growth in some cases, we first measured x-ray scattering with the beam parallel to the growth direction, then rotated roughly 90° to expose with the beam perpendicular to the growth direction. Because the films dried rapidly, as is evident in the optical microscope images in the SI, the domains are small enough that the beam should sample many domains with a range of in-plane orientations, and thus we expect that scattering data are not biased.

We analyzed the thin film data using our detailed information from single crystals of TIPS Pn and F8TIPS Pn. To better interpret thin film x-ray scattering data that is collected at ambient temperature, we indexed single crystals at ambient temperature. Our working assumption is that the positions of the molecules (and thus the structure factors) do not

change, and therefore that relative reflection intensities are what we would predict from the bulk structure (collected at cryogenic temperatures). We found subtle differences in the unit cell parameters due to the collection temperature difference, summarized in **Table 3.1**. In most cases, thermal expansion results in a small increase in unit cell parameter; curiously, the a axis of F8TIPS Pn undergoes negative thermal expansion. This has also been reported for pentacene.¹²⁶

	TIPS Pn	1:1 mixed crystal	F8TIPS Pn
a	7.565 / 7.71*	7.649 / 7.68*	7.718 / 7.49*
b	7.750 / 7.81*	7.723 / 7.86*	15.545 / 15.58*
c	16.835 / 16.99*	16.925 / 17.1*	16.875 / 16.82*
Alpha	89.150 / 88.39*	89.456 / 76.90*	102.247 / 76.48*
Beta	78.420 / 77.27*	78.443 / 88.35*	92.666 / 89.56*
Gamma	83.630 / 81.96*	87.889 / 86.30*	91.546 / 86.47*

* ambient temperature

Table 3.1. Unit cell parameters for TIPS Pn, mixed crystals grown from 1:1 solution, and F8TIPS Pn show small shifts from cryogenic temperature (~90-100 K) to ambient temperature (~300 K).

GIWAXS reveals that, as has been reported for thin films of TIPS Pn, thin films of F8TIPS Pn, as well as films containing TIPS Pn: F8TIPS Pn blends, exhibit preferred orientation in the out-of-plane direction, with (00l) planes parallel to the substrate.¹²⁷ An important consideration is that all materials used in this study crystallize in a triclinic space group. Because of the triclinic space group, there are no systematic absences. Many reflections correspond to d-spacings less than 0.05 \AA^{-1} apart and appear in the same spatial region of the detector, leading to significant overlap of the scattering peaks. The only progression that does not overlap with other reflections is the (00l) family of peaks. This direction cannot be probed by the area detector in grazing incidence geometry, so out-of-plane x-ray scattering was conducted on SSRL beamline 2-1.

The molecular packing in a thin film often differs subtly from what is observed in the single crystal structure, particularly for TIPS-Pn.¹¹⁶ Organic materials crystallize into polymorphic forms, and often, the phase observed in thin films can differ from the bulk crystal structures. Polymorphism in thin films has been reported for pentacene, perfluoropentacene and blends of the two, as well as for TIPS Pn.^{48, 128, 129} Vapor-deposited thin films of TIPS Pn have been reported to exhibit a thin film polymorph with packing very similar to that of the bulk structure, and shear-coated thin films of TIPS Pn have been reported to exhibit multiple polymorphs.^{116, 35} These polymorphs have the same packing motif and differ only slightly in their unit cell parameters. Due to such subtle differences in scattering peaks, high resolution detection of scattering is beneficial to determine their presence.

Analysis of the (00l) scattering peaks indicates that drop-cast films of TIPS Pn, F8TIPS Pn and a blend thereof each contain two polymorphs. In the case of TIPS Pn and the blend

film, one polymorph can be attributed to the bulk crystal structure, but F8TIPS does not appear to crystallize in its bulk crystal structure in thin films.

Because the crystallites in thin films are small and tend to be more defective relative to single crystals, blending two materials could, conceivably, lead to long-range cumulative lattice disorder.^{30, 117} For example, in bulk heterojunction films used in organic photovoltaics, even if both components are crystalline in neat thin films, multiple phases are present in the blend, and molecular ordering is poor. The width of the scattering peaks can provide information about the size of the crystallites and the quality of order within them. Analyzing for disorder in the neat TIPS Pn and F8TIPS Pn films provides a baseline for comparison with the blended TIPS Pn: F8TIPS Pn film. Upon first glance for the WAXS data, there are many higher-order reflections apparent in the blend, as there are for TIPS and F8TIPS films. If paracrystalline disorder affected this blend film to the same extent as it does most polymers, oligomers, and bulk heterojunction blends, we would expect to see few (if any) higher-order reflections due to broadening.

Examining the peak width for a progression of reflections can provide information about crystallite size and strain. A clear (00l) progression, to at least (007), is observed in the specular scattering data (**Figure 3.7**) for TIPS Pn, F8TIPS Pn and a mixed film containing both components. Peak fittings were conducted under the assumption that two phases were present for each material. As seen in **Figure 3.3**, TIPS Pn and F8TIPS peak FWHM for both phases steadily increases with peak order. The alloy, on the other hand, shows peaks that broaden and subsequently become more narrow. The higher order scattering peaks of the alloy film exhibit FWHM as low as is observed for TIPS Pn, which indicates that the alloy is not significantly more disordered than its constituent compounds in the out-of-plane direction. This makes sense upon examining the crystal packing—(00l) planes are made up

of two-dimensional sheets of molecules with π - π overlap, and are separated by bulky TIPS substituents. Thus, we expect that two adjacent (001) sheets can still overlay nicely if we substitute F8TIPS Pn molecules for TIPS Pn. It makes more sense that ordering between in-plane or mixed-index lattice planes might be destroyed upon substitution.

Beyond the (001) reflections, analysis is complicated by the fact that all unit cells in this investigation are triclinic, and two polymorphs are present in each thin film. While it would be most useful to compare widths of reflections with the same Miller indices, this is not always possible—using low-intensity reflections will result in greater error in peak fitting. It is important to note that the Miller indices for reflections shown in **Figure 3.4** and listed in **Table 3.2** are estimates based on simulated scattering data using bulk unit cells at ambient temperature (**Table 3.1**). The diffraction patterns for TIPS Pn and the mixed films correspond well to simulation, but for F8TIPS Pn, the thin film unit cell dimensions and structure factors are significantly different. Therefore, we selected reflections for F8TIPS Pn that were in the same region of the detector as selected reflections for TIPS Pn and the mixed films, and that were also sufficiently intense. While we attempted to select reflections that were sufficiently isolated (according to bulk structures) to resolve well, peak widths may still be overestimated, and therefore coherence lengths in **Table 3.2** (based on the Scherrer equation) are likely underestimated.

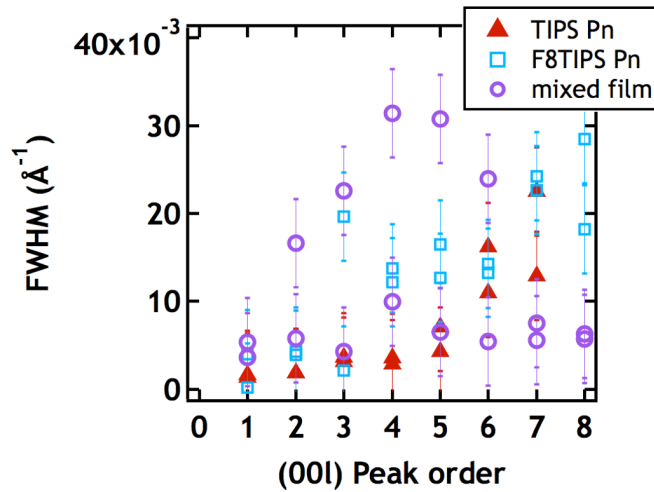


Figure 3.3. Plotting peak FWHM for both phases of TIPS, F8TIPS and the mixed film indicates that substitution does not induce significant disorder in the out-of-plane (00l) scattering direction.

Analysis of peak breadth by order for reflections in selected regions of each diffraction pattern indicates that the alloy film exhibits disorder comparable to that observed in TIPS Pn and F8TIPS. Cumulative fluctuations in lattice positions shorten the length over which the lattice is coherent; broader peaks indicate greater lattice plane parameter variation in a particular crystallographic direction. The effect of this disorder on transport has been reported.¹⁰⁵ Different polymorphs of the same material can exhibit different coherence lengths for the same lattice plane—for example, peak breadths differ slightly for both TIPS Pn peaks in region B, which we believe to be the (211) reflections for the bulk phase and the thin film polymorph. In region A (**Figure 3.4**), peak widths for the alloy film are slightly broader than those observed for TIPS Pn or F8TIPS Pn (**Table 3.2**). In regions B, C, and D, however, the alloy film exhibits coherence lengths on the same order as F8TIPS Pn. Curiously, only one reflection was observed for TIPS Pn in regions A (010) and C (032), although we do also expect to see a second peak contributed by the other polymorph—we are unable to resolve these reflections. Uncertainty in peak fitting arises when reflections overlap significantly, as is the case here. From variation in FWHM from repeatedly fitting the same two overlapping peaks, we can establish that coherence lengths for the alloy are not significantly different than those for TIPS Pn and F8TIPS Pn—they are within error. This is not surprising, given that we were able to grow mixed crystals with a wide range of F8TIPS composition.

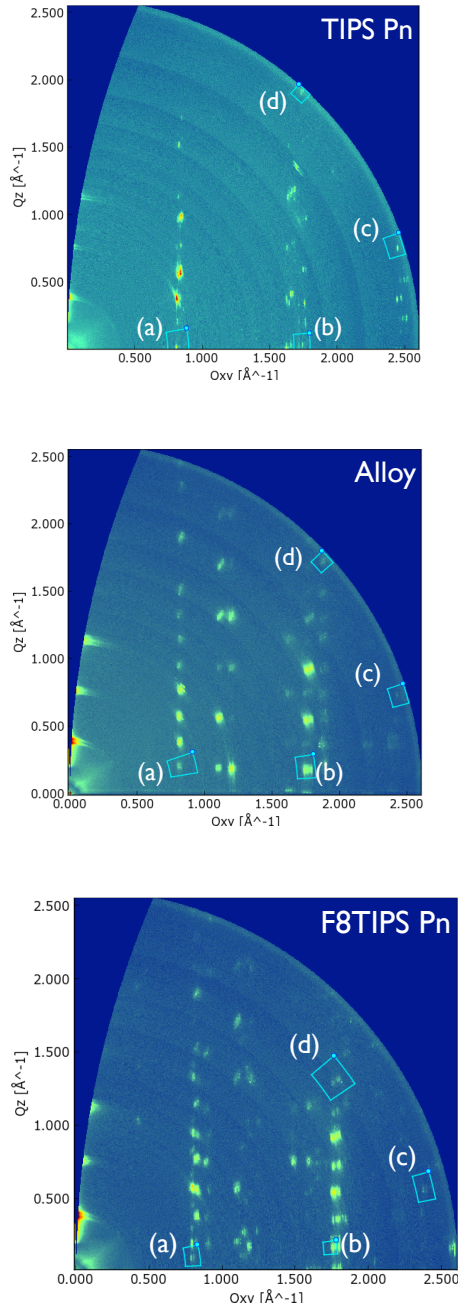


Figure 3.4. In the scattering data collected for TIPS Pn, a mixed film, and F8TIPS Pn, the four clusters of peaks indicated as (a), (b), (c) and (d) have fitting results shown in Table X. (Analysis was conducted on scattering frames as shown in the SI, collected with the incident beam parallel OR perpendicular to the growth direction of the film, but this figure shows the sum of these data for the sake of simplicity.)

Material	Region	Reflection?	Peak position (\AA^{-1})	FWHM (\AA^{-1})	Correlation length (\AA)
TIPS	A	(010)	0.805	0.007	1601
alloy	A	(0-10) (011)	0.828	0.021	533
alloy	A	(0-10) (011)	0.847	0.024	465
f8	A	(021)? (-1-10)?	0.789	0.010	1121
f8	A	(021)? (-1-10)?	0.808	0.013	862
TIPS	B	(211)	1.710	0.008	1410
TIPS	B	(211)	1.740	0.006	1881
alloy	B	(211) (-2-10)	1.741	0.014	806
alloy	B	(211) (-2-10)	1.750	0.013	868
f8	B	(-2-10)?	1.760	0.015	753
f8	B	(-2-10)?	1.777	0.010	1129
TIPS	C	(032)	2.555	0.009	1268
alloy	C	(-302)	2.531	0.019	600
alloy	C	(-302)	2.579	0.043	265
f8	C	(1-50)?	2.435	0.017	670
f8	C	(1-50)?	2.455	0.012	949
TIPS	D	(-1-25)	2.571	0.015	761
TIPS	D	(-1-25)	2.589	0.006	1903
alloy	D	(2-14)	2.549	0.049	233
f8	D	(2-23)?	2.176	0.029	391
f8	D	(2-23)?	2.220	0.034	334

Table 3.2. Peak fittings for reflections indicated in **Figure 3.4**.

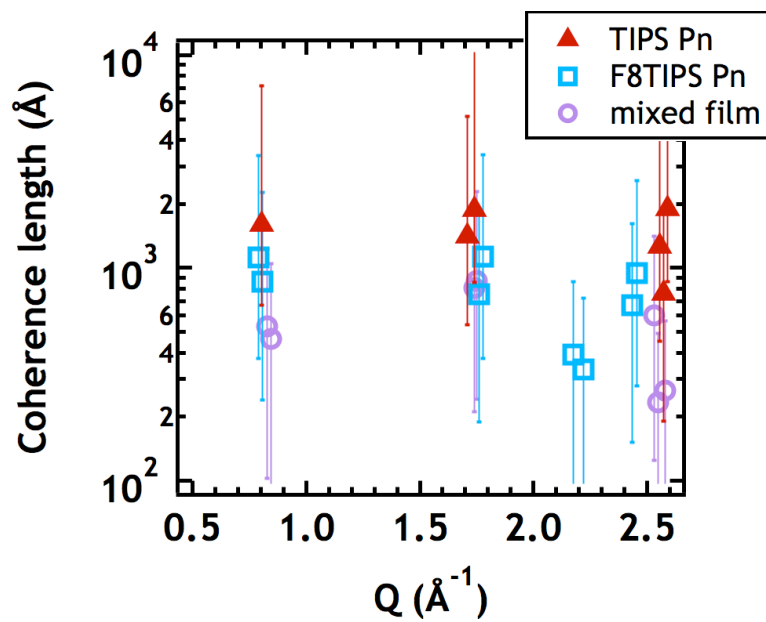


Figure 3.5. Coherence lengths for mixed films, based on in-plane peak widths, generally fall within the range of error for TIPS Pn and F8TIPS Pn. We cannot say thin films of the alloy are any more disordered than films of its constituent materials.

In contrast with TIPS Pn:F8TIPS Pn blends, pentacene:perfluoropentacene thin films have been reported to grow mixed phases with strict 1:1 stoichiometry.^{128, 130} Codeposited pentacene:perfluoropentacene thin films exhibit more microstrain and smaller island sizes than films of the neat materials.^{48, 128} Additionally, the low intensity of the higher-order reflections and the breadth of the in-plane scattering peaks suggest that long-range order is perturbed.¹²⁸ By contrast, our results show similar coherence lengths (within experimental error) for TIPS Pn, F8TIPS Pn and mixed films. The bulky TIPS substituents give TIPS Pn and F8TIPS Pn a higher degree of isostructurality than pentacene and perfluoropentacene. Increased geometric similarity should lead to less perturbation of long-range order in mixed TIPS Pn:F8TIPS Pn films, and the two compounds should be miscible over a greater composition range than pentacene:perfluoropentacene.¹¹³

An in-depth analysis of molecular geometry with respect to packing, conducted using the XPac software, confirms this suspicion with a quantitative dissimilarity index.¹³¹ The dissimilarity index compares the angles and interplanar spacings between two or more crystal structures, and returns a value near 0 in the case of isostructurality. Polymorphs with similar packing often return low dissimilarity indices; compounds in which significant geometric differences (such as large vs. small substituent size) exhibit large dissimilarity indices, if any similarity can be found at all.¹³² Comparing the 22 carbon atoms in the acene core of TIPS Pn and F8TIPS Pn using XPac returns a dissimilarity index of 4.0, whereas comparing the same 22 carbon atoms between pentacene and perfluoropentacene yields a large dissimilarity index of 12.5. The van der Waals radius of fluorine is larger than that of hydrogen, and the C-F bond is longer than the C-H bond. However, pentacene and perfluoropentacene are smaller molecules than their silylethynylated counterparts; the TIPS

substituents in TIPS Pn and F8TIPS Pn impart so much volume that structural differences resulting from the substitution of fluorine for hydrogen have much less impact on packing.

iii. Electronic Structure of Donor-Acceptor Co-Crystals

The electronic interactions between TIPS Pn and F8TIPS Pn are expected to influence optical properties in the co-crystals and mixed films. Photoluminescence is a good probe of charge transfer interactions, as reported previously for Pn/FPn.¹³³ Unfortunately, as other groups have previously reported, TIPS Pn is not photoluminescent in the solid state.¹⁰⁴ F8TIPS Pn suffers the same problem in the solid state, and also has a fluorescence quantum yield below the detection limit of our equipment, even when measurements on thin films are conducted with the aid of an integrating sphere. These limitations leave UV/vis spectroscopy as the best method for probing electronic interactions between the two compounds. However, the optical gap measured by UV/vis includes the exciton binding energy, and is therefore not equal to the HOMO-LUMO gap.

UV/Vis spectroscopy provides further evidence for mixing, rather than phase separation, of TIPS Pn and F8TIPS Pn in thin films. Spectra (**Figure 3.6**) indicate that the absorption edges of the mixed films (1.53 eV for the 1:1 blend) were slightly redshifted relative to the absorption edges of TIPS Pn (1.62 eV) and F8TIPS Pn (1.72 eV) films. Absorption below 1.6 eV for the mixed film could indicate photoexcitation of a charge transfer transition from TIPS Pn to F8TIPS Pn, based on the CV-determined HOMO and LUMO levels of TIPS Pn and F8TIPS Pn (**Table 3.3**). This is thought to result from through-space electronic interactions between adjacent TIPS Pn and F8TIPS Pn molecules that perturb the frontier molecular orbital energy levels. It is also important to note that the mixed film spectra did not fit any linear combination of TIPS Pn and F8TIPS Pn spectra, which provides further

evidence for mixing of the two molecules, rather than phase separation of domains, within the thin films.

Material	HOMO (CV)	LUMO (CV)	HOMO-LUMO gap	Optical gap (UV/vis)
TIPS	5.2 eV	3.1 eV	2.1 eV	1.6 eV
F8	5.5 eV	3.6 eV	1.9 eV	1.7 eV
alloy	5.2 eV (TIPS)	3.6 eV (F8)	1.6 eV	1.5 eV

Table 3.3. HOMO and LUMO levels from solution electrochemical measurements (cyclic voltammetry) vs. optical gap measured by thin film UV/vis.⁹⁹

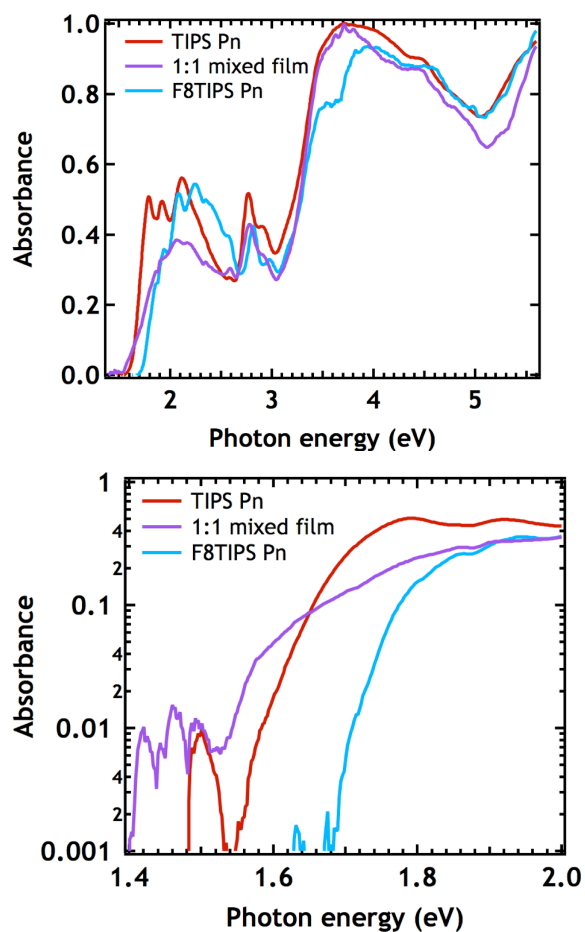


Figure 3.6. Ultraviolet-visible spectra of thin films shows that the absorption edge of the 1:1 mixed film is redshifted relative to TIPS Pn and F8TIPS Pn. Monochromator changeover at ~ 780 nm is responsible for some systematic noise (present in all spectra), and is likely responsible for the feature in the TIPS spectrum around 1.5 eV.

D. Conclusions

While the mixed crystalline phases of pentacene:perfluoropentacene blends are reportedly 1:1 stoichiometric mixtures, our data indicate that the structure of TIPS Pn:F8TIPS Pn mixed crystals changes continuously with increasing F8TIPS Pn fraction.¹²⁸
¹³⁰ Within experimental error, it does not appear that the presence of F8TIPS Pn induces significant disorder into thin films of TIPS Pn. We attribute this to the geometric similarity between the two compounds. Optical measurements of the mixed films corroborate the x-ray scattering analysis. The redshifted absorption edge of the mixed films relative to their constituents, and the fact that the mixed films' absorption spectra cannot be fit to any linear combination of the parent films, indicates that the two components are well mixed.

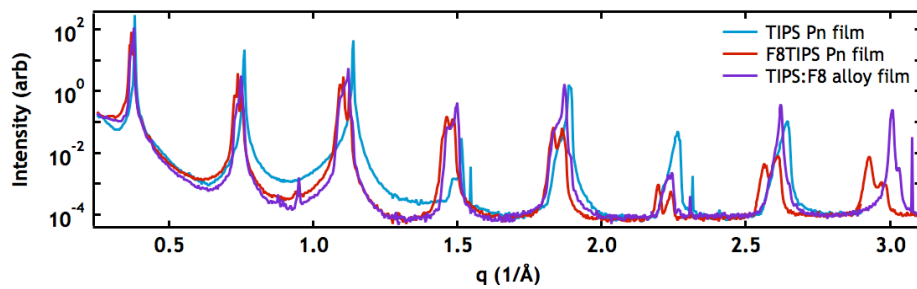


Figure 3.7. Specular x-ray scattering measurements, carried out on SSRL beamline 2-1, show multiple peaks for each film at higher order, indicating the presence of multiple polymorphs with (00l) spacings that vary only slightly.

CIF name	k03261	120207_4 _0m_jes	tipsf8cocry stal_0m_jes	120207_6 _0m_corr	120207_7 _0m_jes	jes12030 6_0m_jes	vial6f8_0 m_jes	k01029
%F8TIPS growth	1.000	0.910	0.500	0.500	0.250	0.500	0.091	0.000
%F8TIPS obs	1.000	0.946	0.694	0.678	0.487	0.444	0.085	0.000
a	7.718	7.714	7.648	7.649	7.571	7.568	7.534	7.565
b	15.545	15.544	7.728	7.723	7.751	7.761	7.707	7.750
c	16.785	16.896	16.930	16.925	16.876	16.853	16.772	16.835
alpha	102.247	102.263	89.417	89.456	89.481	89.530	89.463	89.150
beta	92.666	92.445	78.493	78.443	78.712	78.743	78.660	78.420
gamma	91.546	91.599	87.941	87.889	87.266	87.033	84.125	83.630
V	1975.060	1976.600	979.840	978.900	970.100	969.580	949.800	960.900
Z	2.000	2.000	1.000	1.000	1.000	1.000	1.000	1.000
R _{gt}	0.062	0.087	0.052	0.057	0.079	0.047	0.072	0.049
alkyl disorder	none	none	full	full	partial	partial	partial	partial
Volume/Z	987.53	988.3	979.840	978.900	970.100	969.580	949.800	960.900
density	1.317	1.303	1.252	1.250	1.212	1.204	1.140	1.104

Table 3.4. Summary of crystallographic data for all crystal structures used in this analysis.

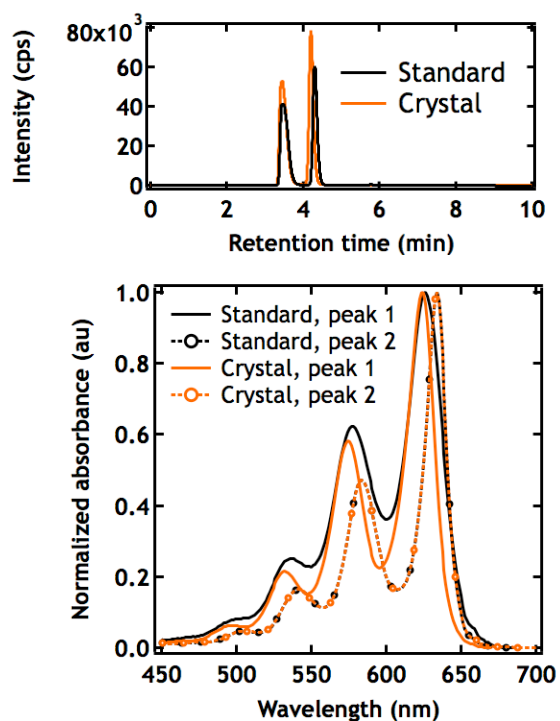


Figure 3.8. HPLC data showing retention times and UV-vis spectra corresponding to chromatographic peaks for a standard containing both F8TIPS and TIPS Pn, and a mixed crystal. HPLC analysis of 10 mixed crystals, grown from a 1:1 solution of F8TIPS Pn and TIPS Pn, gave an average composition of 60.4% ($\pm 6.4\%$) F8TIPS Pn.

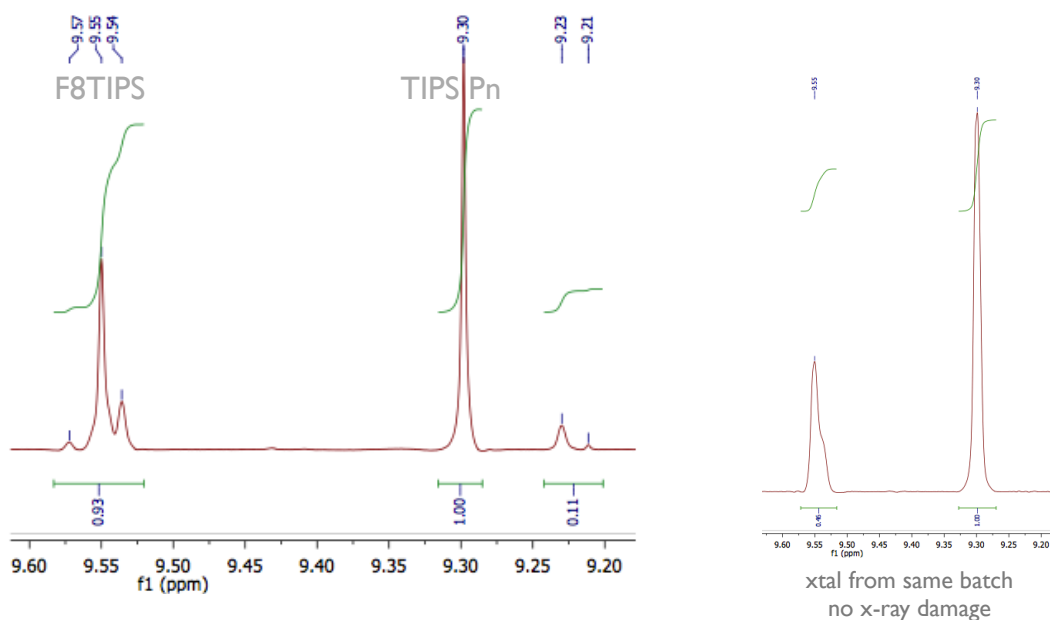


Figure 3.9. ¹H NMR spectra reveal that a single mixed crystal, for which crystallographic data refinement yielded a fractional composition of 43% F8TIPS Pn, contains 46% F8TIPS Pn. The authors note that additional peaks are present, and we attribute these to radiation damage, since the crystal was indexed before turning on the cryostat. An NMR spectrum of another mixed crystal, from the same batch, does not show these extra peaks. The chemical shifts displayed in these spectra correspond to protons attached to aromatic carbons in the acene core, but do not include protons attached to the terminal rings of the acene, as these are only present in TIPS Pn and not F8TIPS Pn.

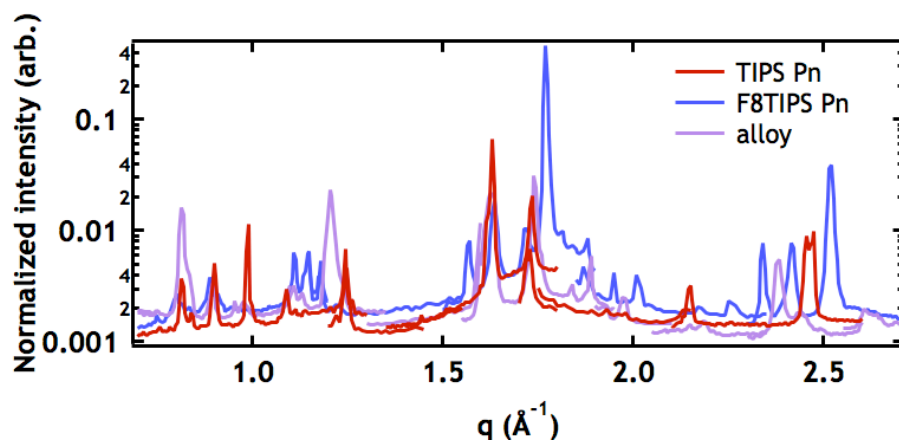


Figure 3.10. High resolution in-plane x-ray scattering, from SSRL beamline 7-2, shows significant differences in the high angle scattering peaks for the mixed film relative to TIPS Pn and F8TIPS Pn, further supporting our claim that the mixed film is well-blended rather than separate domains of TIPS Pn and F8TIPS Pn.

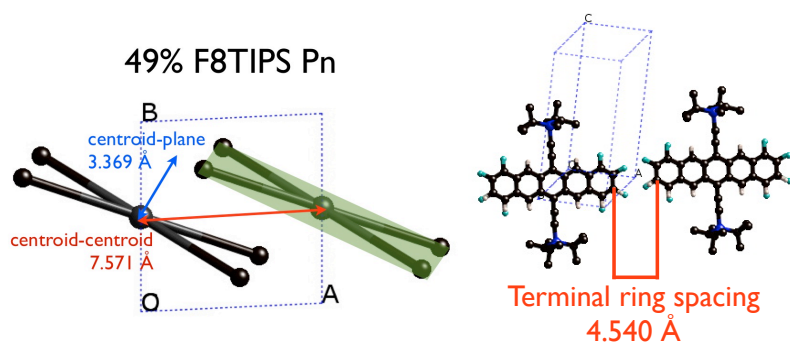


Figure 3.11. Example of packing schematics shown for one crystal structure, with appropriate distances labeled.

4. Amorphous Thin Films of Binary Isomer Mixtures

Jes Sherman, Chien-Yang Chiu, Ryan Fagenson, Guang Wu, Craig Hawker, Michael Chabinyc

A. Introduction

Producing amorphous organic solids, and preventing their crystallization, presents a challenge to research in organic electronics, pharmaceutical science and energetic materials.¹³⁴ Amorphous solids tend to crystallize, and small crystallites, which are thermodynamically disfavored because of their high relative surface areas, grow over time. This leads to a decline in materials performance for applications that require small particles or well-blended components capable of phase separation. This is of particular interest for OLEDs, which frequently employ an emissive guest in a host material—crystallization can lead to dark areas within a device.¹³⁵ Organic photovoltaics also suffer a decline in device performance over time as one or both components of the bulk heterojunction crystallize, leading to larger domains.¹³⁶ A common solution is to use materials which have relatively stable amorphous phases, i.e. molecular glasses.

Molecular structure has a strong influence on the formation of a glass. A common strategy to produce glassy organic materials is to increase steric bulk and conformational flexibility, thus preventing crystallization.^{137, 138} This has led to successful hole transport materials, such as spiro-OMeTAD.¹³⁹ These materials have been used in dye-sensitized solar cells.¹⁴⁰ Attempts have also been made to produce compounds with higher glass transition temperatures, to further extend operating temperature ranges for devices where deposition conditions lead to the glass.¹⁴¹ For example, exceptionally stable glasses can be formed by vapor deposition by controlling substrate temperature and deposition rate.¹⁴²

Here we explore a strategy to blend a stable glass-forming compound with a structurally similar additive, a geometric isomer, to produce an even more stable glass. Structurally similar molecular additives that inhibit crystallization or, in lower concentrations, alter crystal habit, are widely studied in the pharmaceutical industry.^{143, 144, 38} In the area of organic electronics, there are few reports of this approach. For example, two atropisomers of a hole-transporting indolo[3,2-*b*]carbazole were shown to form a stable glass with a high T_g (164° C).⁶³ Here, we use two isomers of MeBTP (**Figure 4.1**). Like a related compound, 9,9'-BF, MeBTP is twisted due to steric bulk around its strained double bond; this strain is relieved upon accepting an electron, which also produces an aromatic [4n+2] electron π -system.^{145, 146} We show that neat films of the *trans* isomer, (E)-MeBTP, slowly crystallize, producing spherulites and dendritic structures within thin films. While (E)-MeBTP is already capable of forming relatively stable glasses, blending (E)-MeBTP with (Z)-MeBTP suppresses crystallization even further.

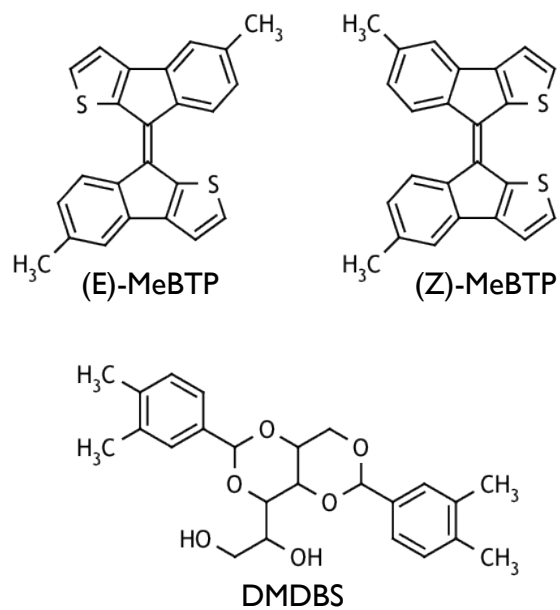


Figure 4.1. Chemical structures of (E)-MeBTP, its isomer (Z)-MeBTP, and the nucleation agent DMDBS.

B. Results and Discussion

Because (E)-MeBTP can be purified by fractionation, whereas (Z)-MeBTP can only be isolated in small quantities after exhaustive chromatography, this study focuses on (E)-MeBTP, the more available of the two compounds. Lack of availability of (Z)-MeBTP precluded study of the pure material beyond synthetic characterization, though we were able to obtain a crystal structure. (E)-MeBTP does not appear to isomerize in toluene solutions. Heating (E)-MeBTP in toluene solution at 200 °C overnight using a microwave reactor failed to produce the (Z) isomer. We also explored the use of photoinduced isomerization by irradiating with intense light at ambient temperature overnight, using a white light or a 380 nm LED source with no evidence of isomerization. The crystal structure of (E)-MeBTP is shown in **Figure 4.2**.

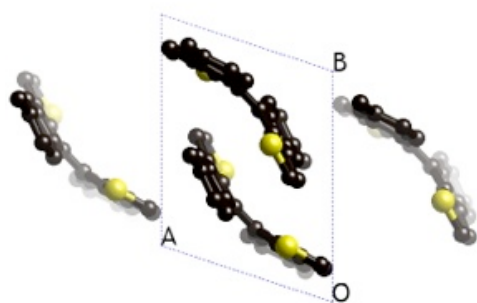
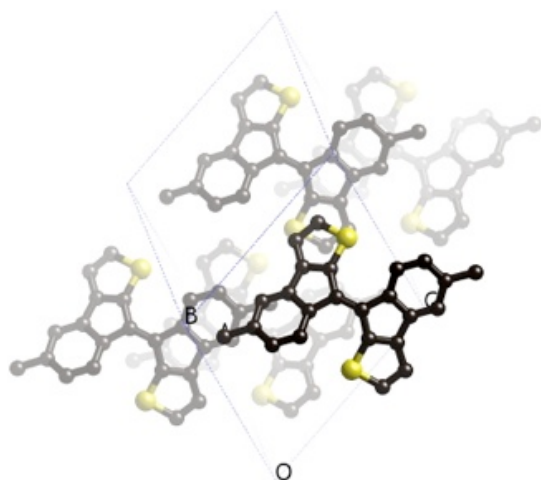


Figure 4.2. Crystal structure of (E)-MeBTP.

Thermal analysis is useful in determining the stability of glass-forming compounds, and in assessing which temperature ranges favor nucleation and growth. Materials that form stable glasses often do not reveal recrystallization from the melt by differential scanning calorimetry. This can be attributed to the timescale of these processes, and to the fact that nucleation does not always take place in the same temperature range as growth.¹⁴⁷ In the case of (E)-MeBTP, DSC—performed using a crystalline sample—showed melting only on the first scan, and reproducible glass transitions upon subsequent cooling and reheating to melt (**Figure 4.3**). The absence of crystallization or melting features after several hours of heating/cooling cycles between T_g and T_m indicates that (E)-MeBTP is a stable glass-forming compound. This is not surprising—one indicator of glass stability is the reduced T_g , defined as T_g/T_m , which is ~ 0.7 for (E)-MeBTP.¹⁴⁸ It is informative to compare the thermal behavior of (E)-MeBTP with a mixture of (E)- and (Z)-MeBTP isomers. A 3:2 mixture of (E)-MeBTP and (Z)-MeBTP also shows melting upon first heating, but also fails to show recrystallization from the melt or melting upon subsequent heating/cooling cycles. This failure to recrystallize, as well as the similarity of the glass transition temperatures between (E)-MeBTP and mixed (E)- and (Z)-MeBTP, might seem to indicate that (E)-MeBTP isomerizes upon melting, but we discount this possibility because no isomerization was observed when a toluene solution of (E)-MeBTP was heated at 200 °C overnight.

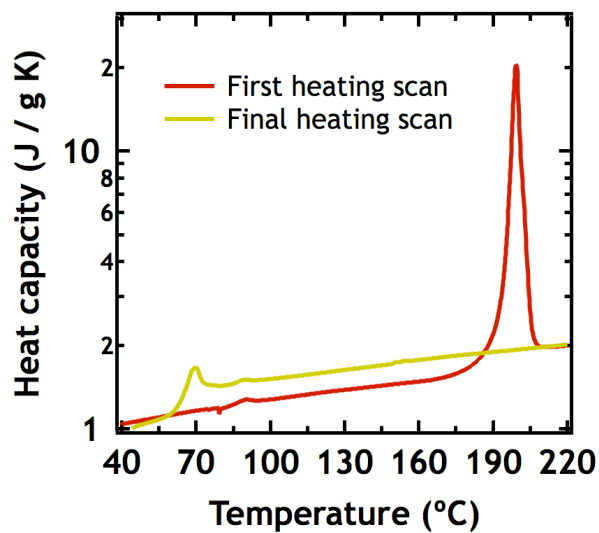


Figure 4.3. DSC shows melting upon first heating a sample of (E)-MeBTP. Despite several heating-cooling cycles in a temperature range thought to promote nucleation and growth, no melting was observed upon reheating to the melting point. This indicates that the material did not crystallize, but a reproducible glass transition at 70 °C is observed.

Optical microscopy also reveals that cooling (E)-MeBTP from the melt results in a glass that does not appear to crystallize. After melting (E)-MeBTP between two microscope cover slips, then cooling to ambient temperature, no crystallization was apparent by optical microscopy after several weeks. Heating the sample for several hours at 60 °C, a temperature slightly below the T_g which should favor rapid growth, also yielded no crystallization within three weeks of casting.¹⁴⁹ Because diffusion at the surface of molecular glasses is known to play a role in some crystal growth modes, we attempted to melt a spincoated film of (E)-MeBTP, but dewetting was observed at temperatures above 140 °C.^{150, 142} A film with an uncovered (E)-MeBTP surface was obtained by melting a sample between two cover slips, and then carefully removing the top cover slip. Optical microscopy revealed no crystallization in this sample, even after aging for three weeks at room temperature.

Solution processing of thin films is more practical than melt processing for organic electronic device applications, so we investigated the stability of spincoated amorphous MeBTP films. Within a few days of spincoating, spherulites (indicative of crystallization) were evident by optical microscopy (**Figure 4.5**) in films of (E)-MeBTP, but not in mixed (3:2) (E)- and (Z)-MeBTP films. After aging for several months, neat films of (E)-MeBTP were almost entirely covered by spherulite and dendrite growth, with only a small area that still appeared amorphous. By contrast, mixed films were almost completely still glassy, with only two small regions of surface crystal growth. As expected, AFM (**Figure 4.4**) shows that the remaining glassy region of the (E)-MeBTP film is smooth and similar in texture to the almost entirely glassy mixed film. By AFM, a spherulite on the (E)-MeBTP film is considerably rougher, but does not show features as tall as a fibrous surface crystal,

which reaches more than a micron above the surface. This is similar to previously reported data on crystals produced by surface-mediated diffusion.¹⁵¹

In an attempt to induce spherulite nucleation and subsequent growth in mixed isomer films, we employed the nucleation agent DMDBS. DMDBS has proven effective in inducing nucleation in TIPS-pentacene and semiconducting polymers when cast from solution.⁵¹ Adding a small amount (0.1% by weight) of DMDBS to (E)-MeBTP in solution before casting produced spherulites very quickly; annealing at 60 °C appeared to accelerate this process (**Figure 4.6**). However, the same treatment did not induce any spherulite formation in 3:2 mixed films, even after annealing.

Because optical microscopy can only easily reveal micron scale crystallites in the solution cast films, we also examined whether smaller scale crystallites were present using synchrotron source grazing incidence wide angle x-ray scattering (GIWAXS). GIWAXS of a thin (60 nm) film of (E)-MeBTP (**Figure 4.7**) shows scattering peaks that match well with data simulated using the bulk structure of the compound. Because a few peaks are present in the experimental data that do not appear in the simulation data, we believe an additional polymorph of (E)-MeBTP is present in the thin films similar to many organic materials. Mixed films containing (E)-and (Z)-MeBTP, unlike neat (E)-MeBTP films, exhibit only a broad amorphous “halo” in GIWAXS. This indicates a lack of long-range order in the mixed films, even after adding nucleation agents or aging for six months, as shown in the optical microscopy (**Figure 4.5** and **Figure 4.6**) and the GIWAXS (**Figure 4.7**). We note that fibrous surface growths, presumed to be crystals, are apparent after aging for five months in the mixed film by optical microscopy (**Figure 4.5**), but it is possible that the aggregates are not well ordered or that they were not sampled by the x-ray beam. The vast

majority of the mixed film remained glassy—we estimate that the fibrous growths covered approximately $50\text{ }\mu\text{m}^2$ of the 1.5 cm^2 film.

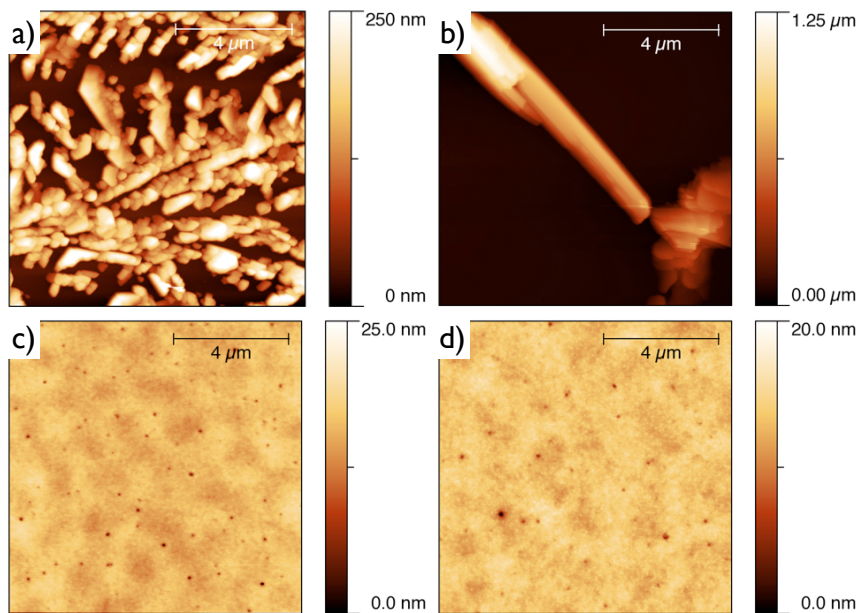


Figure 4.4. AFM images show that (a), a spherulite in a film of (E)-MeBTP does not exhibit features as tall as observed for (b), a surface crystal in a film of (E)-MeBTP. Glassy regions of (E)-MeBTP film (c) appear identical to the glassy mixed-isomer film (d).

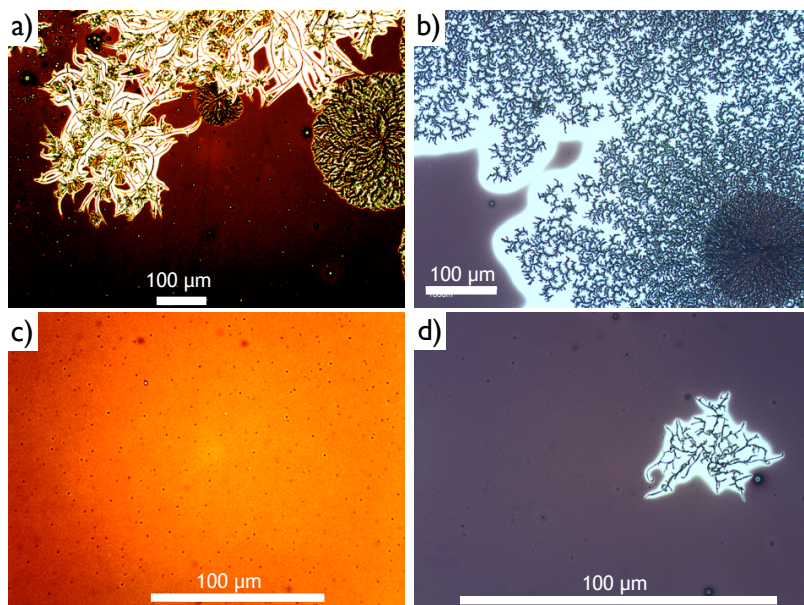


Figure 4.5. Optical microscope images show spherulite formation, indicating glass-to-crystal growth, in neat (E)-MeBTP films, but not in mixed films containing a 3:2 mixture of (E)- and (Z)-MeBTP. Mixed films do show surface crystal growth after 5 months. (a): (E)-MeBTP, 3 days after casting; (b): (E)-MeBTP, 5 months after casting; (c): mixed (E)- and (Z)-MeBTP, 3 days after casting; (d) mixed (E)- and (Z)-MeBTP, 5 months after casting.

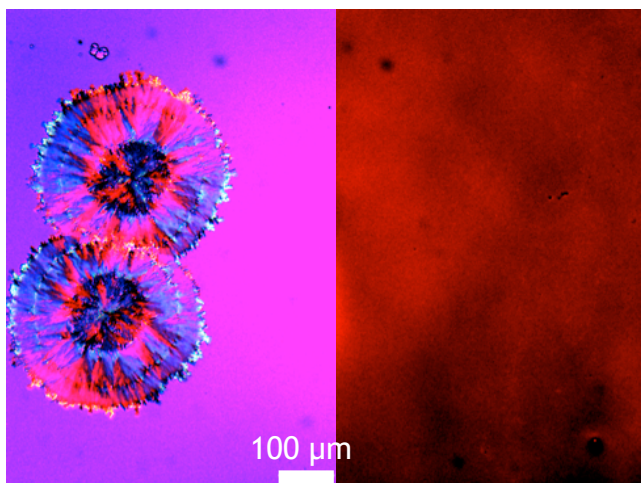


Figure 4.6. Optical microscope images show that adding nucleation agent DMDBS and annealing for 10 minutes at 60 °C is sufficient to induce spherulite formation in films of neat (E)-MeBTP (left), but not in mixed films containing a 3:2 ratio of (E)-MeBTP and (Z)-MeBTP (right).

Under near-equilibrium growth conditions, structurally similar crystallization inhibitors attach to kink sites, slowing step velocity for particular crystal faces.^{152, 144} This “step-pinning” changes the crystal habit.^{38, 153} The concentration of inhibitor affects the induction time for crystallization; additive incorporation can induce disorder and broaden reflections.¹⁵⁴ Crystallization in an amorphous thin film differs from near-equilibrium conditions in that the solvent quickly dries, and then molecules are not free to diffuse through the thin film, only at the surface.¹⁴² We expect that the amount of (Z)-MeBTP present should affect the solid-state ordering of (E)-MeBTP because, once partially incorporated, (Z)-MeBTP should not be free to desorb from the surface of the growing crystal.

Casting films containing different concentrations of (Z)-MeBTP reveals that over 20% (Z)-MeBTP content is needed to inhibit growth. The film containing 20% (Z)-MeBTP exhibited a longer induction time for crystallization—no detectable crystallization had occurred two days after casting, but by the fourth day, spherulites were evident. A series of photos, taken over the course of a day using a polarized optical microscope, was used to measure the fractional area of a thin film covered by spherulite growth (**Figure 4.8**). This clearly shows that films containing less (Z)-MeBTP crystallize faster. This data can be used in conjunction with the Avrami equation to determine the crystallization mechanism.¹⁵⁵ In this case, the Avrami exponent is 1. Since the growth of new spherulites was observed in the films over the course of the experiment, it is reasonable to conclude that nucleation events are distributed throughout the crystallization process. This leads us to conclude that (E)-MeBTP glasses undergo surface crystallization.

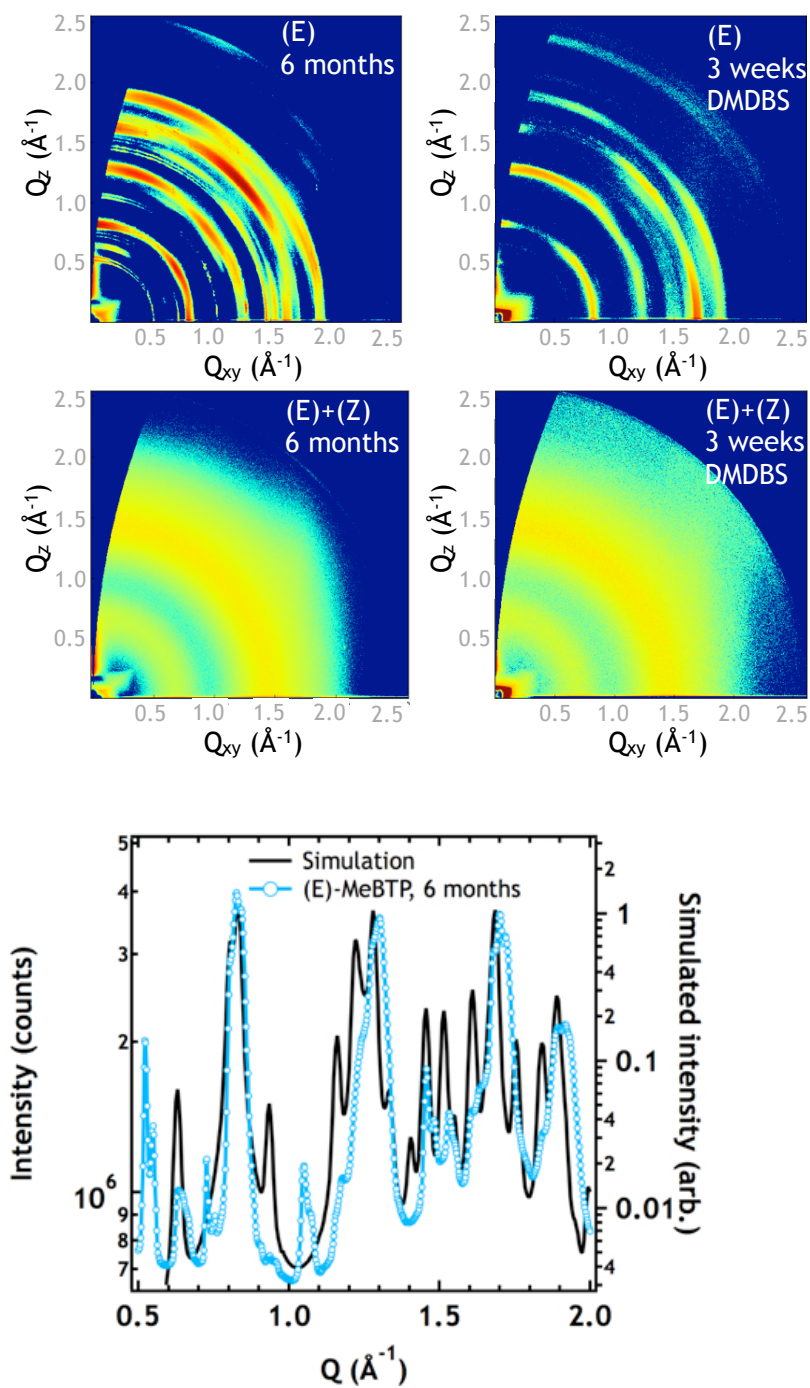


Figure 4.7. GIWAXS shows that (3:2) mixed films of (E)- and (Z)-MeBTP show only a broad amorphous halo, indicating a lack of crystalline order, even after aging for 6 months or with the addition of a nucleation agent. By contrast, neat films of (E)-MeBTP show intense scattering peaks. Comparing (E)-MeBTP scattering data with a diffraction pattern simulated using the (E)-MeBTP crystal structure indicates that the packing arrangement is the same in the thin film as in the bulk structure, and that the thin film probably contains an additional polymorph.

C. Conclusion

We have shown that (E)-MeBTP forms stable glasses from the melt, and its solution-cast thin films crystallize slowly. By DSC, melting of (E)-MeBTP is only ever observed on the first trace—we have not managed to successfully recrystallize the material from the melt in the DSC pan under any conditions, nor have we observed crystallization from a melted sample placed between two microscope cover slips. Solution-cast thin films of (E)-MeBTP exhibit glassy areas with pinholes, and over the course of a few days spherulites and rough surface crystals extending far above the substrate grow. These films adopt the packing shown in the bulk (E)-MeBTP structure, with some indication that another polymorph is also present.

Low concentrations of (Z)-MeBTP slow crystallization of its geometric isomer (E)-MeBTP, whereas high concentrations (40%) of (Z)-MeBTP appear to stop crystallization altogether. What is not known is the extent to which (Z)-MeBTP disrupts the solid-state ordering of (E)-MeBTP: at lower concentrations, when crystallization is still observed, do we still observe long-range order within the thin films, or do the higher-angle reflections broaden and weaken?

Finally, we believe thermopower measurements may be useful on the amorphous thin films. The low-lying LUMO level seems to indicate that n-doping may be a possibility for thin films containing mixed isomers; since the glassy matrix does not order strongly, the dopant may disperse better within the film.

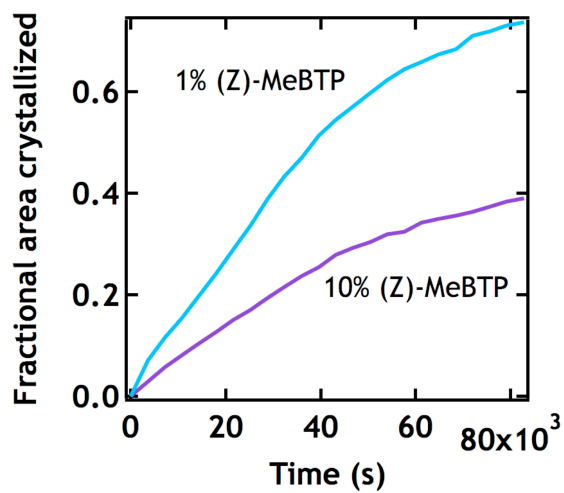


Figure 4.8. (E)-MeBTP films containing 1% (Z)-MeBTP crystallize more rapidly than (E)-MeBTP films containing 10% (Z)-MeBTP. Crystallization was measured over the course of a day using cross-polarizers with an optical microscope.

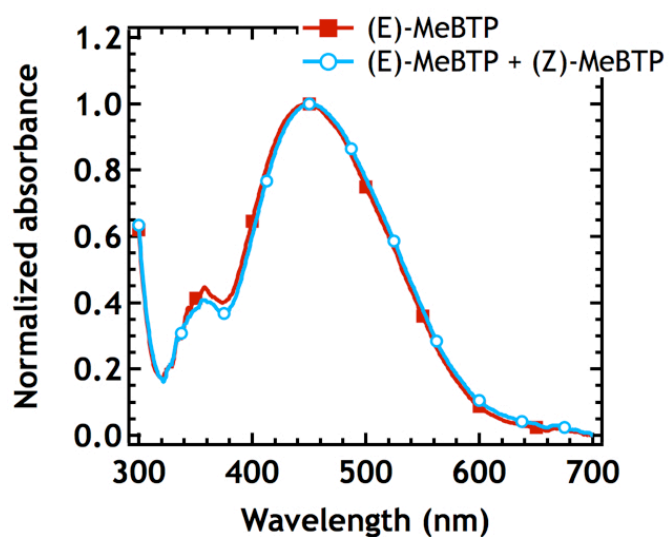


Figure 4.9. No significant difference is apparent in UV/vis spectra of thin films of neat (E)-MeBTP and mixed (E)-MeBTP and (Z)-MeBTP.

5. Interfacial Doping of Organic Semiconductors

Jes Sherman, John Anthony, Michael Chabinyc

A. Introduction

Electrical doping of organic semiconductors remains challenging despite the significant progress in the development of organic light emitting diodes, solar cells, and transistors. While bulk doping is required in many applications, interfacial doping can be used to gain information about electronic interactions between materials. For example, it has been shown that the interface between TTF and TCNQ single crystals has high electrical conductivity due to charge transfer between molecules.^{156, 157} Such high-conductivity interfaces may be useful in making thermoelectric devices, as seen in the case of bilayers containing pentacene and F4TCNQ.²²

We have studied the well-known organic semiconductor F TES ADT along with the dopant F4TCNQ (structures shown in **Figure 5.1**) to explore doping of a solution processable organic semiconductor. F TES ADT has been reported to form uniform thin films with high hole mobility (above $1 \text{ cm}^2/\text{Vs}$).^{158, 159} The HOMO level of F TES ADT has been measured at -5.2 eV by UPS, which should make doping by F4TCNQ (LUMO -5.2 eV) possible.¹⁶⁰ Even more intriguing, F TES ADT has been observed to undergo an enantiotropic phase transition slightly below room temperature providing a means to examine how such transitions are affected by interfacial charge transfer.¹⁶¹ The formation of well-defined interfaces can also enable study of the diffusion of F4TCNQ into F TES ADT under thermal treatment.

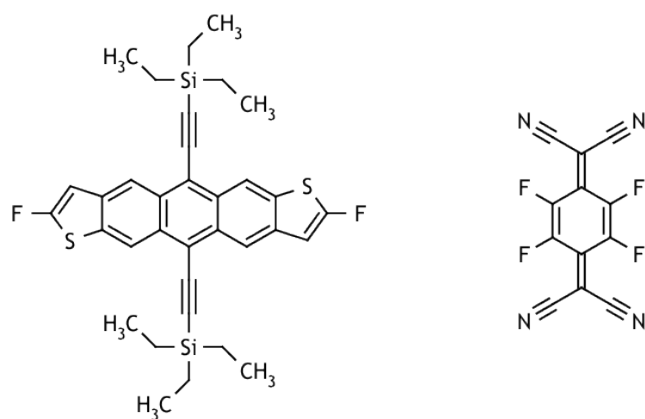


Figure 5.1. Chemical structures of F TES ADT and F4TCNQ.

B. Results

To study interfacial doping of F TES ADT, it is desirable to form films with relatively large crystalline domains. Blade-coating is useful in making highly uniform thin films that are crystalline over long ranges with preferred orientation.³¹ We decided to employ this coating method to produce crystalline thin films of F TES ADT. Typical blade coating was performed under ambient atmosphere using a razor blade, cleaned with toluene. 10 μ L of a 10 mg/mL toluene solution of F TES ADT were added to the substrate, then the blade, held at 30° with respect to substrate normal, was swept along the substrate at 0.3 mm/s. F TES ADT is highly soluble in many solvents, so solution processing to add a layer of F4TCNQ is counterindicated because of the high probability of dissolving, or at least disturbing, the underlying F TES ADT film. Instead, we took advantage of the high vapor pressure of F4TCNQ and added the dopant layer via sublimation in these initial experiments (**Figure 5.2**). Typical sublimation of F4TCNQ took five minutes at a source temperature of approximately 200 °C. In future studies, thin films of F4TCNQ can be deposited by high vacuum thermal evaporation using a quartz crystal microbalance thickness monitor to keep track of coverage during the deposition process.

Blade-coated F TES ADT films contain crystalline ribbons of F TES ADT with bare substrate (SiO_x with HMDS surface treatment) between them. The optical micrograph of a blade-coated film of F TES ADT is shown in **Figure 5.3**. These blade-coated F TES ADT films have crystalline ribbons with step edges of approximately 2 nm measured by atomic force microscopy (AFM); this corresponds well with the (001) d-spacing of 16.6 Å in the F TES ADT bulk crystal structure (**Figure 5.4**). The ribbons are approximately 30 nm thick, as measured from substrate to surface and are about 5-6 μ m wide and are spaced about 2 μ m apart on the substrate.

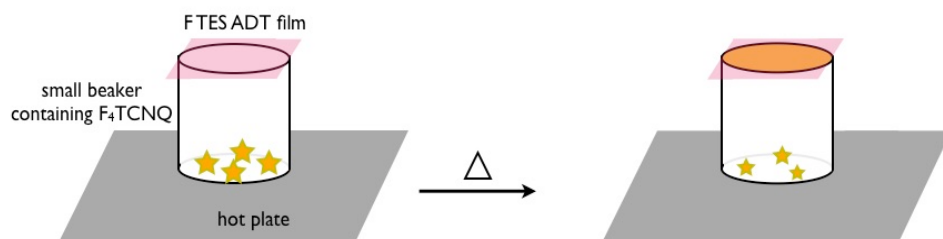


Figure 5.2. Schematic showing apparatus for sublimation of F₄TCNQ.

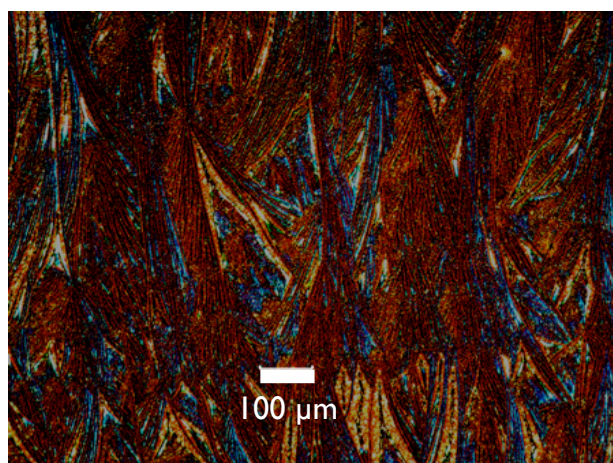
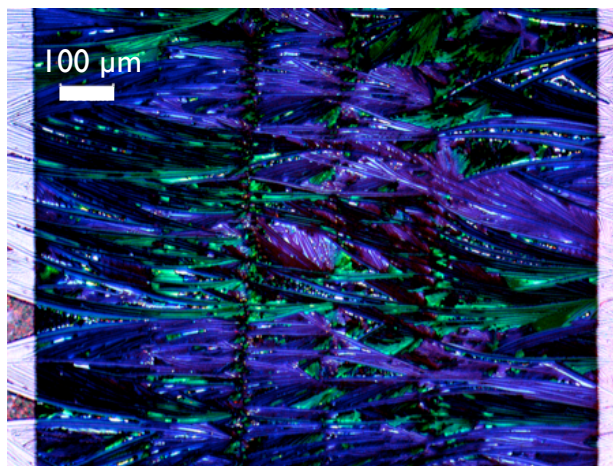


Figure 5.3. Optical micrographs of blade-coated F TES ADT films without (top) and with (bottom) sublimed F4TCNQ layer.

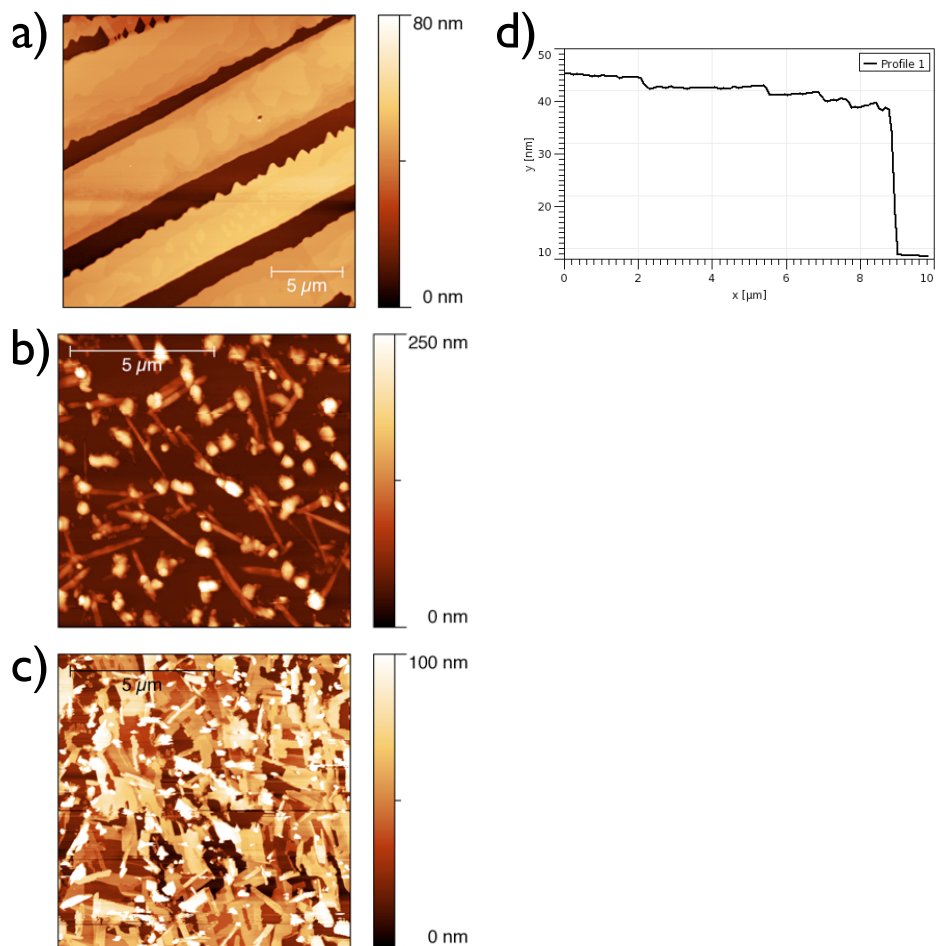


Figure 5.4. AFM images show very different topography for (a) 20 by 20 μm image, blade-coated F TES ADT film, (b) 10 by 10 μm image, sublimed F4TCNQ film, and (c) 10 by 10 μm image, sublimed F4TCNQ film on an underlying blade-coated F TES ADT film. Height profile (d) of the blade-coated F TES ADT film in (a) shows clear step edges, approximately 2 nm high, on a crystalline ribbon of F TES ADT that is approximately 30 nm thick. Ribbons of F TES ADT are approximately 5-6 μm wide, and are approximately 2 μm apart with what appears to be bare substrate between them.

F4TCNQ appears to adopt a different morphology when sublimed onto a film of F TES ADT as opposed to a bare substrate. F4TCNQ films sublimed onto bare SiO_x are very rough, exhibiting distinct “islands”. These appear either as elongated needles, with long axis parallel to the substrate plane, or as rough tall features, reaching up to 250 μm high. The substrate is likely covered in a thin layer of F4TCNQ as well, but it is difficult to discern from AFM images. When F4TCNQ is sublimed onto a film of F TES ADT, however, the AFM (**Figure 5.4**) reveals a very different morphology, comprised of overlapping grains with sharp edges. The F4TCNQ films imaged in **Figure 5.4** were sublimed simultaneously in the same deposition chamber. The underlying F TES ADT layer does not appear to be disturbed, as seen in **Figure 5.3**, but we speculate that it is likely that the F4TCNQ is coating the bare substrate between the F TES ADT ribbons.

Synchrotron x-ray scattering confirms that the ribbon-shaped domains in the F TES ADT film are crystalline, with molecular packing similar to the bulk structure. The GIWAXS shown in **Figure 5.5** reveals slight differences between the overlay of simulated data based on the HT bulk crystal structure of F TES ADT and the thin film scattering.¹⁶¹ This is not surprising, given that polymorphism is common in organic compounds, and multiple thin film polymorphs may be observed—often, the packing is very similar from polymorph to polymorph.^{35, 34} Very subtle changes to unit cell lengths or angles of the triclinic F TES ADT unit cell could produce the observed thin film diffraction pattern without significant perturbation of the molecular packing. As previously observed, the F TES ADT films are oriented with (001) planes parallel to the substrate; the (001) d-spacing, as previously noted, corresponds well to the step height observed in the AFM.

F4TCNQ does not adopt a preferred orientation when sublimed onto a bare SiO_x substrate, but appears textured when sublimed onto F TES ADT. The GIWAXS in **Figure**

5.5 shows powder-like rings for F4TCNQ sublimed onto a bare substrate, as well as some discrete reflections. The reflections that correspond well to the powder diffraction observed for F4TCNQ seem to indicate some oriented population of F4TCNQ, perhaps corresponding to the elongated needles seen in **Figure 5.4**. The diffraction rings are much less apparent when F4TCNQ is sublimed onto F TES ADT, but are still faintly present. We note that the necessary exposure time to observe scattering for the F4TCNQ film is much longer than that required for the F4TCNQ:F TES ADT film; this suggests that the un-oriented F4TCNQ film scatters more weakly than the crystalline material in the rest of the film, perhaps because it is less ordered. New reflections, not associated with the bulk structure of F TES ADT, appear in the diffraction pattern; the most readily apparent of these in **Figure 5.5** is the family of reflections appearing at $q_{xy} \sim 0.58 \text{ \AA}^{-1}$. We speculate that these correspond to a different polymorph of F4TCNQ, which is templated by the F TES ADT surface, but we have not yet indexed the pattern or attempted to solve the structure. The speculation is more plausible in light of the AFM data in **Figure 5.4** that show the morphology difference of F4TCNQ films sublimed onto the different surfaces. The fact that the F TES ADT reflections do not change upon F4TCNQ sublimation appears to indicate that the underlying film is not significantly disturbed—in other words, the F4TCNQ dopant does not fully diffuse into the F TES ADT film.

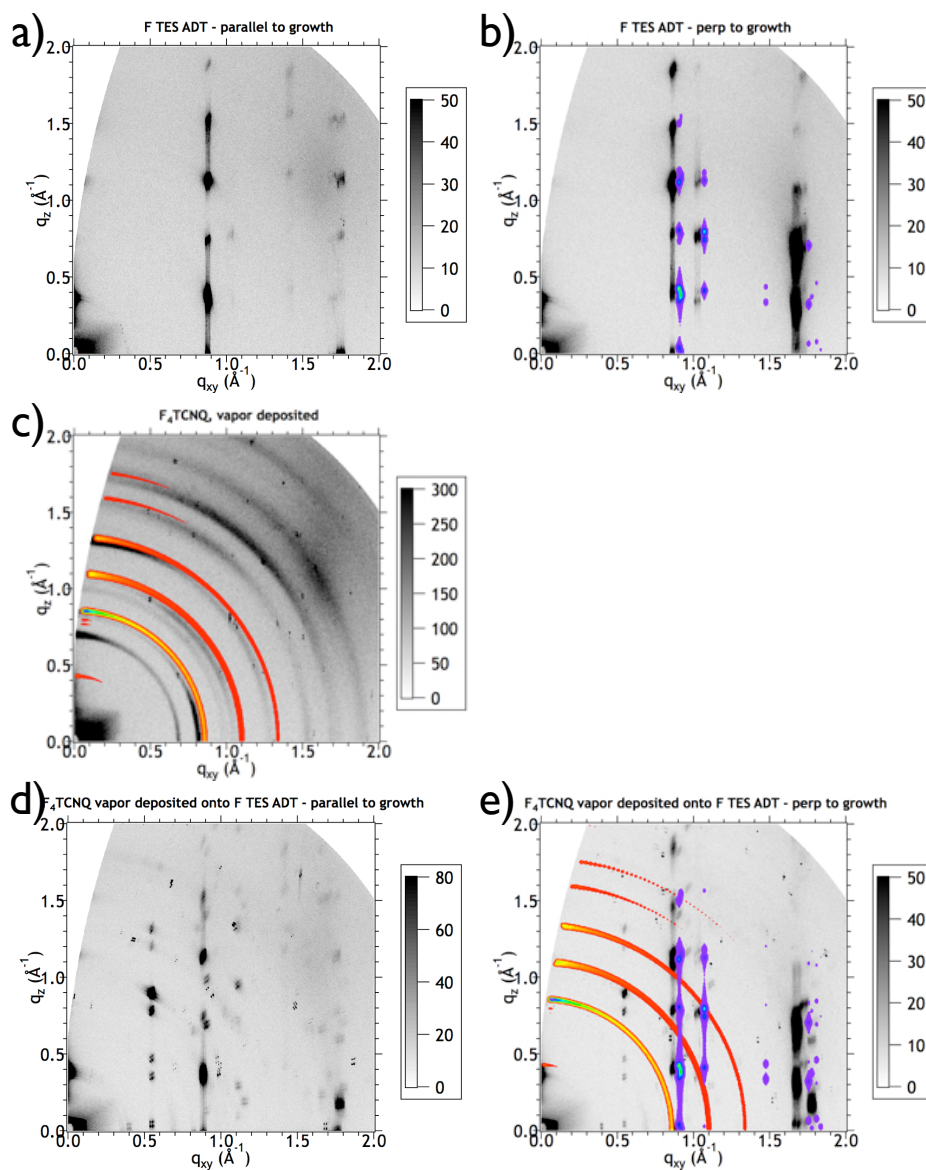


Figure 5.5. GIWAXS of thin films. SimDiffraction overlays are of bulk unit cells of F TES ADT (purple, simulated with (001) orientation) and F4TCNQ (red, shown with no preferred orientation).

Conductivities of doped and undoped F TES ADT films were calculated from two-point probe measurements. Gold contacts were evaporated onto the F TES ADT films perpendicular to the blade-coating direction (the growth direction of the film). Current-voltage characteristics of the films are shown in **Figure 5.6**. Undoped F TES ADT films exhibited conductivity less than $6.7 \cdot 10^{-7}$ S/cm, but after doping, the conductivity measured as high as 1.8 S/cm. These calculations assume that the entire F TES ADT film is conductive, but it is likely only the interface that is conductive because the F4TCNQ does not diffuse into the entire F TES ADT film. We also assume that the F4TCNQ film is not conductive. These conductivities are higher than observed for pentacene films doped by F4TCNQ.²²

Future work will examine the thermopower in the films to determine if hole or electron conduction is dominant. The charge transfer process should produce holes in the F TES ADT and electrons in F4TCNQ. In a semiconductor, the thermopower depends on both holes and electrons and is weighted by their contribution to the electrical conductivity. Here the F4TCNQ coats the top and sides of the F TES ADT ribbon, and can potentially contribute to the electrical conductivity.

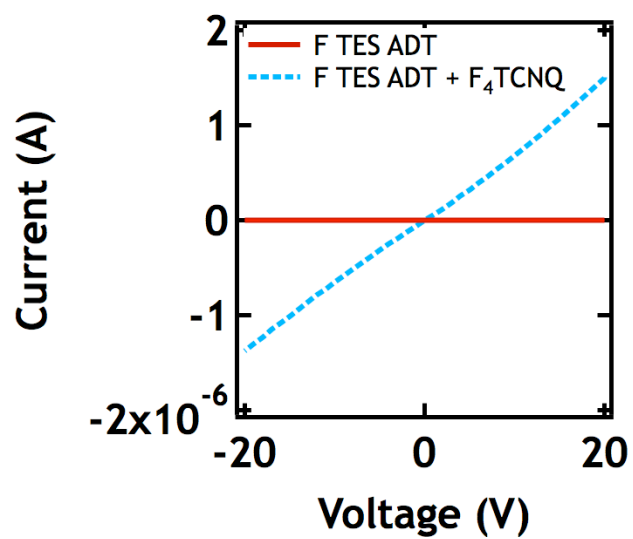


Figure 5.6. Conductivity of F TES ADT films with and without F4TCNQ.

6. Ambipolar Transistors from Glassy Polymer

Jes B. Sherman, Chien-Yang Chiu, Craig Hawker, Michael Chabinyo

Ambipolar charge transport is desirable in organic electronics—materials that transport both holes and electrons well can open possibilities for new electronic applications for organic materials.²⁴ We examined an ambipolar polymer, pBTPDPP, containing a BTP subunit and a DPP subunit in the monomer. The chemical structure of this polymer is shown in **Figure 6.1**. The DPP subunit has been used in ambipolar polymers, whereas the BTP monomer was only recently investigated in glassy thin films (see **Chapter 4**).¹⁶² The BTP subunit, containing a strained double bond, should twist the polymer backbone.

pBTPDPP has interesting electronic properties. The HOMO level of pBTPDPP, as measured by cyclic voltammetry, is -5.2 eV, and the LUMO level is -3.5 eV.

The solid-state ordering of the pBTPDPP polymer was examined by grazing incidence wide angle x-ray scattering (GIWAXS) (**Figure 6.2**). The GIWAXS image is relatively glassy, as is expected from the presence of the BTP subunit, but a few broad peaks are apparent with corresponding d-spacings of 3.9 Å, 4.8 Å, and 10.0 Å.

To study the electrical characteristics of pBTPDPP, we made thin film transistors. Thin films of pBTPDPP were made by spin coating from solution; 6 mg pBTPDPP were added to 600 μ L chlorobenzene, and allowed to dissolve overnight while stirring on a hot plate at 80 °C. Transistor substrates (200 nm of SiO_x with lithographically patterned gold contacts) were subjected to solvent cleaning, followed by 3 minutes of air plasma.

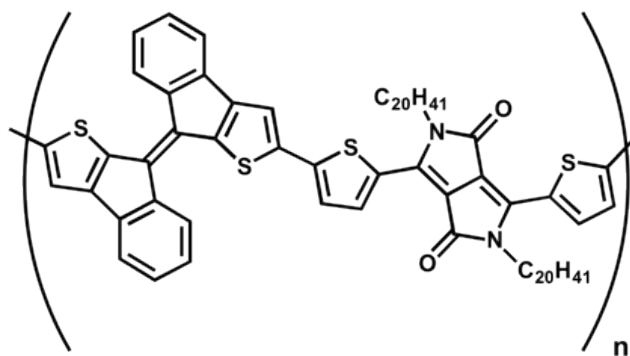


Figure 6.1. Chemical structure of pBTPDPP polymer.

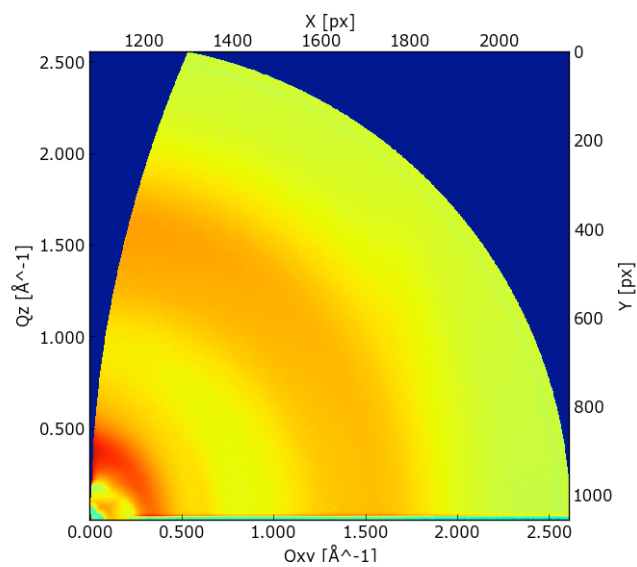


Figure 6.2. GIWAXS of pBTPDPP shows no strongly preferred orientation.

Substrates were then transferred to a glovebox, where neat HMDS was spincoated through a glass pipette at 1000 RPM for 60 s. Following this treatment, polymer solutions were spincoated through a 0.45 μm syringe filter at 1200 RPM for 60 s, with an additional drying step at 2000 RPM for 10 s. Films were then transferred to a vacuum probe station for transistor measurements.

Output and transfer characteristics of pBTPDPP show relatively balanced hole and electron transport. **Figure 6.3** shows the transfer and output characteristics of a pBTPDPP transistor with W/L of 2, operating under negative gate bias. The hole mobility of this device was found to be $4.08 \cdot 10^{-3} \text{ cm}^2/\text{Vs}$. **Figure 6.4** shows the transfer and output characteristics of the same transistor, operating under positive gate bias, with an electron mobility of $2.75 \cdot 10^{-3} \text{ cm}^2/\text{Vs}$. These values are lower than many high performance ambipolar materials, but are both surprisingly high for a polymer with glassy ordering.

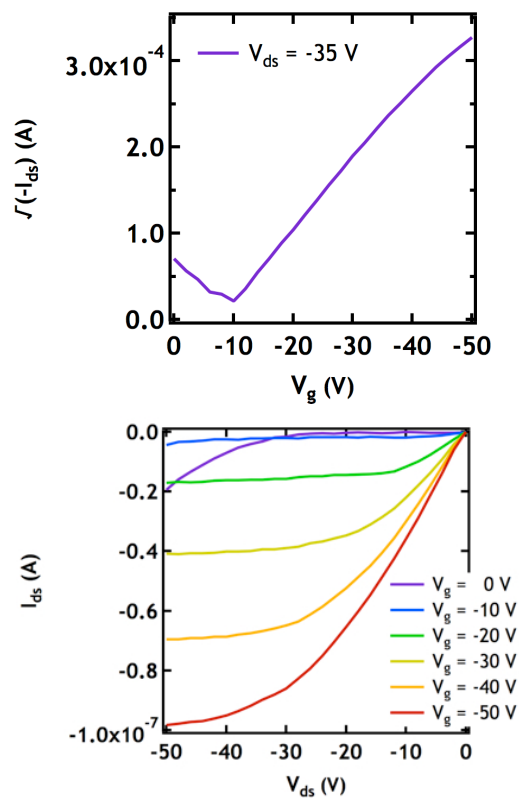


Figure 6.3. Hole transport in a pBTPDPP transistor.

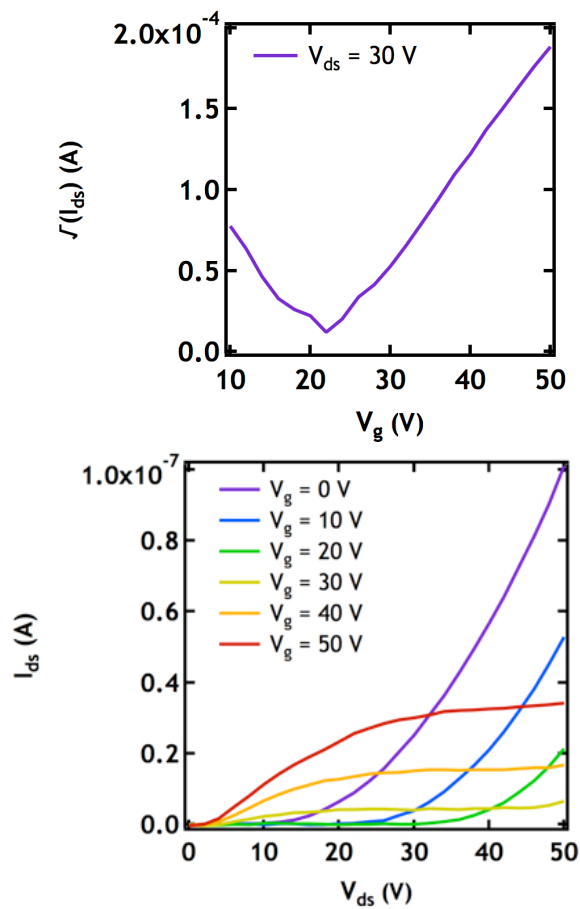


Figure 6.4. Electron transport in a pBTPDPP transistor.

Acknowledgments

JBS was supported by a DOE Graduate Fellowship and by the Center for Energy Efficient Materials, an Energy Frontier Research Center funded by the U.S. Department of Energy, Office of Science, Office of Basic Energy Sciences under Award Number DE-SC0001009. CK, SC, and TQN were partially supported by the NSF SOLAR program (DMR 1035480). JEA and BP were supported by the NSF SOLAR program (DMR 1035257). The MRL Shared Experimental Facilities are supported by the MRSEC Program of the NSF under Award No. DMR 1121053; a member of the NSF-funded Materials Research Facilities Network (www.mrfn.org). Portions of this research were carried out at the Stanford Synchrotron Radiation Lightsource, a directorate of SLAC National Accelerator Laboratory and an Office of Science User Facility operated for the U.S. Department of Energy Office of Science by Stanford University. We gratefully thank Dag Brieby for the SimDiffraction software and Thomas Gelbrich for the XPac software.

References

- (1) Smith, M. B.; March, J. *March's Advanced Organic Chemistry: Reactions, Mechanisms, and Structure*; 6 edition.; Wiley-Interscience: Hoboken, N.J, 2007.
- (2) Hoffmann, R. *Acc. Chem. Res.* **1971**, *4*, 1–9.
- (3) Carroll, F. A. *Perspectives on structure and mechanism in organic chemistry*; Brooks/Cole Pub. Co: Pacific Grove, 1997.
- (4) Geoghegan, M.; Hadziioannou, G. *Polymer Electronics*; Oxford University Press, 2013.
- (5) Pino, R.; Scuseria, G. E. *J. Chem. Phys.* **2004**, *121*, 8113–8119.
- (6) Castiglioni, C.; Zerbi, G.; Gussoni, M. *Solid State Commun.* **1985**, *56*, 863–866.
- (7) So, F. *Organic Electronics: Materials, Processing, Devices and Applications*; CRC Press, 2009.
- (8) Goetz, K. P.; Li, Z.; Ward, J. W.; Bougher, C.; Rivnay, J.; Smith, J.; Conrad, B. R.; Parkin, S. R.; Anthopoulos, T. D.; Salleo, A.; Anthony, J. E.; Jurchescu, O. D. *Adv. Mater.*
- (9) Wang, C.; Dong, H.; Hu, W.; Liu, Y.; Zhu, D. *Chem. Rev.* **2012**, *112*, 2208–2267.
- (10) Hirsch, A.; Brettreich, M. *Fullerenes: Chemistry and Reactions*; John Wiley & Sons, 2006.
- (11) Ong, B. S.; Wu, Y.; Li, Y.; Liu, P.; Pan, H. *Chem. – Eur. J.* **2008**, *14*, 4766–4778.
- (12) Guo, X.; Baumgarten, M.; Müllen, K. *Prog. Polym. Sci.* **2013**, *38*, 1832–1908.
- (13) Sun, Y.; Welch, G. C.; Leong, W. L.; Takacs, C. J.; Bazan, G. C.; Heeger, A. J. *Nat. Mater.* **2012**, *11*, 44–48.
- (14) Prashad, M.; Sutton, P.; Wu, R.; Hu, B.; Vivel, J.; Carosi, J.; Kapa, P.; Liang, J. *Org. Process Res. Dev.* **2010**, *14*, 878–882.
- (15) Anthony, J. E.; Eaton, D. L.; Parkin, S. R. *Org. Lett.* **2002**, *4*, 15–18.
- (16) Günes, S.; Neugebauer, H.; Sariciftci, N. S. *Chem. Rev.* **2007**, *107*, 1324–1338.
- (17) Armin, A.; Kassal, I.; Shaw, P. E.; Hambsch, M.; Stolterfoht, M.; Lyons, D. M.; Li, J.; Shi, Z.; Burn, P. L.; Meredith, P. *J. Am. Chem. Soc.* **2014**, *136*, 11465–11472.
- (18) Xue, L.; Li, Y.; Dong, F.; Tian, W. *Nanotechnology* **2010**, *21*, 155201.
- (19) Yu, C.-Y.; Chen, C.-P.; Chan, S.-H.; Hwang, G.-W.; Ting, C. *Chem. Mater.* **2009**, *21*, 3262–3269.
- (20) Yan, D.; Evans, D. G. *Mater. Horiz.* **2013**.
- (21) Jr, P. A.; Montes, V. A.; Takizawa, S. *Appl. Phys. Lett.* **2008**, *93*, 163302.
- (22) Harada, K.; Sumino, M.; Adachi, C.; Tanaka, S.; Miyazaki, K. *Appl. Phys. Lett.* **2010**, *96*, 253304.
- (23) Yan, L.; Shao, M.; Wang, H.; Dudis, D.; Urbas, A.; Hu, B. *Adv. Mater.*
- (24) Zaumseil, J.; Sirringhaus, H. *Chem. Rev.* **2007**, *107*, 1296–1323.
- (25) Tang, M. L.; Bao, Z. *Chem. Mater.* **2011**, *23*, 446–455.
- (26) Laudise, R. A.; Kloc, C.; Simpkins, P. G.; Siegrist, T. *J. Cryst. Growth* **1998**, *187*, 449–454.
- (27) Chapman, B.; Checco, A.; Pindak, R.; Siegrist, T.; Kloc, C. *J. Cryst. Growth* **2006**, *290*, 479–484.
- (28) Rivnay, J.; Jimison, L. H.; Northrup, J. E.; Toney, M. F.; Noriega, R.; Lu, S.; Marks, T. J.; Facchetti, A.; Salleo, A. *Nat. Mater.* **2009**, *8*, 952–958.
- (29) Guinier, A. *X-ray Diffraction in Crystals, Imperfect Crystals, and Amorphous Bodies*; Courier Dover Publications, 1994.

- (30) Rivnay, J.; Noriega, R.; Kline, R. J.; Salleo, A.; Toney, M. F. *Phys. Rev. B* **2011**, *84*.
- (31) Diao, Y.; Tee, B. C.-K.; Giri, G.; Xu, J.; Kim, D. H.; Becerril, H. A.; Stoltenberg, R. M.; Lee, T. H.; Xue, G.; Mannsfeld, S. C. B.; Bao, Z. *Nat. Mater.* **2013**, *12*, 665–671.
- (32) Liman, C. D.; Choi, S.; Breiby, D. W.; Cochran, J. E.; Toney, M. F.; Kramer, E. J.; Chabinyc, M. L. *J. Phys. Chem. B* **2013**, *117*, 14557–14567.
- (33) Breiby, D. W.; Bunk, O.; Andreasen, J. W.; Lemke, H. T.; Nielsen, M. M. *J. Appl. Crystallogr.* **2008**, *41*, 262–271.
- (34) Diao, Y.; Lenn, K. M.; Lee, W.; Blood-Forsythe, M. A.; Xu, J.; Mao, Y.; Kim, Y.; Reinspach, J. A.; Park, S.; Aspuru-Guzik, A.; Xue, G.; Clancy, P.; Bao, Z.; Mannsfeld, S. C. B. *J. Am. Chem. Soc.* **2014**, 141021110957003.
- (35) Mannsfeld, S. C. B.; Tang, M. L.; Bao, Z. *Adv. Mater.* **2011**, *23*, 127–131.
- (36) Wedl, B.; Resel, R.; Leising, G.; Kunert, B.; Salzmann, I.; Oehzelt, M.; Koch, N.; Vollmer, A.; Duhm, S.; Werzer, O.; Gbabode, G.; Sferrazza, M.; Geerts, Y. *Rsc Adv.* **2012**, *2*, 4404–4414.
- (37) Kahr, B.; Gurney, R. W. *Chem. Rev.* **2001**, *101*, 893–952.
- (38) Kuvadia, Z. B.; Doherty, M. F. *Cryst. Growth Des.* **2013**, *13*, 1412–1428.
- (39) Thorat, A. A.; Dalvi, S. V. *CrystEngComm* **2014**, *16*, 11102–11114.
- (40) Nagy, Z. K.; Braatz, R. D. *Annu. Rev. Chem. Biomol. Eng.* **2012**, *3*, 55–75.
- (41) Dunitz, J. D.; Bernstein, J. *Acc. Chem. Res.* **1995**, *28*, 193–200.
- (42) Chemburkar, S. R.; Bauer, J.; Deming, K.; Spiwek, H.; Patel, K.; Morris, J.; Henry, R.; Spanton, S.; Dziki, W.; Porter, W.; Quick, J.; Bauer, P.; Donaubauer, J.; Narayanan, B. A.; Soldani, M.; Riley, D.; McFarland, K. *Org. Process Res. Dev.* **2000**, *4*, 413–417.
- (43) Bolton, O.; Simke, L. R.; Pagoria, P. F.; Matzger, A. J. *Cryst. Growth Des.* **2012**, *12*, 4311–4314.
- (44) Landenberger, K. B.; Matzger, A. J. *Cryst. Growth Des.* **2010**, *10*, 5341–5347.
- (45) Yang, Z.; Li, H.; Zhou, X.; Zhang, C.; Huang, H.; Li, J.; Nie, F. *Cryst. Growth Des.* **2012**, *12*, 5155–5158.
- (46) Hogge, W. C. *Effect of HNS on physical properties of TNT explosives: surveillance evaluation*; NWSY-TR-79-1; Naval Weapons Station, 1979.
- (47) Roncali, J. *Acc. Chem. Res.* **2009**, 090706165338012.
- (48) Salzmann, I.; Duhm, S.; Heimel, G.; Rabe, J. P.; Koch, N.; Oehzelt, M.; Sakamoto, Y.; Suzuki, T. *Langmuir* **2008**, *24*, 7294–7298.
- (49) Jurchescu, O. D.; Popinciuc, M.; van Wees, B. J.; Palstra, T. T. M. *Adv. Mater.* **2007**, *19*, 688–692.
- (50) Lee, S. S.; Kim, C. S.; Gomez, E. D.; Purushothaman, B.; Toney, M. F.; Wang, C.; Hexemer, A.; Anthony, J. E.; Loo, Y.-L. *Adv. Mater.* **2009**, *21*, 3605–3609.
- (51) Treat, N. D.; Nekuda Malik, J. A.; Reid, O.; Yu, L.; Shuttle, C. G.; Rumbles, G.; Hawker, C. J.; Chabinyc, M. L.; Smith, P.; Stingelin, N. *Nat. Mater.* **2013**, *12*, 628–633.
- (52) Probst, K. H.; Karl, N. *Phys. Status Solidi A* **1975**, *27*, 499–508.
- (53) Luria, J. L.; Schwarz, K. A.; Jaquith, M. J.; Hennig, R. G.; Marohn, J. A. *Adv. Mater.* **2010**, n/a – n/a.
- (54) Coropceanu, V.; Cornil, J.; da Silva Filho, D. A.; Olivier, Y.; Silbey, R.; Brédas, J.-L. *Chem. Rev.* **2007**, *107*, 926–952.
- (55) Gomar-Nadal, E.; Conrad, B. R.; Cullen, W. G.; Williams, E. D. *J. Phys. Chem. C* **2008**, *112*, 5646–5650.

- (56) Day, J.; Platt, A. D.; Ostroverkhova, O.; Subramanian, S.; Anthony, J. E. *Appl. Phys. Lett.* **2009**, *94*, 013306.
- (57) Mulliken, R. S.; Person, W. B. *Annu. Rev. Phys. Chem.* **1962**, *13*, 107–126.
- (58) Wudl, F.; Southwick, E. W. *J. Chem. Soc. Chem. Commun.* **1974**, 254–255.
- (59) Ferraris, J.; Cowan, D. O.; Walatka, V.; Perlstein, J. H. *J. Am. Chem. Soc.* **1973**, *95*, 948–949.
- (60) Cochran, J. E.; Junk, M. J. N.; Glaudell, A. M.; Miller, P. L.; Cowart, J. S.; Toney, M. F.; Hawker, C. J.; Chmelka, B. F.; Chabiny, M. L. *Macromolecules* **2014**, *47*, 6836–6846.
- (61) Guilbert, A. A. Y.; Reynolds, L. X.; Bruno, A.; MacLachlan, A.; King, S. P.; Faist, M. A.; Pires, E.; Macdonald, J. E.; Stingelin, N.; Haque, S. A.; Nelson, J. *ACS Nano* **2012**, *6*, 3868–3875.
- (62) Molaire, M. F. Monomeric glass mixtures incorporating tetracarbonylbisimide group. US7776500 B2, August 17, 2010.
- (63) Hu, N.-X.; Xie, S.; Popovic, Z.; Ong, B.; Hor, A.-M.; Wang, S. *J. Am. Chem. Soc.* **1999**, *121*, 5097–5098.
- (64) Engler, E. M.; Scott, B. A.; Etemad, S.; Penney, T.; Patel, V. V. *J. Am. Chem. Soc.* **1977**, *99*, 5909–5916.
- (65) Ponzini, F.; Zagha, R.; Hardcastle, K.; Siegel, J. S. *Angew. Chem. Int. Ed.* **2000**, *39*, 2323–2325.
- (66) Yu, G.; Gao, J.; Hummelen, J. C.; Wudl, F.; Heeger, A. J. *Science* **1995**, *270*, 1789–1791.
- (67) Li, G.; Zhu, R.; Yang, Y. *Nat. Photonics* **2012**, *6*, 153–161.
- (68) He, Z.; Zhong, C.; Su, S.; Xu, M.; Wu, H.; Cao, Y. *Nat. Photonics* **2012**, *6*, 591–595.
- (69) Zhou, J.; Wan, X.; Liu, Y.; Zuo, Y.; Li, Z.; He, G.; Long, G.; Ni, W.; Li, C.; Su, X.; Chen, Y. *J. Am. Chem. Soc.* **2012**, *134*, 16345–16351.
- (70) Kyaw, A. K. K.; Wang, D. H.; Wynands, D.; Zhang, J.; Nguyen, T.-Q.; Bazan, G. C.; Heeger, A. J. *Nano Lett.* **2013**, *13*, 3796–3801.
- (71) Lin, Y.; Zhan, X. *Mater. Horiz.* **2014**, *1*, 470.
- (72) Eftaiha, A. F.; Sun, J.-P.; Hill, I. G.; Welch, G. C. *J. Mater. Chem. A* **2014**, *2*, 1201.
- (73) Lloyd, M. T.; Anthony, J. E.; Malliaras, G. G. *Mater. Today* **2007**, *10*, 34–41.
- (74) Roncali, J.; Leriche, P.; Blanchard, P. *Adv. Mater.* **2014**, *26*, 3821–3838.
- (75) Beaujuge, P. M.; Fréchet, J. M. J. *J. Am. Chem. Soc.* **2011**, *133*, 20009–20029.
- (76) Verreet, B.; Rand, B. P.; Cheyns, D.; Hadipour, A.; Aernouts, T.; Heremans, P.; Medina, A.; Claessens, C. G.; Torres, T. *Adv. Energy Mater.* **2011**, *1*, 565–568.
- (77) Chen, G.; Sasabe, H.; Wang, Z.; Wang, X.-F.; Hong, Z.; Yang, Y.; Kido, J. *Adv. Mater.* **2012**, *24*, 2768–2773.
- (78) Chen, J. J.-A.; Chen, T. L.; Kim, B.; Poulsen, D. A.; Mynar, J. L.; Fréchet, J. M. J.; Ma, B. *ACS Appl. Mater. Interfaces* **2010**, *2*, 2679–2686.
- (79) Sonar, P.; Lim, J. P. F.; Chan, K. L. *Energy Environ. Sci.* **2011**, *4*, 1558–1574.
- (80) Bloking, J. T.; Han, X.; Higgs, A. T.; Kastrop, J. P.; Pandey, L.; Norton, J. E.; Risko, C.; Chen, C. E.; Brédas, J.-L.; McGehee, M. D.; Sellinger, A. *Chem. Mater.* **2011**, *23*, 5484–5490.
- (81) Pho, T. V.; Toma, F. M.; Chabiny, M. L.; Wudl, F. *Angew. Chem. Int. Ed.* **2013**, *52*, 1446–1451.
- (82) Zhang, X.; Lu, Z.; Ye, L.; Zhan, C.; Hou, J.; Zhang, S.; Jiang, B.; Zhao, Y.; Huang, J.; Zhang, S.; Liu, Y.; Shi, Q.; Liu, Y.; Yao, J. *Adv. Mater.* **2013**, *25*, 5791–5797.

- (83) Earmme, T.; Hwang, Y.-J.; Murari, N. M.; Subramaniyan, S.; Jenekhe, S. A. *J. Am. Chem. Soc.* **2013**, *135*, 14960–14963.
- (84) Sharenko, A.; Proctor, C. M.; van der Poll, T. S.; Henson, Z. B.; Nguyen, T.-Q.; Bazan, G. C. *Adv. Mater.* **2013**, *25*, 4403–4406.
- (85) Douglas, J. D.; Chen, M. S.; Niskala, J. R.; Lee, O. P.; Yiu, A. T.; Young, E. P.; Fréchet, J. M. J. *Adv. Mater.* **2014**, *26*, 4313–4319.
- (86) Shaw, P. E.; Wolfer, P.; Langley, B.; Burn, P. L.; Meredith, P. *J. Phys. Chem. C* **2014**, *118*, 13460–13466.
- (87) Anthony, J. E. *Chem. Mater.* **2010**, 101201082159004.
- (88) Brady, M. A.; Su, G. M.; Chabinye, M. L. *Soft Matter* **2011**, *7*, 11065–11077.
- (89) Ferguson, A. J.; Blackburn, J. L.; Kopidakis, N. *Mater. Lett.* **2013**, *90*, 115–125.
- (90) Lim, Y.-F.; Shu, Y.; Parkin, S. R.; Anthony, J. E.; Malliaras, G. G. *J. Mater. Chem.* **2009**, *19*, 3049.
- (91) Desiraju, G. R.; Gavezzotti, A. *Acta Crystallogr. B* **1989**, *45*, 473–482.
- (92) Purushothaman, B.; Bruzek, M.; Parkin, S. R.; Miller, A.-F.; Anthony, J. E. *Angew. Chem. Int. Ed.* **2011**, *50*, 6932–6932.
- (93) Kim, C.; Liu, J.; Lin, J.; Tamayo, A. B.; Walker, B.; Wu, G.; Nguyen, T.-Q. *Chem. Mater.* **2012**, *24*, 1699–1709.
- (94) Walker, B.; Liu, J.; Kim, C.; Welch, G. C.; Park, J. K.; Lin, J.; Zalar, P.; Proctor, C. M.; Seo, J. H.; Bazan, G. C.; Nguyen, T.-Q. *Energy Environ. Sci.* **2013**, *6*, 952.
- (95) Yook, K. S.; Chin, B. D.; Lee, J. Y.; Lassiter, B. E.; Forrest, S. R. *Appl. Phys. Lett.* **2011**, *99*, 043308.
- (96) Zhang, J.; Geng, H.; Virk, T. S.; Zhao, Y.; Tan, J.; Di, C.; Xu, W.; Singh, K.; Hu, W.; Shuai, Z.; Liu, Y.; Zhu, D. *Adv. Mater.* **2012**, *24*, 2603–2607.
- (97) Vasseur, K.; Rand, B. P.; Cheyins, D.; Temst, K.; Froyen, L.; Heremans, P. *J. Phys. Chem. Lett.* **2012**, *3*, 2395–2400.
- (98) Viterisi, A.; Montcada, N. F.; Kumar, C. V.; Gispert-Guirado, F.; Martin, E.; Escudero, E.; Palomares, E. *J. Mater. Chem. A* **2014**, *2*, 3536.
- (99) Swartz, C. R.; Parkin, S. R.; Bullock, J. E.; Anthony, J. E.; Mayer, A. C.; Malliaras, G. G. *Org. Lett.* **2005**, *7*, 3163–3166.
- (100) Anthony, J. E.; Brooks, J. S.; Eaton, D. L.; Parkin, S. R. *J. Am. Chem. Soc.* **2001**, *123*, 9482–9483.
- (101) Shu, Y.; Lim, Y.-F.; Li, Z.; Purushothaman, B.; Hallani, R.; Kim, J. E.; Parkin, S. R.; Malliaras, G. G.; Anthony, J. E. *Chem. Sci.* **2011**, *2*, 363.
- (102) Tantiwiwat, M.; University of California, S. B.; Physics. *Structure-function-property relationships in solution-processed Diketopyrrolopyrrole-based materials*; University of California, Santa Barbara: [Santa Barbara, Calif.], 2011.
- (103) Lin, J. D. A.; Liu, J.; Kim, C.; Tamayo, A. B.; Proctor, C. M.; Nguyen, T.-Q. *RSC Adv.* **2014**, *4*, 14101.
- (104) Platt, A. D.; Day, J.; Subramanian, S.; Anthony, J. E.; Ostroverkhova, O. *J. Phys. Chem. C* **2009**, *113*, 14006–14014.
- (105) Rivnay, J.; Noriega, R.; Northrup, J. E.; Kline, R. J.; Toney, M. F.; Salleo, A. *Phys. Rev. B* **2011**, *83*, 121306.
- (106) Mikhnenko, O. V.; Lin, J.; Shu, Y.; Anthony, J. E.; Blom, P. W. M.; Nguyen, T.-Q.; Loi, M. A. *Phys. Chem. Chem. Phys.* **2012**, *14*, 14196.
- (107) Ramanan, C.; Smeigh, A. L.; Anthony, J. E.; Marks, T. J.; Wasielewski, M. R. *J. Am. Chem. Soc.* **2012**, *134*, 386–397.

- (108) DeLongchamp, D. M.; Kline, R. J.; Fischer, D. A.; Richter, L. J.; Toney, M. F. *Adv. Mater.* **2011**, *23*, 319–337.
- (109) Chen, W.; Nikiforov, M. P.; Darling, S. B. *Energy Environ. Sci.* **2012**, *5*, 8045.
- (110) Foster, R. *J. Phys. Chem.* **1980**, *84*, 2135–2141.
- (111) Mulliken, R. S. *J. Am. Chem. Soc.* **1952**, *74*, 811–824.
- (112) Mulliken, R. S. *J. Am. Chem. Soc.* **1950**, *72*, 600–608.
- (113) Kitaigorodsky, A. I. *Mixed Crystals*; Softcover reprint of the original 1st ed. 1984.; Springer, 2012.
- (114) Shtukenberg, A. G.; Lee, S. S.; Kahr, B.; Ward, M. D. *Annu. Rev. Chem. Biomol. Eng.* **2014**, *5*, 77–96.
- (115) Rosenstock, H. B. *Phys. Rev.* **1969**, *187*, 1166–1168.
- (116) Giri, G.; Verploegen, E.; Mannsfeld, S. C. B.; Atahan-Evrenk, S.; Kim, D. H.; Lee, S. Y.; Becerril, H. A.; Aspuru-Guzik, A.; Toney, M. F.; Bao, Z. *Nature* **2011**, *480*, 504–508.
- (117) Noriega, R.; Rivnay, J.; Vandewal, K.; Koch, F. P. V.; Stingelin, N.; Smith, P.; Toney, M. F.; Salleo, A. *Nat. Mater.* **2013**, *12*, 1038–1044.
- (118) Anthony, J. E.; Vogel, D. E.; Schnobrich, S. M.; Clough, R. S.; Novack, J. C.; Redinger, D. *Mater. Matters* **2009**, *4*, 58.
- (119) Patrick, C. R.; Prosser, G. S. *Nature* **1960**, *187*, 1021–1021.
- (120) Williams, J. H.; Cockcroft, J. K.; Fitch, A. N. *Angew. Chem. Int. Ed. Engl.* **1992**, *31*, 1655–1657.
- (121) Cozzi, F.; Ponzini, F.; Annunziata, R.; Cinquini, M.; Siegel, J. S. *Angew. Chem. Int. Ed. Engl.* **1995**, *34*, 1019–1020.
- (122) Wheeler, S. E.; Houk, K. N. *J. Chem. Theory Comput.* **2009**, *5*, 2301–2312.
- (123) Coates, G. W.; Dunn, A. R.; Henling, L. M.; Dougherty, D. A.; Grubbs, R. H. *Angew. Chem. Int. Ed. Engl.* **1997**, *36*, 248–251.
- (124) Sakamoto, Y.; Suzuki, T.; Kobayashi, M.; Gao, Y.; Fukai, Y.; Inoue, Y.; Sato, F.; Tokito, S. *J. Am. Chem. Soc.* **2004**, *126*, 8138–8140.
- (125) Bondi, A. *J. Phys. Chem.* **1964**, *68*, 441–451.
- (126) Haas, S.; Batlogg, B.; Besnard, C.; Schiltz, M.; Kloc, C.; Siegrist, T. *Phys. Rev. B* **2007**, *76*, 205203.
- (127) Chen, J.; Martin, D. C.; Anthony, J. E. *J. Mater. Res.* **2007**, *22*, 1701–1709.
- (128) Hinderhofer, A.; Frank, C.; Hosokai, T.; Resta, A.; Gerlach, A.; Schreiber, F. *J. Chem. Phys.* **2011**, *134*, 104702.
- (129) Mayer, A. C.; Kazimirov, A.; Malliaras, G. G. *Phys. Rev. Lett.* **2006**, *97*, 105503.
- (130) Haas, B.; Gries, K. I.; Breuer, T.; Häusler, I.; Witte, G.; Volz, K. *Cryst. Growth Des.* **2014**, *14*, 3010–3014.
- (131) Gelbrich, T.; Threlfall, T. L.; Hursthouse, M. B. *CrystEngComm* **2012**, *14*, 5454.
- (132) Fabbiani, F. P. A.; Dittrich, B.; Florence, A. J.; Gelbrich, T.; Hursthouse, M. B.; Kuhs, W. F.; Shankland, N.; Sowa, H. *CrystEngComm* **2009**, *11*, 1396–1406.
- (133) Anger, F.; Ossó, J. O.; Heinemeyer, U.; Broch, K.; Scholz, R.; Gerlach, A.; Schreiber, F. *J. Chem. Phys.* **2012**, *136*, 054701.
- (134) Trasi, N. S.; Taylor, L. S. *CrystEngComm* **2012**.
- (135) Aziz, H.; Popovic, Z.; Xie, S.; Hor, A.-M.; Hu, N.-X.; Tripp, C.; Xu, G. *Appl. Phys. Lett.* **1998**, *72*, 756–758.
- (136) Krebs, F. C. *Stability and Degradation of Organic and Polymer Solar Cells*; John Wiley & Sons, 2012.
- (137) Shirota, Y. *J. Mater. Chem.* **2005**, *15*, 75–93.

- (138) Naito, K.; Miura, A. *J. Phys. Chem.* **1993**, *97*, 6240–6248.
- (139) Fabregat-Santiago, F.; Bisquert, J.; Cevey, L.; Chen, P.; Wang, M.; Zakeeruddin, S. M.; Grätzel, M. *J. Am. Chem. Soc.* **2009**, *131*, 558–562.
- (140) Leijtens, T.; Ding, I.-K.; Giovenzana, T.; Bloking, J. T.; McGehee, M. D.; Sellinger, A. *ACS Nano* **2012**, *6*, 1455–1462.
- (141) Redinger, D.; Clough, R. S.; Novack, J. C.; Caldwell, G.; Payne, M. M.; Anthony, J. E. *MRS Online Proc. Libr.* **2010**, *1270*, null – null.
- (142) Swallen, S. F.; Kearns, K. L.; Mapes, M. K.; Kim, Y. S.; McMahon, R. J.; Ediger, M. D.; Wu, T.; Yu, L.; Satija, S. *Science* **2007**, *315*, 353–356.
- (143) Rimer, J. D.; An, Z.; Zhu, Z.; Lee, M. H.; Goldfarb, D. S.; Wesson, J. A.; Ward, M. D. *Science* **2010**, *330*, 337–341.
- (144) Sizemore, J. P.; Doherty, M. F. *Cryst. Growth Des.* **2009**, *9*, 2637–2645.
- (145) Brunetti, F. G.; Gong, X.; Tong, M.; Heeger, A. J.; Wudl, F. *Angew. Chem. Int. Ed.* **2010**, *49*, 532–536.
- (146) Gong, X.; Tong, M.; Brunetti, F. G.; Seo, J.; Sun, Y.; Moses, D.; Wudl, F.; Heeger, A. J. *Adv. Mater.* **2011**, *23*, 2272–2277.
- (147) Baird, J. A.; Van Eerdenbrugh, B.; Taylor, L. S. *J. Pharm. Sci.* **2010**, *99*, 3787–3806.
- (148) Ping, W.; Paraska, D.; Baker, R.; Harrowell, P.; Angell, C. A. *J. Phys. Chem. B* **2011**, *115*, 4696–4702.
- (149) Sun, Y.; Xi, H.; Ediger, M. D.; Richert, R.; Yu, L. *J. Chem. Phys.* **2009**, *131*, 074506.
- (150) Sun, Y.; Xi, H.; Chen, S.; Ediger, M. D.; Yu, L. *J. Phys. Chem. B* **2008**, *112*, 5594–5601.
- (151) Sun, Y.; Zhu, L.; Kearns, K. L.; Ediger, M. D.; Yu, L. *Proc. Natl. Acad. Sci.* **2011**, *108*, 5990–5995.
- (152) Michaels, A. S.; Tausch, F. W. *J. Phys. Chem.* **1961**, *65*, 1730–1737.
- (153) Davey, R. J.; Black, S. N.; Logan, D.; Maginn, S. J.; Fairbrother, J. E.; Grant, D. J. W. *J. Chem. Soc. Faraday Trans.* **1992**, *88*, 3461–3466.
- (154) Solomonov, I.; Osipova, M.; Feldman, Y.; Baehtz, C.; Kjaer, K.; Robinson, I. K.; Webster, G. T.; McNaughton, D.; Wood, B. R.; Weissbuch, I.; Leiserowitz, L. *J. Am. Chem. Soc.* **2007**, *129*, 2615–2627.
- (155) Lai-Chang Zhang. *Crystallization Behavior and Control of Amorphous Alloys.*; INTECH Open Access Publisher, 2012.
- (156) Alves, H.; Molinari, A. S.; Xie, H.; Morpurgo, A. F. *Nat. Mater.* **2008**, *7*, 574–580.
- (157) Mathis, T.; Mattenberger, K.; Moll, P.; Batlogg, B. *Appl. Phys. Lett.* **2012**, *101*, 023302.
- (158) Subramanian, S.; Park, S. K.; Parkin, S. R.; Podzorov, V.; Jackson, T. N.; Anthony, J. E. *J. Am. Chem. Soc.* **2008**, *130*, 2706–2707.
- (159) Gundlach, D. J.; Royer, J. E.; Park, S. K.; Subramanian, S.; Jurchescu, O. D.; Hamadani, B. H.; Moad, A. J.; Kline, R. J.; Teague, L. C.; Kirillov, O.; Richter, C. A.; Kushmerick, J. G.; Richter, L. J.; Parkin, S. R.; Jackson, T. N.; Anthony, J. E. *Nat Mater* **2008**, *7*, 216–221.
- (160) Brütting, W.; Adachi, C. *Physics of Organic Semiconductors*; John Wiley & Sons, 2012.
- (161) Jurchescu, O.; Mourey, D.; Subramanian, S.; Parkin, S.; Vogel, B.; Anthony, J.; Jackson, T.; Gundlach, D. *Phys. Rev. B* **2009**, *80*.
- (162) Shahid, M.; McCarthy-Ward, T.; Labram, J.; Rossbauer, S.; Domingo, E. B.; Watkins, S. E.; Stingelin, N.; Anthopoulos, T. D.; Heeney, M. *Chem. Sci.* **2011**, *3*, 181–185.